INVESTIGATION OF FOCAL EPILEPSY USING GRAPH SIGNAL PROCESSING

INVESTIGATION OF FOCAL EPILEPSY USING GRAPH SIGNAL PROCESSING

Master Thesis

To obtain the degree of Master in Electrical Engineering with specialization in Signals and System, from Delft University of Technology, to be defended in public on

by

Gaia ZIN

born in Camposampiero, Italy

Student number
Project duration

Thesis Committee:
Prof. dr. A. Jansen Technische Universiteit Delft

Prof. dr. ir. J. de Wit heeft in belangrijke mate aan de totstandkoming van het proefschrift bijgedragen.

Keywords: ...

SUMMARY

Epilepsy is one of the most common neurological disorders worldwide. Its manifestations, the seizures, are due to a group of neurons' abnormal and synchronous activity. The unpredictable nature of these events hinders the quality of life of those affected. In particular, focal seizures show a localized onset of the abnormal activity and are the most common ones. Correct detection of the episodes can help clinicians to give the best medical treatments. This research project arises from the need to have automatic algorithms for seizure detection with a high number of correctly detected seizures for low false alarm rates. Recent studies have shown disorganization in how brain areas interact with each other before and during a seizure. We decided to model this change in connectivity patterns by inferring graphs from EEG recordings of epileptic patients. We work with seventeen subjects suffering from focal epilepsy, and we build, for each of them, a graph of the activity preceding (preictal) and during (ictal) a seizure. After that, we exploit techniques from graph signal processing to build a detector for seizures. Last, we analyze the density of connections of the inferred graphs to indicate the seizure onsets. The obtained results are unsuitable for real-life applications, but they are a starting point for further research. Furthermore, we find that most the proposed ictal or preictal graphs show less connections in the nodes involved with the seizure onset.

ACKNOWLEDGEMENTS

This was a long and exciting journey (and adventure).It taught me a lot of lessons and made me grow both academically and personally. I want to thank all the people who were there with me during these past months.

First, I would like to thank my supervisors Elvin and Bori. You both transmit a lot of passion for science and learning. You were a great source of inspiration. Elvin, I sincerely admire the way you work and teach. Thank you for your honesty, the discussions, last-minute meetings. In general, thank you for transmitting the desire always to do better. Bori, thank you for your patience, kindness, and feedback, which truly was a turning point for me.

Next, thank you to all my friends who were always there to support, encourage me, and make this time all the more enjoyable. I consider myself extremely lucky to have you all. In particular, thank you to Karen, Plad (also known as Alessandro), Marta, Giulia, Cassy, Gius, Ele, and Elena. Karen, you were fundamental in these years. Thank you for the silly walks, the study sessions, and thank you for supporting me even from afar on your crazy adventure. Thank you for being an example both academically and as a person in general. Plad, thank you for the laughs, your pep talks, your special honesty, and thank you for withstanding my hate-relationship with comas. Thank you in general for being a good friend. Marta, thank you for believing in me and reasoning with me when I needed it (with your unique grace). In general, thank you for truly being a mussel. Gius, you are one kind, special person I could always talk to, during the good and the bad. Elena, a very big and loud thank you to you too. Thanks for the scientific talks, deep discussions, and breaks. Giulia and Cassy, also known as my trusted neuroscientists, thank you both for your help, insights, and passion for what you study. In general, thank you to my "pepper"-friends expecially Mirkino, Albi, Luca and Elena. You all are essential part of my life and great teachers.

Thanks also to all the fantastic fellow students and friends of SS and, in particular, Mihir, Chris, Brenda, Felix, and Jory. Thank you for making the stress of the last period more bearable and for prompting me to chill when it was time. A special thanks also to Alberto. Thanks for your kindness, suggested papers, and thank you for the curiosity that you transmit.

Last but definitely not least, thank you to all my family. I would not be here both physically and mentally without you. In particular, thank you, dad, uncle Roberto and aunt Ella for your silent and loud support. Mum, thank you for your love and phone calls. Giuly, thank you for being the "loving" little sister you are, for the many online study sessions (where I could only look at your forehead), and thank you for being an example for me.

Contents

1

INTRODUCTION

Epilepsy is a disease of the brain affecting 50 million people worldwide [1]. Concisely, an epileptic seizure occurs when a group of neurons, also called an assembly, begins to fire with an abnormal frequency. The unpredictable nature of seizures causes social and psychological effects and may lead to early death [2]. Seizure-under reporting is an issue in this regard [3, 4]: on average epileptic patients and caregivers do not recognize 50% of the occurred seizures, mainly when episodes comprise loss of consciousness or if they happen during the night [5]. It follows problems concerning medical treatment. Hence the need for an automated seizure-detection algorithm. Most of the current algorithms available cannot be implemented in a real-life scenario due to their low level of false alarm, given a high value of correctly detected seizures. Concretely, we desire an average of $10^{-}3$ false alarms in an hour. A better understanding of the disease could aid the way we detect the episodes and treat epileptic patients, hence this research. This project focuses on focal epilepsy, where the onset of the abnormal activity is initially localized.
More scientists have started paying more attention to how brain areas communicate before and during a seizure in recent years. In particular, they found a disruption in the normal connectivity patterns during a seizure [6]. In particular, they found a disruption in the normal connectivity patterns during a seizure [6]. The main research question of this project is:

RQ1. Can these alterations in brain connectivity patterns be modeled and then used to detect an incoming seizure?

To address this question, we propose a new framework for focal epilepsy detection, which exploits techniques from graph signal processing. The proposed algorithm is trained and tested on data from a specific patient (patient-dependent algorithm). We cast the problem as a classification between the seizure (ictal) and non-seizure (later called background) class. The two most important phases of this research are the extraction and modeling of the graph and the development of the detector. First, we use the method proposed in [7] to construct a graph of each patient's brain activity before (preictal) and during a seizure. Then, we investigate the distribution of the two classes over the preictal

graph and exploit the difference in the so-called signal bandwidth to build a detector. After that, we repeat this last step using the ictal graph. In this way, we design and propose two different detectors. We compare the performance of these detectors with:

1. a detector that exploits the inferred graphs but disregards the bandwidth information,
2. a simple energy detector that does not exploit any network information (single electrode analysis), and
3. a detector working on a graph decided a priori and modeling a brain state where every brain area is in communication with all the others (fully connected network).

We evaluate the proposed framework by studying the Receiver operating characteristic (ROC) curves which describe the True Positive Rate (TPR) of the detector as a function of the False Positive Rate (FPR). In particular, we exploit the Area Under the Curve (AUC), which is the integral of the ROC curve, to compare performances. We obtained satisfying results (AUC > 0.8) for seven out of the seventeen studied patients. However, the derived TPRs are still too low. In the studied database, the only patient with slightly more than one hour of testing data reported TPR=0.02 for a false alarm rate of 0.5. Furthermore, the proposed algorithm does not outperform the single electrode detector.
However, we further analyze the inferred graphs and pose the following and last question:

RQ2. Can we gain more insights regarding the localization of the seizure onset by the inferred model?

The motivation behind this question follows. More than 30% of epileptic patients do not respond favorably to treatments [8]. When these subjects suffer from focal epilepsy, in the worst-case scenario, surgery can be used to remove clinically the onset area, also called *epileptogenic zone*. It is of the utmost importance to precisely localize this area. Consequently, we want to verify whether the model for the graph we have used in this research can aid the current methodology for seizure onset identification. We find that, for some patients, the preictal graph shows fewer connections in the area associated with the onset.

Chapter 2 provides a basic introduction to epilepsy and the tools from graph signal processing that we leverage in this research. Then, in Chapter 3, we outline the detection algorithm proposed in the literature for Epilepsy detection to delineate our proposed method in Chapter 4. Chapter 5 provides the numerical results and their possible interpretation. Finally, we summarize the work done and propose future works in Chapter 6.

NOTATION

In this work, we denote scalars with plain letters (i.e., x or X), and vectors and matrices with bold lowercase (i.e., $\boldsymbol{x}$), and uppercase letters (i.e., $\boldsymbol{X}$) respectively. We reserve calligraphic notations to more complex structures like graphs or lists of matrices (i.e., $\mathcal{G}$ and $\mathcal{X}$). The vertical bars |...| denote the cardinality of the set between them (i.e., $|\mathcal{V}|$).

2

BACKGROUND

This chapter provides the background knowledge founding this research.
We start in Section 2.1 with basic concepts regarding epilepsy and, in particular, focal epilepsy. The section states: what epilepsy is, how to diagnose it, which are the brain states that we leverage in this project, how and why we regard the disease as a disorder of brain network organization. Then, Section 2.2 focuses on the tool used to approach the problem: graph signal processing techniques. The concepts to retain from the section are the meaning of graph and graph signal, frequency analysis of a graph signal, and the bandwidth of a graph signal. Last, Section 2.3 summarizes the main concepts of the chapter.

2.1. EPILEPSY

Epilepsy is a neurological disease affecting 50 million people worldwide and causing the death of 125.000 of them per year [9]. It manifests in the form of *seizures* [10] that are moments of excessive and abnormal neural activity. In an epileptic brain under seizure, the level of excitability of a pool of neurons is altered, thus resulting in the production of long sequences of action potentials. These neurons fire synchronously and at an excessive rhythm [11]. Nevertheless, there is no direct relation between seizures and epilepsy: a subject manifesting a seizure does not always suffer from the disorder [12]. In fact, seizures can also be caused by psychological or exogenous factors (*provoked seizures*) without there being a chronic state [13, 14]. Examples of exogenous factors are alcohol abuse, alcohol or drug withdrawal, sleep deprivation, and intermittent lights exposure. Conversely, unprovoked seizures, also called reflex seizures, are not induced by external stimulations. The International League against Epilepsy (ILAE) defines the disorder when at least one of the following conditions occur [15]:

1. Appearance of at least two unprovoked seizures with a minimum time gap of 24 hours.

2. Appearance of an unprovoked seizure and 60% probability of another one occurring within ten years.

3. Diagnosis of a so-called epilepsy syndrome [16].

Scalp Electroencephalography (EEG), which we call simply EEG in this work, is a monitoring tool for neural activity. It has been leveraged for epilepsy prediction and detection due to its non-invasiveness, high temporal resolution, and relatively low cost [17] [18]. It adopts multiple electrodes placed on the scalp of the patient under test, as illustrated in Figure 2.1.

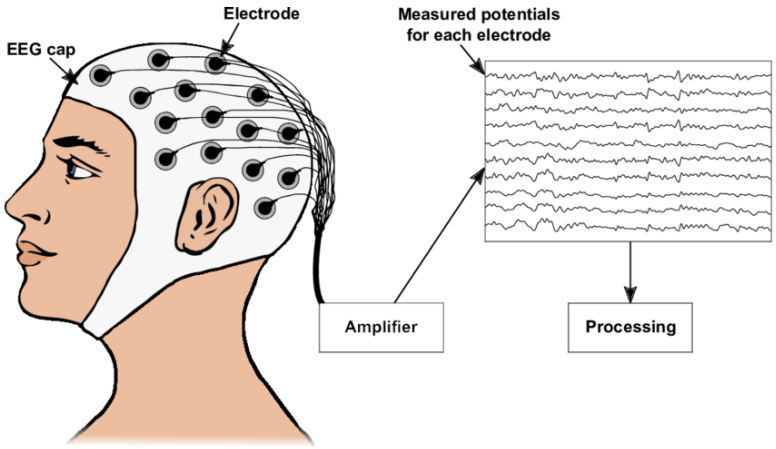

Figure 2.1: Depiction of an Electroencephalography system. Electrodes are placed on the scalp of the tested patient, sometimes using a cap, as in the depicted case, in order to monitor the brain electrical activity expressed as measured potential per sensor [19].

The EEG of patients undergoing seizure depicts a disordered rhythm of brain potentials. For this reason, the disease is now recognized as a paroxysmal cerebral dysrhythmia [20]. Figure 2.2 illustrates this concept: during a seizure, the electrical brain potentials exhibit evolving sharp waves [21]. In particular, this dysrhythmia is characterized by: i) alteration in the signal's amplitude, ii) change in frequency components, and iii) the spread of the abnormal pattern to different brain areas. As a consequence, this evolution is observed both in time, frequency and space domain. Physicians recognize four phases in the brain patterns of an epileptic patient. These are: i) *interictal* that is the state of normal activity happening far away in time to the seizure; ii) *preictal* which happens right before a seizure; iii) *ictal* state during which a seizure occurs; iv) *postictal* that is the state taking place right after a seizure. This is depicted in Figure 2.2. Preictal periods are a valuable source of information. They are leveraged and studied mainly in algorithms for seizure prediction [23, 24]. They also underpin mechanisms behind seizure such as whether the ictal event involves all brain hemispheres or not [25]. Instead, ictal patterns are multiple and are strongly dependent on the area of the brain involved in the abnormal activation [26] which also influences the related symptomatology and EEG pattern [27]. In 2017 ILAE sought for a unique classification of the epileptic disease that, as depicted in Figure 2.3, is based on more levels [28]. We distinguish: *Focal Seizure* (previously termed *Partial Seizure*) where the start of the seizure is localized around a restricted area of the brain; *Generalized Seizure* where the epileptic

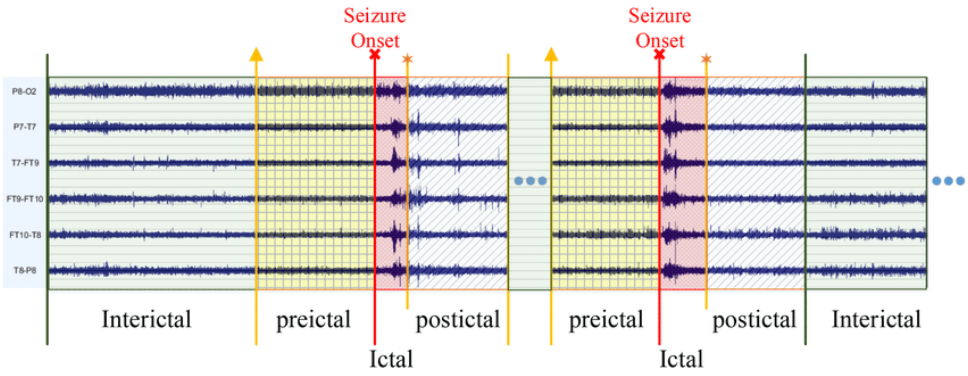

Figure 2.2: EEG tracing of epileptic subject [22]. Six electrodes, on the y-axis of the figure, are depicted. The image is annotated with the four phases of the seizure event: ictal that is during seizure; preictal and postictal that are before and after the event respectively; interictal that is between ictal events and that denotes normal activity.

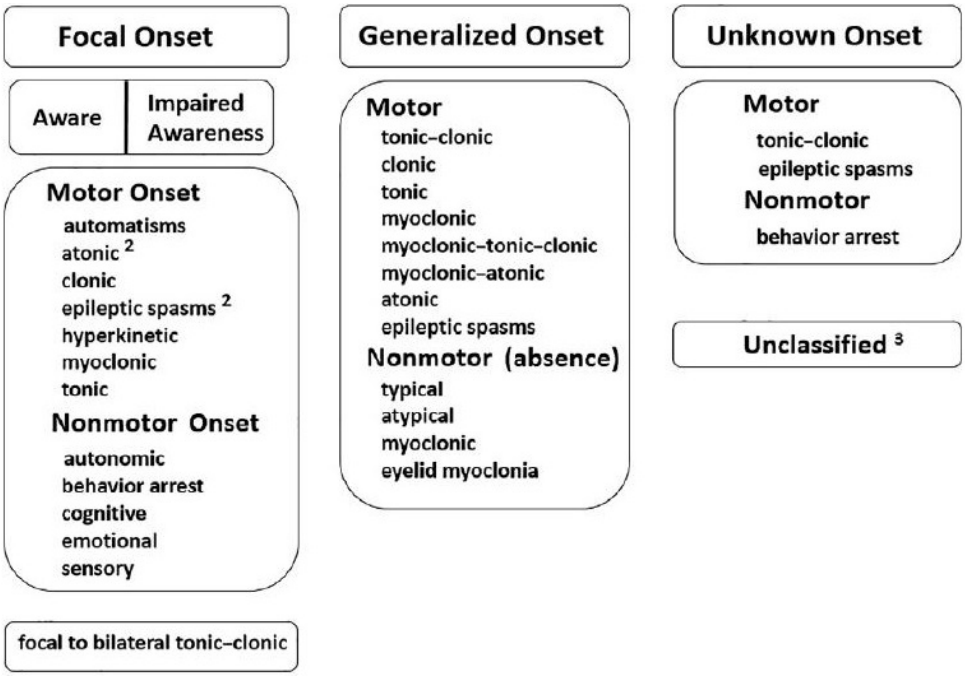

Figure 2.3: Current seizure classification according to ILAE [28]. First, they classify the event in terms of the localization of the ictal activity at seizure onset. Therefore *Focal* denotes seizures starting from a local and restricted area of the brain; *Generalized* refers to seizures immediately involving both cerebral hemispheres while *unknown* marks ictal events for which the initial extent is unknown. Further characteristics can be identified. For example a focal seizure can become *Aware*, also known as *Simple Seizure* if consciousness is retained; with *Impaired Awareness*, also known as *Complex Seizure*, in the opposite case. In other cases, it can also be identified whether also motor functions are involved or not.

behavior affects immediately both hemispheres of the brain; and unknown origin. The associated symptoms depend on the cerebral lobe involved in the ictal process and its associated functions (Fgure 2.4). For example, Temporal Lobe Epilepsy (TLE) manifests in the form of focal seizures starting from the temporal lobe and causes patients to experience problems with speech recognition tasks [29]. Conversely, occipital Lobe Epilepsy patients could have visual hallucinations during the ictal events [30]. In this work, we

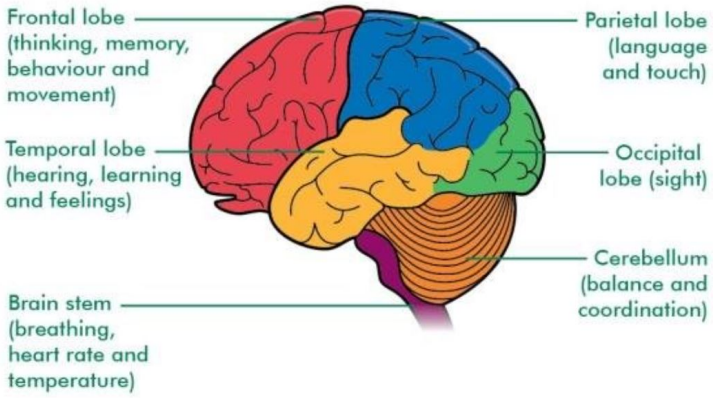

Figure 2.4: Four brain lobes, with associated functions and two other components of the nervous system with corresponding functions [31].

decided to focus on the detection of focal epilepsy for two main reasons. First, it affects a higher percentage of the population compared with generalized epilepsy [32]. Second, it is more difficult to treat, and there is sometimes the need to identify the seizure onset zone (epileptogenic zone) in order to remove it with surgery [33]. The localization of the epileptogenic zone is mostly done by placing multiple in-depth electrodes on the surface of the presumed epileptic area after a surgical incision in the skull. This technology, called Electrocorticography (ECoG), is invasive [34] but allows for cleaner signals in terms of noise and artifacts when compared with EEG data [35]. We seek a method that also gains insight into the localization of the seizure onset zone from EEG recordings to support the other diagnostic methodologies.

For this purpose, we aim at exploiting the spatial information most optimally. Friston et al. define functional connectivity as the "*correlation between spatially remote neurophysiological events*" [36]. This means that two brain areas are functionally connected when the activity recorded at these locations shows statistical dependence. In these terms, a functional brain network refers to a map of functional connectivity between the different brain areas. It has been demonstrated that different neural activity (be it sleep, resting, or other states) corresponds to specific functional networks. When a seizure occurs, there is a change in network functional connection meant as in change in the way the areas of the brain communicate and influence each other. Epilepsy is now considered a disorder of brain network reorganization [37]. The core idea of our proposed algorithm is to build a model of the functional connections existing between the various areas underlying the electrodes before and during a seizure. In this way, we de-

tect seizures when the normal functional network are disrupted. We exploit graph signal processing techniques for this purpose.

2.2. GRAPH SIGNAL PROCESSING

Graph signal processing (GSP) is a discipline that develops methods for signals living in irregular (or non-Euclidean) domains. Examples are brain signals [38], recommendation systems [39], and power grids [40] [41]. In these cases, signals are not represented in regular domains such as those of a time series or of an image. Instead, the domain that best suits them is the one of graphs.
Here, Subsection 2.2.1 introduces the notions of graph and graph signal while Subsection 2.2.2 deals with the basics of spectral analysis on a graph as well as the concept of bandwidth. Last, Subsection 2.2.3 applies the concepts of GSP to neural signals.

2.2.1. GRAPH AND GRAPH SIGNALS

A graph $\mathcal{G}(\mathcal{V},\mathcal{E})$ is a mathematical structure which is uniquely represented by a set of N nodes, also called vertices, $\mathcal{V} = (v_1,...,v_N)$ connected by a a set of M edges $\mathcal{E} = (e_1,...,e_M)$, Figure 2.5. Edges can have a specific direction (directed graph, Figure 2.6) or can have a

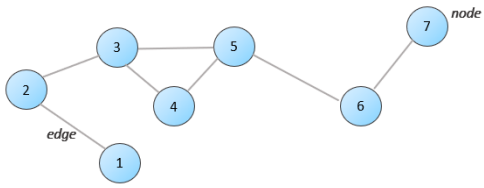

Figure 2.5: Undirected graph with seven nodes (N = 7) and seven edges (M = 7). The nodes have been enumerated for visualisation purposes.

weight associated with them (weighted graph, Figure 2.7).
In this study we deal with undirected weighted graphs and, we use the so called Lapla-

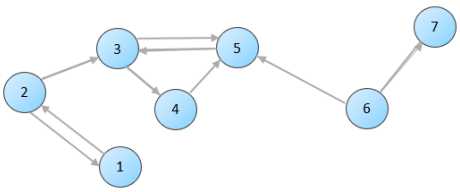

Figure 2.6: Directed graph with seven nodes and nine edges. Arrows specify the direction.

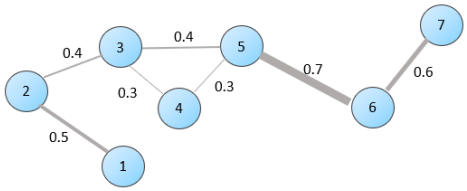

Figure 2.7: Undirected, weighted graph with seven nodes and edges. The thickness of the edges is made proportional to the weight.

cian matrix **L** in order to represent the topological structure of the graph. The Laplacian matrix is defined as:

$$\mathbf{L} = \mathbf{D} - \mathbf{A} \tag{2.1}$$

Here **A** is the so called adjacency matrix, a $|\mathcal{V}| \times |\mathcal{V}|$ structure whose entry $a_{i,j}$ in row i and column j contains the weight of the edge connecting node i and j; **D** is the diagonal degree matrix whose diagonal entry $d_{i,i}$ contains the sum of the weights connected to node i: $d_{i,i} = \sum_{j \in \mathcal{N}_i} a_{i,j}$ with $\mathcal{N}_i$ the set of nodes neighbouring i.
The Laplacian matrix is symmetric and satisfies the following eigendecomposition:

$$\mathbf{L} = \mathbf{U}\mathbf{\Lambda}\mathbf{U}^H \tag{2.2}$$

Here **U** is an orthogonal matrix of eigenvectors of **L** while $\mathbf{\Lambda}$ carries the eigenvalues of the Laplacian stored in increasing order ($\lambda_1 \leq \lambda_2 \leq ... \leq \lambda_N$). The eigenvalues of **L** are all positive (not strictly) with the smallest one $\lambda_1 = 0$.

A graph signal **x** is defined as a mapping from the vertex set to the set of real numbers $\mathbf{x} : \mathcal{V} \rightarrow \mathbb{R}$. This implies that to each node a number is associated, Figure 2.8. The graph signal is modeled as a vector **x** where the i^{th} entry x_i reports the quantity associated with the i^{th} node. In our work, we associate to every electrode a node. It follows that at time

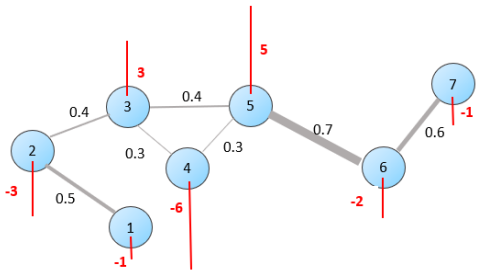

Figure 2.8: Representation of signal on a graph. The red vertical bar are proportional to the magnitude and sign of the quantity of the signal recorded at a given node, which are annotated in red.

instant t the graph signal $\mathbf{x}_t$ is given by the collection of potential values recorded at that instant of time by the EEG sensors.

2.2.2. SPECTRAL ANALYSIS ON THE GRAPH

It is possible to decompose **x** as a sum of fundamental signals with different degrees of variability on the graph. This is done by the Graph Fourier Transform (GFT) which behaves similarly to the Discrete Fourier Transform (DFT). The GFT uses as basis for the signal decomposition, the eigenvectors **U** of the Laplacian matrix.
The definition of GFT of **x** follows:

$$\hat{\boldsymbol{x}} = \boldsymbol{U}^H \boldsymbol{x} \tag{2.3}$$

We say that the GFT projects signal $\boldsymbol{x}$ on the space of eigenvectors of the Laplacian matrix. The inverse operator is called Inverse Graph Fourier Transform (IGFT) and it is defined as:

$$\mathbf{x} = \mathbf{U}\hat{\mathbf{x}} \tag{2.4}$$

Equation (2.4) means that $\mathbf{x}$ can be rewritten as:

$$\mathbf{x} = \mathbf{u}_0 \hat{x}_0 + \ ... \ + \mathbf{u}_N \hat{x}_N = \sum_{k=0}^{N} \mathbf{u}_k \hat{x}_k \tag{2.5}$$

Here $\mathbf{u}_k$ is the k^{th} column of $\mathbf{U}$ while $\hat{x}_k$ is the k^{th} scalar entry of $\hat{\mathbf{x}}$. The eigenvalues λ_k of $\mathbf{L}$ represents the concept of frequency: for lower eigenvalues, the corresponding fundamental eigenvector signal presents smaller variations in values from one node to the neighboring ones.

The bandwidth $\mathscr{F}$ of $\mathbf{x}$ is defined as the set of frequencies for which the graph Fourier components differ from zero. We write:

$$\mathscr{F} = \{\lambda_k \mid \hat{x}_k = \mathbf{u}_k^H \mathbf{x} \neq 0\} \tag{2.6}$$

Figure 2.9 depicts in a) and b) two band-limited signals, and it shows their spectrum in d) and e) respectively. For them, there exist a set of frequencies for which the associated Fourier graph component $\hat{x}_k$ is null. In particular, the first signal has low-frequency components, given that small eigenvalues comprise its bandwidth. The opposite is true for the second signal which has high-frequency components. Figure 2.9 c) shows a non band-limited signal: its spectrum in f) has no negligible Fourier components.

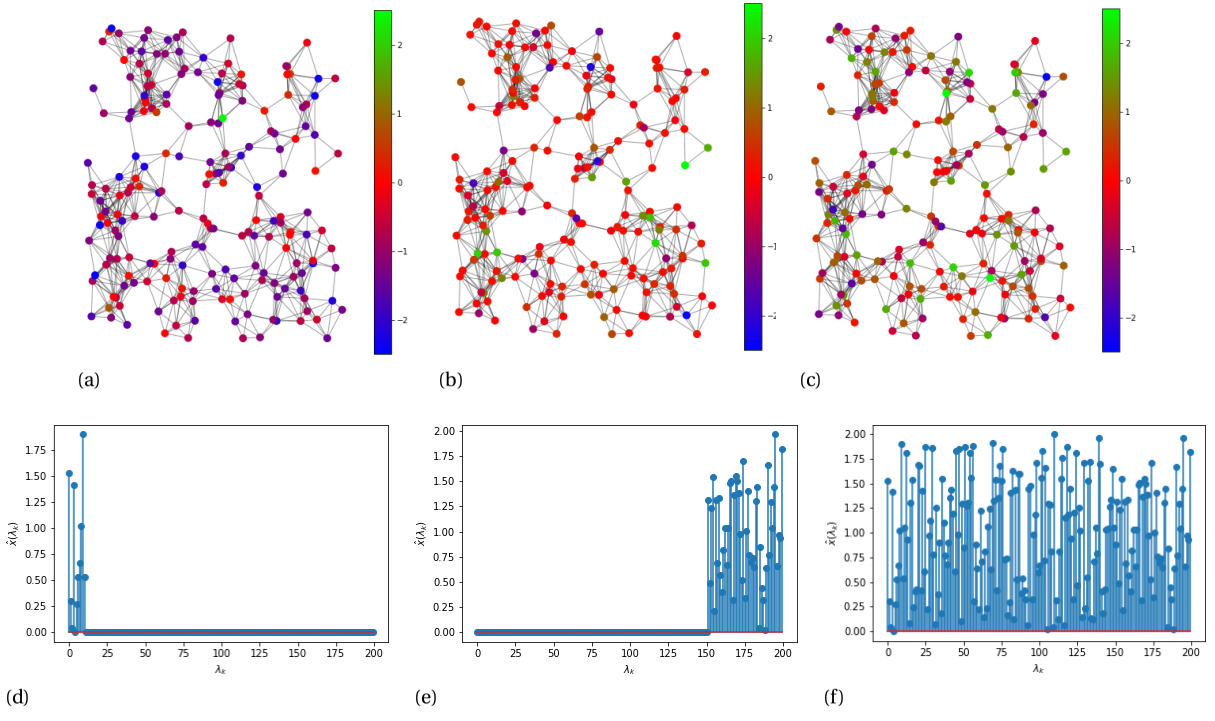

Figure 2.9: Signals with different bands on the same graph. The signal magnitude is color coded. In particular a) depicts a band-limited signal with low frequency components, its corresponding spectrum in d); in b) band-limited signal with high frequency components, its corresponding spectrum in e); in c) a non band-limited signal, its corresponding spectrum in e).

2.2.3. APPLICATION TO NEURAL SIGNALS

Graphs can be exploited to model how the different brain areas communicate with each other. In these terms, each node can represent a neural region while the edges encode functional or structural connections [42]. In recent years GSP techniques have been thoroughly applied to brain signals to study behavior [43, 44] and neurological disorders, i.e. epilepsy, autism and Alzheimer. [45] [46]. In particular, a graph spectral analysis allows to verify when and which brain regions act in unison. As a matter of fact, low graph frequencies are associated with areas with similar signals. This is interpreted as a collaboration between these brain areas. The opposite applies to high graph frequency components. For example, Huang at al. study the learning process with GSP techniques [47]. They claim that when a subject becomes accustomed to a new task, there is a high collaboration between brain areas, and hence the associated graph signal has low-frequency components. Conversely, while learning the task, the brain activity at different areas becomes different. Hence, high graph frequencies are associated with the learning process.

2.3. SUMMARY

In this chapter, we introduced the basic concepts of epilepsy and graph signal processing. Epilepsy is a neurological disorder manifesting itself in the form of seizures. During these events, a neuronal pool starts firing synchronously and at an abnormal rhythm. When this set of neurons is restricted to a small cerebral area, the type of epilepsy is focal. EEG is a diagnostic tool recording the electrical brain activity of a subject through multiple electrodes. In particular, ictal activity denotes the patterns of brain waves during a seizure, while preictal refers to the moments right before the start of a seizure. During the ictal event the normal connectivity between the cerebral areas is altered. As a consequence the disease is defined as a network organization disorder. In this study we aim at modeling this alteration of brain connectivity using graph signal processing tools. Graph signal processing studies signals lying on non-Euclidean domains modeled by a graph. These are used to model networks and are therefore suitable candidates for representing the cerebral dynamics that are altered during a seizure. In graph signal processing, spectral analysis can be performed thanks to the use of the graph Fourier transform operator. The frequencies are specific to the graph and are given by the eigenvalues of the so-called Laplacian matrix which encodes the topology of the graph itself. In these terms, the bandwidth of a graph signal is defined as the set of graph frequencies for which their corresponding component is different from zero.

3

LITERATURE REVIEW

This chapter provides an overview of the current methodologies for seizure detection from EEG data present in the literature. In particular, we focus on the ways to exploit spatial information. We start with algorithms working on recordings of just one EEG electrode in Section 3.1. Section 3.2 deals with techniques integrating information from multiple sensors recordings. Then, Section 3.3 details the main metrics used in the literature to evaluate algorithms for seizure detection. Finally, Section 3.4 summarizes the chapter.

3.1. UNIVARIATE ALGORITHMS

Univariate algorithms exploit only single electrode recordings. They are the simplest algorithms as they do not exploit the spatial information coming from the different EEG sensors. As a consequence, the evolution that they can capture comes either from the time or frequency domain. We differentiate them by the type of features extracted: i) time-based features; ii) frequency-based features; iii) time and frequency-based features.

In particular,Runarsson et al. developed a time-based detection algorithm for neonatal seizures [48]. The rationale behind their work is that during a seizure, there can be a strong spike pattern. Subsequently, the features extracted for classification regard the height and width of the spikes. Similarly, Tessy et al. base their algorithm on the increase in signal amplitude that is observed during the ictal condition [49]. They extract the vertical distance between consecutive samples, also called line length, and the energy E of the signals. They calculate this last quantity as:

$$E = \sum_{i=0}^{N-1} x_i^2 \tag{3.1}$$

Here N is the number of samples, and x_i is the i^{th} sample of the signal. This feature is quite easy to extract and will be used later in this project to evaluate the performance of our proposed algorithm.

A more innovative way to exploit time evolution comes from graph theory and, in particular, visibility graphs [50]. These structures map nodes to time samples and define edges as a function of the amplitude recorded at those instants as shown in Figure 3.1. There

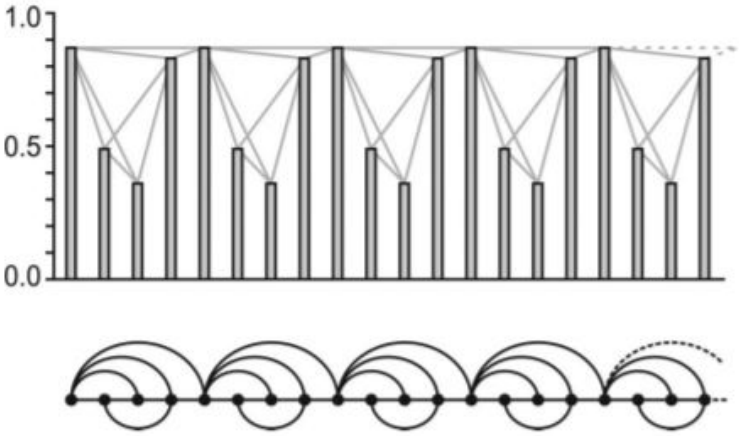

Figure 3.1: Construction of visibility graph[50]. The bar plot on top is a time series: the x-axis represents time while the height of the bar indicates the amplitude at a point in time. The visibility graph (bottom figure) is constructed by connecting points in time that are "visible" to each other.

are two main ways to exploit graphs. The first one is to extract a characteristic of the graph itself and use it as a feature. For example, Zeynab et al. [51] develop a multi-class (ictal, interictal, and healthy) algorithm using the weighted visibility graph (WVG) first proposed in [52]. They assign a weight to the edge between nodes i and j based on the angle formed by two corresponding time instants. After that, they extract a function of the graph's edges and use it as input to different machine learning classifiers. The second way to use a graph is to use the GFT operator and extract features from the obtained projections. In [53] Priyanka et al. first divide the signals into segments and then construct a WVG per segment. They construct an edge using a so-called Gaussian kernel function on the distance between points of the signal. Subsequently, the segments are projected on the eigenvectors of the Laplacian of the graph. Then the power spectral density of the evaluated GFT coefficients is used as a discriminating feature.
Deep learning-based methodologies have been more and more applied in the field of Epilepsy detection and prediction with promising results, due to the large databases that have been recently made publicly available [54]. Other popular techniques exploit transform using both time and frequency information. This is the case of wavelet decomposition which is more and more used for frequency detection, in particular when combined with different types of neural networks [55], [56], [57].

3.2. MULTIVARIATE ALGORITHMS

Univariate methods have two main disadvantages as regards focal seizure detection. First, in these types of seizures, not every electrode is affected by the ictal pattern. It follows that missed detection can occur when the wrong electrodes are studied. Second,

they fail to incorporate the ictal spatial evolution and the synchronization of the signals typical of seizure activity. Multivariate methods solve these problems by basing the classification task on multiple electrodes. In this case, the feature to extract can express a statistical coupling between two different electrodes or come from one single recording. Figure 3.2 represents a classification for multivariate algorithms.

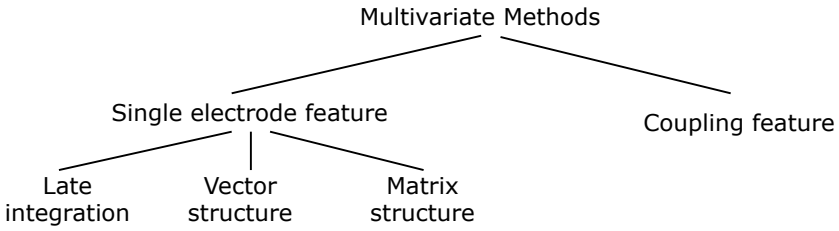

Figure 3.2: Scheme of the types of multivariate algorithms analyzed in this section. They are first divided by the type of feature extracted. We consider either single electrode features or coupling ones. We further classify this last group in late integration algorithms, vector structure storing and matrix structure storing.

SINGLE ELECTRODE FEATURES

Single electrode features are the same that can be studied in the univariate framework. The integration of information from different recordings is either at a late stage in the algorithm (late integration) or can happen early. Late integration comprises first a classification per single electrode. Then, the outputs of the classifiers are combined to give one unique label for the segments. One of the first algorithms for Epilepsy detection using EEG signals was a late integration algorithm developed in the 80s by Gotman [58] and was further improved later [59, 60]. The signals are first decomposed into a simpler representation called half-waves. Then, they segment the signals into segments for each electrode and investigate the set of frequencies ranging between 3 and 20Hz. After that, they devise a classifier per electrode. A seizure is detected if at least two electrodes detect ictal activity for the same segment or if two consecutive segments are labeled as ictal at the same or at a different electrode. Other methods convert the output of the single electrode classifiers into probabilities. The possible combination rules are multiple, i.e., maximum, minimum. and majority voting. The information from the different recordings can also be integrated early on in the pipeline of the algorithm. In this case, the features can either be stored (and processed) in a vector or a matrix. Shanir et al. exploit this first option in [61]. They extract an epoch's mean and minimum energy per electrode and store these features in a vector. Then, the proposed classifier receives this feature as input. In [62] 16 univariate features are extracted from the time and frequency domain and are then used as input of three different classifiers. They compare late integration methods to storing features in vectors and in a matrix structure. It results that, for the considered dataset, the matrix gives better results in terms of the ratio between sensitivity and specificity. The matrix structure better exploits the spatial information intrinsic in the recorded data. In [63] spectral information are captured from segments of EEG data and are stored in a matrix $\boldsymbol{X_t} \in \mathbb{R}^{p\times d}$. Here, p is the number of electrodes, d the number of features, and the index t refers to the number of segments. To better

capture the temporal evolution of the process, information coming from nearby non-overlapping segments is stored in matrix $\boldsymbol{X} = [\boldsymbol{X_{t-2}}\ \boldsymbol{X_t}\ \boldsymbol{X_{t+2}}]$. Then, this concatenated matrix is given as input to a classifier. This algorithm exploits spatial, frequency and temporal information in an innovative way.
Deep learning approaches also exploit univariate features. We report the work of Chatzichristos et al. [64] where they propose an algorithm exploiting 16 electrodes of scalp EEG. It consists of three attention U-net, a type of deep learning architecture [65]. Each U-net receives as input the EEG data that underwent different preprocessing steps to reduce noise. In the end, the output of the three deep learning structures is combined into one single element per input signal. In [66] they tailor the algorithm in order to exploit the spatial information behind the input time series. To this purpose, they use a Temporal Graph Convolutional Neural Network. Their focus is to reach high performance value while maintaining interpretability. Their model extracts feature over both time and space by integrating the knowledge of a graph underlying the connections. Furthermore, they couple the architecture with a model explainability tool to help clinicians understand the operation behind the architecture itself.
These methods all give promising results, but they are not suitable to model functional networks. In order to do so, we need coupling features. These can be interpreted as connections between brain areas.

COUPLING FEATURES

Coupling features capture statistical coupling between variables. In this way, it is possible to model the functional network that are altered during seizure (Section 2). Several of these measures exist [67]. Rana et al. [68] extract the so-called Phase Slope Index: a frequency domain feature which measures the synchronization between the signals recorded at sensors i and j. These values are stored in a matrix $\boldsymbol{P}$ of size $n_c \times n_c$ whose entry $p_{i,j}$ denotes the index between electrode i and j. Then, the sum of the index values per electrode is extracted as a feature. This representation underlays a graph structure: $\boldsymbol{P}$ can be interpreted as the adjacency matrix of a graph. However, one of the main challenges encountered in the construction of this graph from EEG signals is the presence of spurious coupling happening at electrode level, namely the volume conduction effect [69]. This means that the waveform recorded at electrode i is not only due to brain activity happening below that electrode but might suffer from corruption with signals coming from neighboring areas. In [70] Nolte et al. argue that the frequency domain feature called coherency is a solution to this problem. Coherency is a complex number and they mathematically prove how the imaginary part of coherency ($Im(Coh)$)is a direct measure of true interactions. In [71] $Im(Coh)$ is used to study the functional networks of prenatal children. In [72] a simpler metric is used in order to construct the graph: the autocorrelation. In particular, they set a hypothesis problem to learn the topology of the graph. The null hypothesis is the absence of a functional connection between signals recorded at electrodes i and j. On the contrary, the alternative hypothesis states the presence of an edge between i and j. First, they compute the maximum of the correlation between time series $x_i[t]$ recorded at i and $x_j[t]$ recorded at j. Then, with a particular analytic method called extremum method, they assign to each coupling measure a p-value which is a statistical parameter. In our case, the higher the p-value, the higher the evidence towards the presence of a connection. After that, they choose the de-

sired level of expected proportion of false connection and threshold the inferred edges accordingly. The interesting part of this method is that they give a statistical measure of the reliability of the inferred graph. In addition, testing the algorithm, they see that it can give similar performance if the autocorrelation metrics are directly thresholded with a value K. This means that there is a correlation between K and p. The final methodology is simple and is based on a probabilistic scheme. They then use a graph constructed in this fashion in order to detect seizures [73]. The algorithm is done on intracranial EEG data and showed graphs with more connection during the ictal event rather than the background one. In this work, we will use the last technique explained in order to build the graph.

3.3. COMMON EVALUATION METRICS

We cast the detection problem as a classification problem. The possible classes are positive P for seizure items; and N for negative items that are background events. The output of detector comprises: True Positives (TP) that are positive items that are classified as such; True Negative (TN) that are negative items that are classified as such; False Positive (FP) that are negative items that are classified as positive; False Negative (FN) that are positive items that are classified as negative.
Given this notation, we define the following three metrics that are often used in the literature of epilepsy detection:

- True positive rate also called sensitivity or recall which is defined as:

$$TPR = \frac{TP}{P} = \frac{\textit{Ictal segments correctly classified}}{\textit{Total ictal segments}} \tag{3.2}$$

- False positive rate also called specificity, which is defined as:

$$FPR = \frac{FP}{N} = \frac{\textit{Background segments not correctly classified}}{\textit{Total background segments}} \tag{3.3}$$

- Accuracy which is defined as:

$$accuracy = \frac{TP+TN}{F+N} = \frac{\textit{Segments correctly classified}}{\textit{Total number of segments}} \tag{3.4}$$

One of the main challenges of current seizure detection algorithms is to reduce the rate of false detection per hour [60, 74]. The target value is 10^{-3} false detections per hour. In this work, we focus only on Equations (3.2) and (3.3). In particular, we fix FPR to 10^{-3} to study the corresponding TPR values.

3.4. SUMMARY

In this chapter, we have seen different algorithms used for epilepsy detection in the literature. We have divided them by how they exploit the spatial information intrinsic in the EEG measurement. First, we explained some methodologies using recordings of only one electrode. We divide them further based on the type of feature extracted: from time

domain, frequency domain, or a combination of both. Then, we investigated the so-called multivariate algorithms that exploit information coming from multiple electrodes. In particular, we distinguish methods that use single electrode features such as the mean value of energy; from methodologies exploiting coupling features. These can model the functional networks that vary during the ictal event. Additionally, they can be expressed through graphs. We focus our attention on an algorithm constructing a graph structure from the autocorrelation between electrodes. This will be used as the base of our proposed algorithm. Lastly, we present three standard metrics that are used in the literature to evaluate seizure detection algorithms.

4

DATA AND METHOD

In this chapter, we present the details of the proposed framework for epilepsy detection. The main idea is to first construct a unique graph encoding the brain network organization before and during a seizure per each selected patient. Then, we study the difference in the spectrum of the ictal and non-ictal conditions on the obtained graph. With this information, we build a detector. Section 4.1 presents the EEG database used and the procedure followed for patient selection. After that, Section 4.2 details the new proposed patient-specific framework. Last, Section 4.3 provides a discussion on the chapter.

4.1. DATA

In this work, we used scalp EEG recordings from the Temple University Hospital EEG Data corpus: the world's largest publicly available EEG data corpus [75]. This comprises 30.000 clinical EEG data recorded from 2002 to the current year. Together with the recordings, it provides an annotation file where the clinician gives more detail about the patient's state during the recording and the type of epilepsy. The registrations can vary in temporal length, sampling frequency, which can have four different values (250Hz, 256Hz, 400Hz, and 512Hz), number, and location of the electrodes. Some reported electrodes measure activity not concerning the neural one. This is the case of the sensors for cardiac activity (EKG) and breath rhythm (RESP1 and RESP2), as can be seen in Figure 4.1. The database considers 30 possible events. Moreover, they identify each of these events through a class code which serves as a label. Each event is associated with a possible locality. In particular, the event can have a generalized spread; it can regard just one hemisphere; it can be focal; it can manifest in all the three mentioned conditions; or this information might not be available (N/A). Table 4.1 reports all the possible events with corresponding class code, locality, and a brief description. The corpus is split into subsets that focus on a specific group of events. In particular, this work leverages version v1.5.2 of the TUH EEG Seizure corpus (TUSZ). TUSZ supports deep learning research in automatic seizure detection [76]. In this database, out of the 30 labels present in the TUH corpus, only 13 are retained, and they regard just the different types of seizures [77]. The patterns that do not correspond to seizures are labeled as background (bckg).

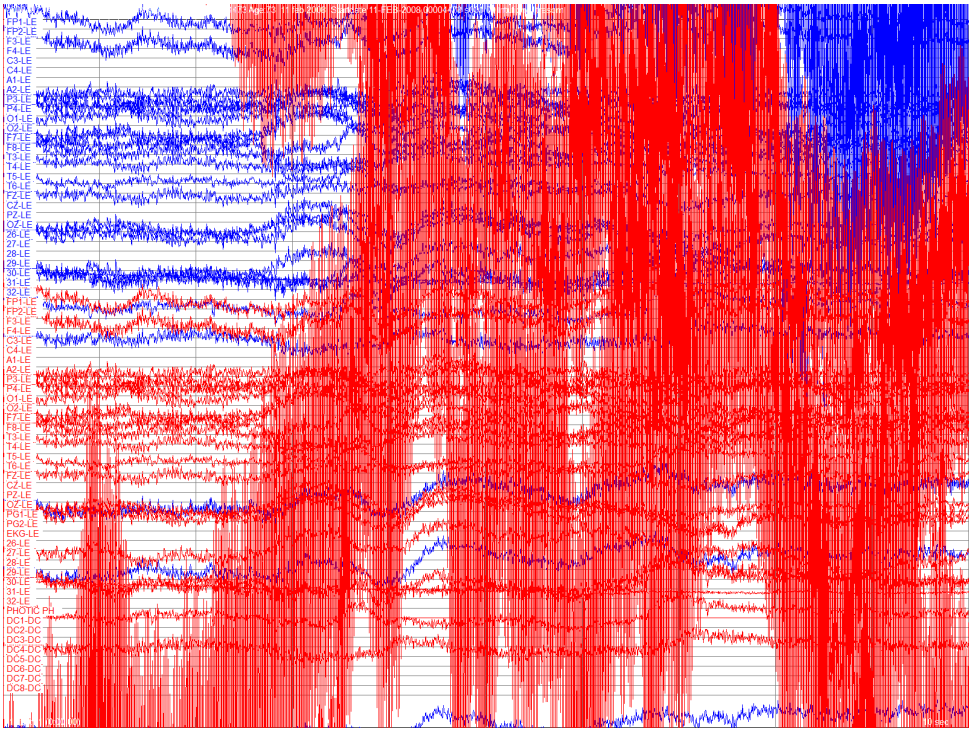

Figure 4.1: Piece of a session of EEG recording for a selected patient. Every line corresponds to a signal recorded at the electrode specified in the left part of the figure. Blue signals come from EEG recordings. In red are the signals of non-neural activities.

Table 4.1: Different events that are annotated in the TUH corpus. The implemented algorithm is developed with a smaller subset of the whole corpus: the TUSZ database. Here only 13 of the labels reported in this figure are used. Specifically TUSZ works with the 11 types of seizures (class numbers from 1 to 11) and the class codes *SEIZ* and *BCKG*. In light cyan the labels considered in this work.

Class Code	Event Name	Locality	Description
NULL	No Event	N/A	Unclassified event
SPSW	Spike/Sharp and Wave	All	Spike or wave and wave/complexes
GPED	Generalized Periodic Epileptiform Discharges	Generalized	Diffused periodic discharges
PLED	Periodic Lateralized Epileptiform Discharges	Hemispheric/Focal	Focal periodic discharges
EYBL	Eye Blink	Focal	Eye movement artifact corresponding to blinks
ARTF	Artifact (all)	All	Any non-brain activity electrical signal
BCKG	Background	N/A	Baseline/non-interesting events
HPHS	Hypnagogic Hypersynchrony	Generalized	A brief period of high amplitude slow waves.
SEIZ	Seizure	All	Common seizure class, include all types of seizure
TCSZ	Tonic Clonic Seizure	All	Seizure stiffening and then jerking of body
FNSZ	Focal Non-Specific Seizure	Hemispheric/Focal	Focal seizures cannot be specified with its type
INTR	Interesting Patterns	All	Any unusual or interesting patterns
SPSZ	Simple Partial Seizure	All	Partial seizures during consciousness
GNSZ	Generalized Non-Specific Seizure	Generalized	Generalized seizures cannot be further classified
CPSZ	Complex Partial Seizure	All	Partial Seizures during unconsciousness
ABSZ	Absence Seizure	Generalized	Absence Discharges observed on EEG
TNSZ	Tonic Seizure	All	Stiffening of body during seizure
CNSZ	Clonic Seizure	All	Jerking/shivering of body during seizure
ATSZ	Atonic Seizure	N/A	Sudden loss of muscle tone
MYSZ	Myoclonic Seizure	N/A	Myoclonous jerks of limbs
NESZ	Non-Epileptic Seizure	N/A	Any non-epileptic seizure observed.
SLOW	Slowing	All	A brief decrease in frequency
EYEM	Eye Movement Artifact	Focal	Artifact seen when the eyes move
CHEW	Chewing Artifact	All	Artifact corresponding to patient chewing, “bursty”
SHIV	Shivering Artifact	All	Artifact corresponding with patient shivering
MUSC	Muscle Artifact	All	Artifact that corresponds with agitation in a patient
ELPP	Electrode Pop Artifact	Focal	Artifact where channels spike with perfect symmetry
ELST	Electrostatic Artifact	All	Artifact of movement or interference on the electrodes
CALB	Calibration Artifact	All	Artifact caused by calibration of the electrodes.
TRIP	Triphasic Wave	Generalized	Large, three-phase waves

We clarify three main points regarding the selection of data from this database. First, in TUSZ, the signals are already divided into sets designed for training and testing purposes, namely "train" and "dev," respectively. However, we do not respect this split: we sample patients from both folders. Subjects in one folder are not always present in the second one, and this does not suit the patient-specific algorithm we aim to design (as will be clarified in the following section). Second, when recording an EEG signal, a differential voltage is taken per electrode with respect to a reference to reduce noise. TUSZ offers per recording three different versions where the reference signal varies. These are called different channel configurations. In particular, we can choose from: i) Average Reference (AR), where the average of the recorded signals serves as the reference; ii) Linked Ears Reference (LE) where a lead adapter linking left and right ear serves as the reference; and iii) AR_A files which leverage the AR configuration but discard the recordings of the auricular activity. LE is believed to reduce artifacts and, as a consequence, we exploit this channel configuration [78]. Last, in TUSZ, patients are distinguished and identified through a specific number. Moreover, for each patient, different sessions of EEG recordings can be present. Clinicians have already preprocessed each session: they split each session into sub-sessions and deleted those that are not relevant ones for seizure detection. Therefore, the corpus data are the cropped version of EEG sessions and are available in the European Data Format (EDF). For each session four types of annotations are present: "tse" files; "tse_bi" files; "lbl" and "lbl_bi". In this work, we leverage only the first two types of files. These are term-based annotations: they give a high-level view regarding at which time instant the seizure starts. To clarify, Figure 4.2 illustrates this concept. In addition, "bi" stands for bipolar annotations, which use only the "seiz" and "bckg" labels to classify the recording without specifying the type of seizure.

Patient selection happens in two main phases. First, "tse" files are analysed to find all patients suffering from focal seizure be it: i) non specific (label *fnsz*); ii) complex (label *CPSZ*); or iii) simple (label *SPSZ*). The ones with less than three seizure events across all recordings are discarded from this first set of subjects. A list of the seventeen selected patients with associated number and type of seizures follows in Table 4.2. Five selected patients suffer from complex seizure while all the others are annotated with non-specific seizures. We found no simple seizure in the considered version of the database.

```
version = tse_v1.0.0

0.0000 14.3320 bckg 1.0000
14.3320 188.0365 seiz 1.0000
188.0365 251.9720 bckg 1.0000
251.9720 317.4720 seiz 1.0000
317.4720 481.7640 bckg 1.0000
481.7640 598.1640 seiz 1.0000
598.1640 710.8280 bckg 1.0000
710.8280 878.3280 seiz 1.0000
878.3280 1077.0480 bckg 1.0000
1077.0480 1315.0480 seiz 1.0000
1315.0480 1590.5840 bckg 1.0000
1590.5840 1739.6509 seiz 1.0000
1739.6509 1750.0000 bckg 1.0000
```

(a)

```
version = tse_v1.0.0

0.0000 14.3320 bckg 1.0000
14.3320 188.0365 fnsz 1.0000
188.0365 251.9720 bckg 1.0000
251.9720 317.4720 fnsz 1.0000
317.4720 481.7640 bckg 1.0000
481.7640 598.1640 fnsz 1.0000
598.1640 710.8280 bckg 1.0000
710.8280 878.3280 fnsz 1.0000
878.3280 1077.0480 bckg 1.0000
1077.0480 1315.0480 fnsz 1.0000
1315.0480 1590.5840 bckg 1.0000
1590.5840 1739.6509 fnsz 1.0000
1739.6509 1750.0000 bckg 1.0000
```

(b)

Figure 4.2: Bipolar and non-bipolar term-based annotation (file extension "tse_bi") ,in a) and b) respectively, for EEG recording session of patient with identifier 258. From the third line on, an event is reported. In particular per row the first element represents the start of the event; the second position is reserved for the end time; the third entry regards the type of event and the last number is the probability of that annotation to be correct for that event. This last quantity is here always set to 1.

Table 4.2: Seventeen selected patients suffering from Focal Epilepsy. The number of total ictal events, their localization, and the temporal length of the non-seizure (background) and seizure events are also reported per subject. In particular, we obtain the information of the seizure localization by looking at the annotations file of the clinicians. These are part of the TUSZ database.

Patient identifier	Number of ictal events	Type of seizure	Localization	Time background	Time seizure
258	10	FNSZ	Right centrotemporal lobe	27.88min	22.06min
473	17	FNSZ	Left hemisphere	14.24min	6.06min
529	4	FNSZ	Left temporal region	43.69min	2.81min
1543	5	FNSZ	Left hemisphere, maximum in temporal region	11.47min	6.74min
2297	9	CPSZ	Right hemisphere. Difficult to localize	27.53min	12.23min
2806	18	FNSZ	Right hemisphere	33.92min	8.78min
3208	4	FNSZ	Right hemisphere	19.86min	5.56min
3636	17	FNSZ	Right hemisphere	11.88min	13.70min
3977	8	CPSZ	Very difficult to localize. Hypothesis of right occipital region.	8.95min	14.13min
4434	10	FNSZ	Left occipital region	16.66min	4.66min
4473	6	FNSZ	Left temporal region	41.89min	4.46min
5452	9	CPSZ	Not specified	34.51min	12.71min
5943	11	FNSZ	Right temporal region	9.99min	26.85min
6083	17	CPSZ	Right occipital region	39.50min	7.78min
6413	6	CPSZ	Right centrotemporal region	12.37min	7.14min
6507	7	FNSZ	Left hemisphere	10.44min	8.10min
7234	34	FNSZ	Right central parietal region.	6.75min	19.60min

Each session k of EEG data for each selected patient is organized in a matrix $\boldsymbol{X}_k \in \mathbb{R}^{n\_ch_k \times n\_t_k}$ with n_ch_k and n_t_k representing the number of channels and time samples for session k respectively. These sessions are collected in a list structure $\mathscr{X}$.

4.2. METHOD

The problem is cast into a classification task between background event (label 0) and the ictal one (label 1). Figure 4.3 gives an overview of the implemented pipeline. In Subsec-

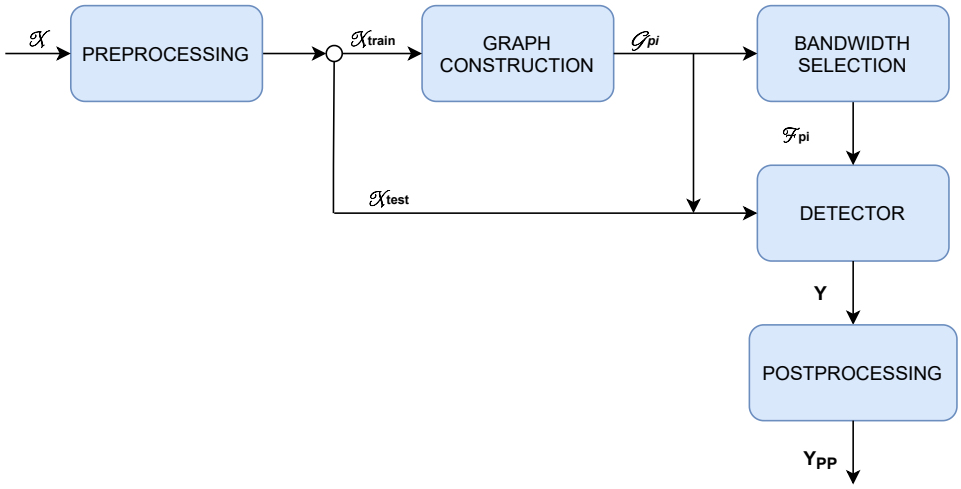

Figure 4.3: Pipeline of algorithm.The input data $\mathscr{X}$ is first preprocesed and then split into two subsets $\mathscr{X}_{train}$ and $\mathscr{X}_{test}$. The first set is used to construct a unique graph per patient and to select a bandwidth. With these two information the detector is built and applied to data in $\mathscr{X}_{test}$. The detector outputs a "0" for every interval of time classified as background. Conversely, the seizure events are labelled with a 1. These decisions are grouped in $\boldsymbol{Y}$. Finally, the output is post-processed and we get $\boldsymbol{Y}_{pp}$

tion 4.2.2 the input data $\mathscr{X}$ is preprocessed and split into a training $\mathscr{X}_{train}$ and testing $\mathscr{X}_{test}$ set. The first set is used to i) construct a unique graph $\mathscr{G}_{pi}$ of the brain organization under preictal activity (Subsection 4.2.2); and ii) select the bandwidth $\mathscr{F}$ of the most band-limited condition between the ictal and non-ictal one (Subsection 4.2.3). After that, Subsection 4.2.4 exploits $\mathscr{G}_{pi}$ and $\mathscr{F}$ to build a detector. The detector is applied to $\mathscr{X}_{test}$ and returns the labels in $\boldsymbol{y}$. Then, in Section 4.2.5, $\boldsymbol{y}$ is postprocessed to obtain $\boldsymbol{y_{pp}}$. The whole procedure is then repeated using a graph of the ictal activity $\mathscr{G}_i$.

4.2.1. DATA PREPROCESSING

Preprocessing encompasses six phases. First, we implemented a function selecting the common electrodes per patient. The sensors retained are the ones of the 10/20 configuration shown in Figure 4.4 except the auricular sensors A1 and A2. These last two are the reference electrodes of the chosen configuration and, as a consequence, we do not analyze them. For patients suffering from TLE also the electrodes $T1$ and $T2$ are present and retained. The location of these sensors is on the temporal lobe area slightly above the

eyes. Second, we upsample all the signals to the same sampling frequency $f_s = 400Hz$.

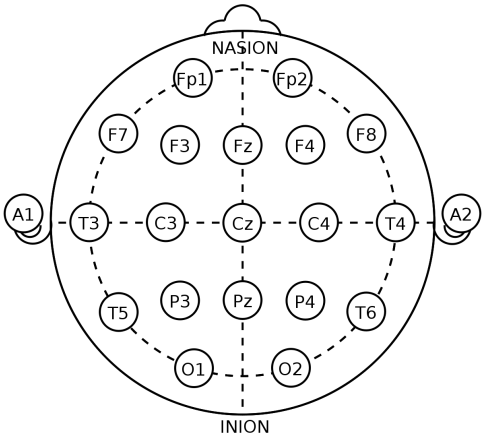

Figure 4.4: Electrodes of the configuration 10/20. These are the electrodes considered in the algorithm, except A1 and A2.

This value was chosen to resemble the methodology used in the chosen reference paper for the graph construction (Subsection 4.2.2) [7]. Third, a Butterworth band-pass filter of fourth order was applied between 1 and 50Hz to reduce noise. Fourth, we further divide the waves into 1s segments with 50% overlap with each other. Therefore, the first segment comprises 400 points going from 0s to 1s, while the second segment corresponds to the time instants going from 0.5s to 1.5s. After that, we discard all the preictal and ictal data that either started with the spurious, square-wave-like activity, reported in Figure 4.5 or for which one of the two events (background or seizure) lasted less than 10s. For this reason, after preprocessing, the number of ictal events per patient and the corresponding total background and seizure time might be reduced for some subjects. The final data are present in Table 4.3.
Last, we split the input data $\mathscr{X}$ into subsets $\mathscr{X}_{train}$, and $\mathscr{X}_{test}$. The split is made in terms of the number of background followed by seizure events, which we here call a cycle, occurring per patient. To be precise, we count the number of "seiz" entries in the "tse_bi" files for each patient. Then, we retain 60% of these events for training. We write in $\mathscr{X}_{train}$ all the time segments associated with the selected "seiz", together with the time samples of the "bckg" events happening immediately before. All the other samples are put into $\mathscr{X}_{test}$. Therefore, this last structure contains also data of recordings entirely comprised by background data. These are used to test the false alarm of the algorithm and cannot be used to construct the preictal graph. We remark that the temporal length of the two obtained subsets, namely $\mathbf{X}_{train}$ and $\mathbf{X}_{test}$, is different as the split was done just in terms of number of events. These steps are summarized in Figure 4.6.

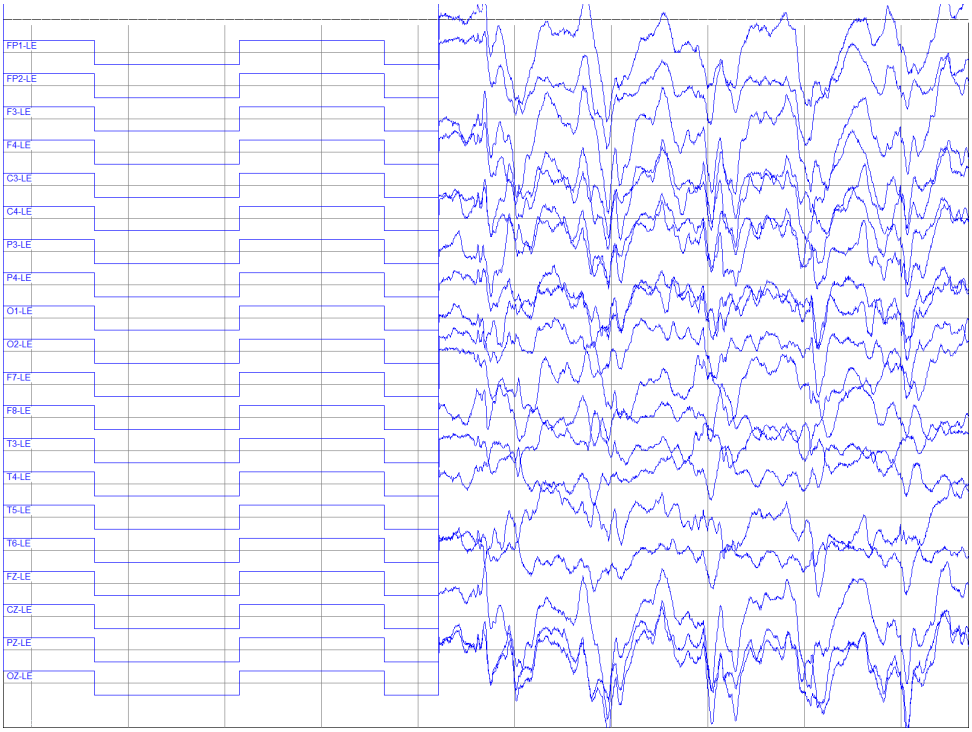

Figure 4.5: Spurious EEG signals not due to cerebral activity. This characterize the start of some recordings and might corrupt the result of the algorithm if it is not discarded.

Preprocessing

1. Selection of common electrodes per patient
2. Upsample signals to common sampling frequency
3. Band-pass filter
4. Divide signals into segments
5. Discard events with spurious activity or lasting less than 10s
6. Split data into training and testing sets

Figure 4.6: Summary of the six preprocessing steps encompassing the proposed algorithm.

Table 4.3: Data from the seventeen patients that have been selected from the TUSZ corpus after pre-processing. The number of total ictal events and the temporal length of the non-seizure (background) and seizure events are also reported per subject.

Patient identifier	Number of ictal events	Type of seizure	Time background	Time seizure
258	8	Focal Non-Specific Seizure	27.53min	18.21min
473	16	FNSZ	13.54min	5.41min
529	4	FNSZ	43.69min	2.81min
1543	4	FNSZ	11.31min	5.76min
2297	8	CPSZ	6.85min	11.74min
2806	18	FNSZ	13.77min	8.78min
3208	3	FNSZ	19.84min	4.68min
3636	14	FNSZ	11.84min	12.27min
3977	5	CPSZ	7.54min	9.35min
4434	8	FNSZ	11.64min	3.55min
4473	6	FNSZ	41.89min	4.46min
5452	6	CPSZ	30.93min	8.79min
5943	9	FNSZ	9.92min	22.68min
6083	11	CPSZ	38.60min	5.41min
6413	5	CPSZ	12.07min	6.43min
6507	4	FNSZ	7.73min	7.12min
7234	8	FNSZ	4.44min	3.43min

4.2.2. GRAPH CONSTRUCTION

For the graph construction, we apply to $\mathscr{X}_{train}$ the technique proposed in [7]. This is a relatively simple method and gives a measure of the reliability of the inferred edges as explained in the coupling features of Subsection . Each electrode is chosen as a node, while the edges require a slightly more complex procedure. First, we compute the Pearson correlation coefficient for each of the 20 segments before each ictal event for each pair of electrodes. To be precise, for segment k made of $n_s = 400$ samples, for cycle l and electrodes i and j we calculate the following value:

$$p_{i,j,k,l,\tau} = \frac{(\boldsymbol{x}_{i,k,l}(t) - \bar{x}_{i,k,l}(t)) \times (\boldsymbol{x}_{j,k,l}(t-\tau) - \bar{x}_{j,k,l}(t))}{\sigma_{i,k,l}\sigma_{j,k,l}} \tag{4.1}$$

Here $\boldsymbol{x}_{i,k,l}(t)$ is the segment k of cycle l at electrode i; $\bar{x}_{i,k,l}(t)$ is its mean value; $\boldsymbol{x}_{j,k,l}(t-\tau)$ is the segment k of cycle l recorded at electrode j and shifted in time of τ samples with $\tau \in [0; n_s]$; $\boldsymbol{x}_{j,k,l}(t))$ is the mean value of $x_{j,k,l}(t)$; $\sigma_{i,k,l}$ and $\sigma_{j,k,l}$ are the standard deviations of signals $x_{i,k}(t)$ and $x_{j,k}(t)$ k of cycle l respectively. It follows that, for a subject for which L cycles comprise $\mathscr{X}_{train}$, we retain $20 \times L \times n\_s$ Pearson correlation values for each pair of electrodes. Once this is done, the maximum absolute value of all the values corresponding to time shifts smaller or equal to 250ms $w_{max,i,j}$ is retained.

$$w_{max,i,j} = \max_{\tau \in [0;0.250 \times f_s[,\ k \in [0;20[,\ l \in [0;L[} p_{i,j,k,l,\tau} \tag{4.2}$$

We also calculate the time shift $\tau_{max,i,j}$ at which this maximum value occurs:

$$\tau_{max,i,j} = \operatorname*{argmax}_{\tau} p_{i,j,k,l,\tau};\ k \in [0;20[,\ l \in [0;L[\tag{4.3}$$

Then, a connection is designed for node i and node j with a weight $w_{i,j}$ equal to $w_{max,i,j}$ when: i) $w_{max,i,j}$ is higher than a chosen threshold K (parameter that will be studied later in the Results, Chapter 5) and ii) $\tau_{max,i,j}$ corresponds to a time shift smaller tan 150ms. In the opposite case, the two nodes are not connected with each other. The mathematical formulation follows:

$$w_{i,j} = \begin{cases} w_{max,i,j} & \text{if } w_{max,i,j} > K \wedge \tau_{max,i,j} < 0.150 * f_s, \\ 0 & \text{otherwise} \end{cases} \tag{4.4}$$

Last, we also construct the graph of the ictal activity $\mathscr{G}_i$ by taking into account the first 10s of each episode of ictal data.

We choose to construct the graphs of the preictal and ictal activities as we need a characteristic pattern of the patient. The background activity is not a suitable choice: first, we do not know the state of the subjects before the seizure (i.e., drowsiness, full alert), and these states can vary within the same recording. For instance, a patient could first be sleeping and then wake up with the occurrence of the seizure. As a consequence, we cannot build one unique graph of the background activity. Although the preictal and ictal patterns can vary severely for the same subject, they suit the unique graph approach.

4.2.3. BANDWIDTH SELECTION

For every time segment k of the structure $\mathcal{X}_{train}$ we consider a matrix $\boldsymbol{X}_k \in \mathbb{R}^{N \times n_s}$ with N number of electrodes for that patient. Row n of the matrix contains $\boldsymbol{x}_{n,k}$ that is the recording of segment k at electrode n. We project each matrix column on the eigenvectors of the chosen graph, first the preictal and then the ictal one. The obtained vectors are squared element-wise and summed together. For every segment k going from time instant t_0 to time instant t_1 the value obtained will be a vector $\hat{\boldsymbol{z}}_k \in \mathbb{R}^N$ as follows:

$$\hat{\boldsymbol{z}}_k = \sum_{t=t_0}^{t_1} (\boldsymbol{U}^H \boldsymbol{x}(t))^{\odot 2} \tag{4.5}$$

Here, $\boldsymbol{U}$ is the matrix of eigenvectors of the graph; $\boldsymbol{x}(t)$ is the vector of samples at time t at the various electrodes, and the symbol $^{\odot 2}$ represents element-wise square operation. In this way, $\hat{\boldsymbol{z}}_{\boldsymbol{k}}$ contains the energy of segment k for each graph frequency of the graph. Then, we stack these column vectors into one matrix $\hat{\boldsymbol{Z}}$. We normalize each column by the maximum of these values as:

$$\hat{\boldsymbol{z}}_k = \frac{\hat{\boldsymbol{z}}_k}{\max \hat{\boldsymbol{Z}}} \tag{4.6}$$

A second normalization follows as in Equation (4.7). This allows to have each segment with unitary 1-norm.

$$\hat{\boldsymbol{z}}_k = \frac{\hat{\boldsymbol{z}}_k}{|\hat{\boldsymbol{z}}_k|_1} \tag{4.7}$$

The first normalization re-scales the segments to comparable values. We remark that the elements in $\hat{\boldsymbol{Z}}$ are all positive, thanks to the square operation in Equation (4.5). Consequently, we do not need to take the absolute value of its maximum when computing the normalization. The reason behind the second normalization in Equation (4.7) will be more clear in the next part of this section.

Next, we use the tse annotation files to divide $\hat{\boldsymbol{Z}}$ into $\hat{\boldsymbol{Z}}_{bckg} \in \mathbb{R}^{N \times K_{bckg}}$ with K_{bckg} number of background segments and $\hat{\boldsymbol{Z}}_{ictal} \in \mathbb{R}^{N \times K_{ictal}}$ with K_{ictal} number of ictal segments. The first matrix contains the columns of $\hat{\boldsymbol{Z}}$ corresponding to background (non ictal) events. The remaining columns are stacked in $\hat{\boldsymbol{Z}}_{ictal}$. After that, we evaluate the average spectrum of the background $\bar{\boldsymbol{z}}_{bckg} \in \mathbb{R}^N$ as:

$$\bar{\boldsymbol{z}}_{bckg} = \frac{1}{K_{bckg}} \sum_{k=1}^{K_{bckg}} \hat{\boldsymbol{z}}_{bckg,k} \tag{4.8}$$

Where $\hat{\boldsymbol{z}}_{bckg,k}$ is the kth column of $\hat{\boldsymbol{Z}}_{bckg}$. In the same way we evaluate the average spectrum of the ictal condition as in Equation (4.9).

$$\bar{\boldsymbol{z}}_{ictal} = \frac{1}{K_{ictal}} \sum_{k=1}^{K_{ictal}} \hat{\boldsymbol{z}}_{ictal,k} \tag{4.9}$$

Where $\hat{\boldsymbol{z}}_{ictal,k}$ is the kth column of $\hat{\boldsymbol{Z}}_{ictal}$. After that, we order in a decreasing fashion the elements in $\bar{\boldsymbol{z}}_{bckg}$ and $\bar{\boldsymbol{z}}_{ictal}$ and select the first p values of each of the two arrays. This operation allows us to obtain the p^{th} percentage of the average bandwidth under

the two conditions. The hyperparameter p is later tuned and studied in Chapter 5. The algorithm for bandwidth selection produces $\mathscr{F}_{bckg}$ when $\hat{\boldsymbol{z}}_k = \hat{\boldsymbol{z}}_{bckg}$; $\mathscr{F}_{ictal}$ when $\hat{\boldsymbol{z}}_k = \hat{\boldsymbol{z}}_{ictal}$. For the remaining part of the algorithm we use as bandwidth $\mathscr{F}$ which is defined as in Equation (4.10)

$$\mathscr{F} = \begin{cases} \mathscr{F}_{bckg} & \text{if } |\mathscr{F}_{bckg}| < |\mathscr{F}_{ictal}| \\ \mathscr{F}_{ictal} & \text{if } |\mathscr{F}_{ictal}| < |\mathscr{F}_{bckg}| \\ \emptyset & \text{otherwise} \end{cases} \tag{4.10}$$

If the two bands have the same cardinality the algorithm cannot be applied further. When this is not the case, if $\mathscr{F} = \mathscr{F}_{bckg}$ the background condition is said to be the most band-limited one. In the opposite case, the ictal condition is said to be the most band-limited one.
We also consider the reliability of the inferred average spectrum under the two conditions. In particular we compute the variability of these two spectra looking at the standard deviation per Fourier component as:

$$\sigma_{bckg,k} = \sum_{i=1}^{K_{bckg}} (\hat{Z}_{bckg,i,k} - \bar{z}_{bckg,i})^2 \tag{4.11}$$

$$\sigma_{ictal,k} = \sum_{i=1}^{K_{ictal}} (\hat{Z}_{ictal,i,k} - \bar{z}_{ictal,i})^2 \tag{4.12}$$

Here, $\hat{Z}_{bckg,i,k}$ is the entry at the ith row and kth column of $\hat{\boldsymbol{Z}}_{bckg}$, while $\bar{z}_{bckg,i}$ is the ith entry of $\bar{\boldsymbol{z}}_{bckg}$. Similarly, $\hat{Z}_{ictal,i,k}$ is the entry at the ith row and kth column of $\hat{\boldsymbol{Z}}_{ictal}$, while $\bar{z}_{ictal,i}$ is the ith entry of $\bar{\boldsymbol{z}}_{ictal}$. In this way, we consider each frequency component as a random variable and, as a consequence, we compute the standard deviation over the columns. High values of $\sigma_{bckg,k}$ and $\sigma_{ictal,k}$ imply that the decided bandwidth $\mathscr{F}$ might not be robust.

4.2.4. BLIND GRAPH MATCHED DETECTOR

The detector exploits the preictal graph $\mathscr{G}_{pi}$ and the bandwidth $\mathscr{F}$ to classify $\mathscr{X}_{test}$ using the hypothesis testing procedure proposed in [79]. The rationale behind this detector is that there is a set of graph frequencies for which one condition (either background or seizure) has Fourier components that are negligible. At the same time, this does not hold for the other condition. Consequently, we develop a test T that checks the spectrum of the input signal at those specific frequencies and classifies accordingly.
We call the most band-limited condition, between background and ictal, H_0 or null hypothesis. We call the other condition H_1 or alternative hypothesis. Let us assume that H_0, for the chosen parameters K and p, is the background one. This case is portrayed in Figure 4.7. In this example $|\mathscr{F}| = 50$.

The rationale behind the detector is to exploit the set of frequencies $\bar{\mathscr{F}}_0$ for which the fourier components under H_0 are considered negligible. We call $\bar{\mathscr{F}}_0$ the complementary bandwidth and obtain as:

$$\bar{\mathscr{F}}_0 = \{l \quad | \forall\, l \notin \mathscr{F} \wedge l \in \text{diag}(\boldsymbol{\Lambda}_{\boldsymbol{pi}})\} \tag{4.13}$$

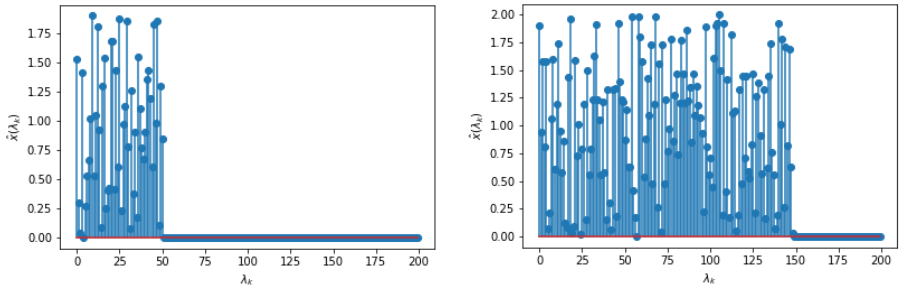

(a) (b)

4

Figure 4.7: Example of average spectrum under background and ictal condition. In (a) the bandwidth of the average spectrum of the background comprises the first 50 frequencies. The average ictal spectrum in (b) has a bandwidth made by the first 150 graph frequencies.

Here, diag($\boldsymbol{\Lambda_{pi}}$) is the diagonal of the matrix of eigenvalues of $\boldsymbol{L_{pi}}$. Now, given a new input segment k $\boldsymbol{X_{test}}(t) \in \mathbb{R}^{N \times n_s}$ we project it on $\mathcal{G}_{pi}$ as in Equation (4.5) and (4.6). In this way we obtain $\hat{\boldsymbol{z}}_{k,test}$. We call $\boldsymbol{z}_{k,test,\bar{\mathcal{F}}_0} \in \mathbb{R}^{|\bar{\mathcal{F}}_0|}$ the frequency components of $\hat{\boldsymbol{z}}_{k,test}$ defined on $\bar{\mathcal{F}}_0$. We assume that the recorded signal is the sum of true brain activity and noise $\boldsymbol{n}$ due to the recording process. Then, under H_0, $\hat{\boldsymbol{z}}_{k,test,\bar{\mathcal{F}}_0}$ shows negligible components. Under the alternative hypothesis, noise is added to brain signal activity $\hat{y}_{\bar{\mathcal{F}}_0}$. We write:

$$\begin{aligned} H_0 &: \hat{\boldsymbol{z}}_{k,test,\bar{\mathcal{F}}_0} = \hat{\boldsymbol{n}}_{\bar{\mathcal{F}}_0} \\ H_1 &: \hat{\boldsymbol{z}}_{k,test,\bar{\mathcal{F}}_0} = \hat{\boldsymbol{y}}_{\bar{\mathcal{F}}_0} + \hat{\boldsymbol{n}}_{\bar{\mathcal{F}}_0} \end{aligned} \tag{4.14}$$

Following the calculation in [79] the detector T_k for segment k is built as:

$$T_k = ||\hat{\boldsymbol{z}}_{k,test,\bar{\mathcal{F}}_0}||_2^2 \underset{H_0}{\overset{H_1}{\gtrless}} \gamma \tag{4.15}$$

In our example, Equation (4.15) means that when the energy of $\hat{\boldsymbol{z}}_{k,test,\bar{\mathcal{F}}_0}$ is below a certain threshold γ, we decide for the background condition. It follows:

$$y_i = \begin{cases} 0 & \text{if } T_k < \gamma \\ 1 & \text{otherwise} \end{cases} \tag{4.16}$$

Here, "0" is the label for background condition, "1" is the label for ictal condition and y_i stands for the i^{th} entry of the output vector $\boldsymbol{y}$. In the case where the most band-limited condition is the ictal one,the detector classifies a value of $\hat{\boldsymbol{z}}_{k,test,\bar{\mathcal{F}}_0} < \gamma$ as ictal. In this way, the detector provides a classification for every segment and hence second of data. We then repeat the same procedure using $\mathcal{G}_i$ instead of $\mathcal{G}_{pi}$. We remark that in [79] they assume that $\hat{\boldsymbol{y}}_{\bar{\mathcal{F}}_0}$ of Equation (4.14) is a deterministic quantity, while $\hat{\boldsymbol{n}}_{\mathcal{F}_0}$,and hence also $\hat{\boldsymbol{z}}_{k,test,\mathcal{F}_0}$, has a Gaussian distribution. However, this does not hold in this case.

In particular, if we consider just Equation (4.5), the null hypothesis of Equation (4.14) has a distribution of a noncentral Chi-Squared, while H_1 is distributed as a central Chi-Squared. Therefore, the corresponding detector would have a more complicated formulation. The normalizations of Equation (4.6) and Equation (4.7) complicate the distribution of the hypothesis testing. In particular, as we do not know the distribution of $\max \hat{\boldsymbol{Z}}$, the optimal detector is very complex. For this reason we use the simpler version in Equation (4.15).

4.2.5. DATA POSTPROCESSING

The output vector $\boldsymbol{y}$ can still be affected by outliers. For example, we know a priori that a label 1 surrounded by zeros is most likely the result of misclassification. In fact, that output implies a seizure lasting 1s that is not possible. For this reason, we use techniques of smoothing filters from digital image processing to process $\boldsymbol{y}$. In particular, we define the validity of the output label y_k of segment k considering a window of $win = 20$ segments, centered at k. Then, we count the number of ictal labels in that window. If this number is greater than $positive = 16$, we classify segment k as ictal and $y_{pp,k} = 1$. Conversely, we label $y_{pp,k} = 0$. The chosen value for win corresponds to 10s, the minimum duration of an ictal event for the considered data. Instead, 16 segments correspond to 8s, and it is a value found in the literature [80]. Therefore, the proposed postprocessing algorithm needs 8s of seizure data to classify the considered 10s window as a seizure.

4.3. DISCUSSION

In this chapter, we selected seventeen patients with focal Epilepsy from the TUSZ corpus. This database contains EEG recordings annotated for seizure events. Then, we developed a patient-specific algorithm for each patient. First, we preprocess data to reduce noise and split it into two subsets: one for training and one for testing purposes. We work with segments of 1s where we assume stationarity. The segments of the training set are first used to construct a graph of the preictal and ictal activity of the patient. In this graph, we associate a node to each electrode of the EEG recordings while we build the edges using the Pearson coefficient between pairs of sensors. After that, we investigate the most band-limited condition on the preictal graph, between the background (non-ictal) and ictal one. The implemented detector works on the testing segments and analyzes their Fourier components on the frequencies that do not comprise the decided bandwidth. If the calculated value is below a certain threshold, we classify the segment with the label of the most band-limited condition. Then, we repeat the last two steps using the ictal graph. Two hyperparameters emerge in this chapter: K, a threshold for edge existence; and p, the percentage of bandwidth considered.
We now make remarks regarding the type of algorithm used, split of the data, the choice for graph construction, and parameter tuning.

First, many studies attest that an approach to seizure detection and prediction that is patient specific help reduce the rate of false alarm as it better models the EEG patterns that are specific to an individual [74, 81, 82]. However, the downside of this approach is that the algorithm implemented cannot be used in a clinical environment where a new patient can arrive. In fact, we need to have already some data on the subject to construct

the graph and select the bandwidth.

Second, the training and testing sets are split not in terms of the number of segments but the number of seizures present. As a consequence, we do not know a priori which set is going to have more segments. Furthermore, given the scarcity of ictal data, there can be an uneven distribution of the data in the two subsets.

Third, we choose the Pearson correlation coefficient as a metric to construct the graph for its simplicity. Furthermore, the implemented method was proven to give a measure of reliability over the inferred edges [70]. However, it does not consider the presence of spurious coupling between electrodes which are a consequence of the recording system. Future work to implement the algorithm could see a graph implementation using the imaginary part of the so-called coherency metric. We also remark that it would have been better to construct a graph of the background activity as it is abundant in the database in contrast to the ictal condition and, consequently, to the preictal one. Still, the background activity of the signals under analysis represents different states that are not annotated and vary both from session to session and within the same session. For this reason, we cannot construct one unique background graph. On the contrary, we must rely on an activity that is relatively constant through all the recordings. Hence, our choice on the preictal and ictal activity.
Furthermore, the constructed detector is not optimal as it assumes probability distributions that do not precisely match the ones of the considered hypothesis testing. Nevertheless, we use this simpler solution.

Last, we remark that the amount of data present for each patient is, on average, minimal. This encompasses two main issues for hyperparameter tuning. First, the problem requires three different sets:

1. Training set used to build the model
2. Validation set used to fine-tune the model
3. Testing set used to evaluate the model

However, for some subjects, we have less than 7 minutes of recordings. In general, the amount of data we have at our disposal forces us to work with only two splits, not more. As a consequence, we stop at the second level of this procedure.

5

RESULTS

This chapter provides the numerical analysis performed on the data . In particular Section 5.1 presents the specifics for the evaluation procedure; Section 5.2 the results and Section 5.3 reports a discussion on the obtained results.

5.1. EVALUATION SPECIFICS

We study the performance of the algorithm with the Receiver Operating Characteristic (ROC) curves. These are simple to calculate and have been extensively exploited in detection theory to evaluate the performance of detectors [83]. ROC curves depict the TPR of a detector as a function of its FPR. The integral of the curve is called Area Under the Curve (AUC) and is also used to evaluate the proposed detector. In particular an ideal classifier shows a constant ROC at 1 ($AUC = 1$); a random classifier has a ROC curve with equation $TPR = FPR$ ($AUC = 0.5$); a classifier depicting all ictal segments as background (opposite polarization) shows a constant ROC at 0 ($AUC = 0$). The ROC curves are calculated using the efficient algorithm proposed in [84]. Two more things need to be specified before looking at the final results.

First, we need to tune K and p. We select a set of possible values for these hyperparameters and compute the ROC curve for each combination of these values. In particular we test the algorithm on:

$$K = [0.7, 0.75, 0.8, 0.85, 0.9] \tag{5.1}$$

$$p = [0.7, 0.75, 0.8, 0.85, 0.9, 0.95] \tag{5.2}$$

The values of K are experimentally chosen in order to have reasonable results: too high values correspond to a graph with no connection, while a fully connected graph is obtained for low K. a proper cross-validation strategy requires repeating training and testing more times and on different splits of the complete recordings. The average performance of the splits would then indicate the reliability of the algorithm. This cannot be applied here for two reasons: i) we want to observe the inferred graph under preictal and ictal condition and the average operator on the graph is ambiguous; ii) the ROC curves

evaluated have a number of points equal to the number of samples in the testing set which changes for different splits. This last point implies that taking the average of the curves requires specific techniques, like interpolation. However, we choose not to do this for complexity reasons. Instead, we opted for repeating the split into training and testing data three times. It follows that for the same patient, we now have three different simulations (folds) of the performance of the hyperparameters. The data we report here correspond to the pair of (K, p) giving the highest AUC per fold. Second, we compare the performance of the proposed method with three other algorithms which we call baselines. In this way we study the relevance of our detector. The first baseline algorithm does not learn the graph from the recordings but uses a complete graph where each node is connected to every other node. Instead, the second baseline detector does not select a subset of frequencies for the bandwidth but look at the whole set frequencies. In this case we assume $test = bckg$ where $test$ denotes the most band-limited condition. If the corresponding ROC curves are below the line of $TPR = FPR$, then $test = seiz$. The very last baseline is a single electrode detector computing the square norm two of per each segment k and electrode i as in:

$$T_i = ||\hat{\boldsymbol{x}}_{i,k}||_2^2 \underset{bckg}{\overset{seiz}{\gtrless}} \gamma \tag{5.3}$$

We perform the calculations using first the preictal and then the ictal graph. Lastly, we investigate the topology of the inferred preictal and ictal graphs. In particular, we investigate the degree matrix of the graphs with the best combination of the hyperparameters for the patient. We expect to find a difference in the density of connections around the onset of the seizure. We take Table 4.2 as a reference for the localization of the ictal events.

5.2. NUMERICAL RESULTS

Table 5.1 depicts the amount of data present for each present per fold. In particular, there sometimes is a strong imbalance between ictal and background data in the training set. Furthermore, the number of samples in training and testing data can vary from fold to fold. Next, Table 5.2 and Table 5.3 report the best AUC value per fold when using the preictal and ictal graph, respectively. We notice that our proposed method gives good performances ($AUC > 0.8$) for seven out of the seventeen subjects. In particular, for some subjects, the use of the preictal graph gives slightly better average results than the ictal graph (Table 5.4). However, it always has a performance comparable with the single electrode baseline.

Table 5.1: The table presents the number of minutes used for training and testing for each subject and for the three different folds. In particular we distinguish the number of background instants (bckg) and the seizure ones (seiz).

id	Fold 1				Fold 2				Fold 3			
	train		test		train		test		train		test	
	bckg	seiz	bckg	seiz	bckg	seiz	bckg	seiz	bckg	seiz	bckg	seiz
258	19.00min	10.00min	8.53min	8.22min	17.69min	12.88min	9.84min	5.33min	12.31min	9.00min	15.22min	9.21min
473	8.49min	3.29min	5.05min	2.12min	6.79min	3.58min	7.45min	2.48min	9.43min	3.69min	4.81min	2.37min
529	7.36min	0.81min	36.33min	2.00min	15.96min	2.00min	27.73min	0.81min	17.87min	1.40min	25.82min	1.41min
1543	4.54min	2.79min	6.77min	2.97min	4.24min	2.03min	7.07min	3.73min	5.15min	2.29min	6.17min	3.48min
2297	4.97min	7.54min	21.74min	4.20min	2.76min	5.93min	23.96min	5.80min	2.49min	4.76min	24.22min	6.98min
2806	9.58min	4.95min	4.19min	3.83min	7.50min	5.44min	6.27min	3.34min	8.33min	4.92min	5.44min	3.86min
3208	8.34min	3.54min	11.51min	2.02min	16.00min	4.27min	3.86min	1.29min	15.39	4.19min	4.47min	1.37min
3636	5.12min	6.85min	9.51min	6.96min	7.26min	5.66min	4.58	6.61min	7.12min	5.03min	4.72min	7.23min
3977	4.00min	4.34min	3.54min	5.01min	5.08min	6.01min	2.46min	3.34min	4.54min	6.02min	3.00min	3.32min
4434	11.71min	3.38min	4.68min	1.29min	10.03min	2.62min	6.36min	2.04	11.72min	2.73min	4.67min	1.93min
4473	6.55min	2.93min	74.41min	1.52min	12.12min	3.10min	68.84min	1.36min	9.35min	2.89min	71.61min	1.57min
5452	15.74min	7.62min	18.77min	5.09min	5.33min	3.47min	25.60	5.32min	9.14min	3.01min	21.79min	5.78min
5943	4.38min	12.61min	5.55min	10.07min	6.33min	11.81min	3.59min	10.87min	4.19min	14.01min	5.73min	8.67min
6083	4.81min	3.56min	33.79min	1.86min	8.34min	3.48min	30.26min	1.93min	10.45min	2.86min	28.16min	2.55min
6413	7.91min	3.43min	4.16min	3.00min	7.73min	3.75min	4.34min	2.68min	6.86min	3.84min	5.21min	2.59min
6507	7.16min	3.32min	0.57min	3.80min	0.57min	3.80min	7.16min	3.32min	4.76min	3.24min	2.97min	3.88min
7234	2.89min	2.14min	1.54min	1.29min	2.66min	2.10min	1.78min	1.33min	2.70min	2.15min	1.73min	1.28min

Table 5.2: Area Under Curve of the seventeen patients. Data are reported for each of the three folds on the preictal graph and after post-processing. Here AUC_proposed are the values obtained by the proposed method; AUC_all indicates the performance of the detector working with the complete graph; AUC_complete are the AUC value obtained when using a complete graph instead of inferring it from data; AUC_se is instead the best performance of the single electrode detectors.
When the algorithm cannot be applied, for equal bandwidth of the background and ictal condition, we use the symbol "-" . The values are color-coded: cyan for a cell with AUC < 0.4; red for 0.4 ≤ AUC < 0.6; yellow for 0.6 ≤ AUC < 0.8; green for AUC ≥ 0.8.

Patient	AUC_proposed			AUC_all			AUC_complete			AUC_se					
identifier	fold 1	fold 2	fold 3	fold 1	fold 2	fold 3	fold 1	fold 2	fold 3	fold 1	ch	fold 2	ch	fold 3	ch
258	0.78	0.73	0.72	0.47	0.43	0.48	0.67	-	0.73	0.82	T4	0.85	T4	0.69	O1
473	0.77	0.64	0.77	0.78	0.69	0.76	-	0.52	-	0.75	F4	0.74	F4	0.71	FZ
529	0.97	0.94	0.98	0.09	0.73	0.93	0.91	0.95	0.97	0.92	P3	0.85	T5	0.96	O1
1543	0.77	0.73	0.60	0.53	0.55	0.52	-	0.68	0.63	0.75	O1	0.72	O1	0.69	O1
2297	0.97	0.97	0.97	0.92	0.83	0.93	0.05	0.92	0.93	0.89	CZ	0.90	CZ	0.68	CZ
2806	0.71	0.77	0.69	0.65	0.69	0.57	-	0.44	-	0.80	T3	0.86	T3	0.75	F4
3208	0.93	0.89	0.75	0.63	0.84	0.66	0.90	-	0.07	0.99	C4	0.86	C4	0.86	FZ
3636	0.95	0.93	0.93	0.69	0.71	0.46	0.81	0.75	0.78	0.98	O2	0.97	O2	0.98	O2
3977	0.86	0.95	0.97	0.66	0.62	0.68	0.82	0.92	0.97	0.99	T6	0.98	PZ	0.99	PZ
4434	0.80	0.80	0.82	0.72	0.80	0.81	0.88	0.57	0.88	0.61	PZ	0.69	C3	0.70	T3
4473	0.98	0.99	0.97	0.96	0.99	0.96	0.96	-	0.97	0.91	O1	0.91	O2	0.85	O1
5452	0.69	0.65	0.78	0.63	0.55	0.74	0.64	0.59	0.36	0.76	T3	0.73	T3	0.77	T3
5943	0.77	0.81	0.85	0.45	0.51	0.37	0.83	0.82	0.84	0.94	T1	0.91	T4	0.93	F8
6083	0.83	0.83	0.92	0.67	0.62	0.64	-	0.72	0.47	0.67	O1	0.70	T6	0.85	O1
6413	0.73	0.49	0.90	0.89	0.86	0.89	0.30	0.31	0.80	0.88	PZ	0.87	PZ	0.86	PZ
6507	0.57	0.64	0.79	0.58	0.49	0.72	0.71	-	0.74	0.73	C3	0.77	T3	0.81	T3
7234	0.76	0.77	0.69	0.74	0.69	0.68	0.44	0.61	0.37	0.74	P4	0.69	P4	0.75	O1

Table 5.3: Area Under Curve of the seventeen patients. Data are reported for each of the three folds on the ictal graph and after post-processing. Here AUC_proposed are the values obtained by the proposed method; AUC_all indicates the performance of the detector working with the complete graph; AUC_complete are the AUC value obtained when using a complete graph instead of inferring it from data; AUC_se is instead the best performance of the single electrode detectors.
When the algorithm cannot be applied, for equal bandwidth of the background and ictal condition, we use the symbol "-" . The values are color-coded: cyan for a cell with AUC < 0.4; red for 0.4 ≤ AUC < 0.6; yellow for 0.6 ≤ AUC < 0.8; green for AUC ≥ 0.8.

Patient	**AUC_proposed**			**AUC_all**			**AUC_complete**			**AUC_se**					
identifier	**fold 1**	**fold 2**	**fold 3**	**fold 1**	**fold 2**	**fold 3**	**fold 1**	**fold 2**	**fold 3**	**fold 1**	**ch**	**fold 2**	**ch**	**fold 3**	**ch**
258	0.75	0.80	0.75	0.58	0.56	0.62	0.67	-	0.73	0.82	T4	0.85	T4	0.69	O1
473	0.79	0.73	0.66	0.70	0.82	0.67	-	0.52	-	0.75	F4	0.74	F4	0.71	FZ
529	0.96	0.93	0.97	0.56	0.82	0.88	0.91	0.95	0.97	0.92	P3	0.85	T5	0.96	O1
1543	0.75	0.79	0.69	0.67	0.58	0.51	-	0.68	0.63	0.75	O1	0.72	O1	0.69	O1
2297	0.97	0.97		0.93	0.88		0.05	0.92		0.89	CZ	0.90	CZ	0.68	CZ
2806	0.74	0.74	0.57	0.64	0.69	0.52	-	0.44	-	0.80	T3	0.86	T3	0.75	F4
3208	0.91	0.73	0.70	0.85	0.78	0.52	0.90	-	0.07	0.99	C4	0.86	C4	0.86	FZ
3636	0.95	0.95	0.90	0.73	0.78	0.51	0.81	0.75	0.78	0.98	O2	0.97	O2	0.98	O2
3977	0.86	0.97	0.98	0.65	0.77	0.88	0.82	0.92	0.97	0.99	T6	0.98	PZ	0.99	PZ
4434	0.79	0.71	0.77	0.72	0.79	0.77	0.88	0.57	0.88	0.61	PZ	0.69	C3	0.70	T3
4473	0.99	0.99	0.97	0.97	0.99	0.96	0.96	-	0.93	0.91	O1	0.91	O2	0.85	O1
5452	0.72	0.60	0.76	0.65	0.55	0.74	0.64	0.59	0.36	0.76	T3	0.73	T3	0.77	T3
5943	0.88	0.83	0.79	0.48	0.44	0.65	0.83	0.82	0.84	0.94	T1	0.91	T4	0.93	F8
6083	0.90	0.91	0.55	0.73	0.69	0.74	-	0.72	0.47	0.67	O1	0.70	T6	0.85	O1
6413	0.92	0.44	0.93	0.89	0.66	0.91	0.30	0.31	0.80	0.88	PZ	0.87	PZ	0.86	PZ
6507	0.78	0.71	0.80	0.75	0.80	0.80	0.71	-	0.74	0.73	C3	0.77	T3	0.81	T3
7234	0.85	0.73	0.70	0.78	0.67	0.71	0.44	0.61	0.37	0.74	P4	0.69	P4	0.75	O1

Table 5.4: Mean AUC between folds, for the ictal and preictal graph. In bold the highest AUC value per row.

Patient identifier	Mean AUC preictal graph	Mean AUC ictal graph
258	0.74	**0.76**
473	**0.79**	0.73
529	0.95	**0.96**
1543	0.70	**0.78**
2297	**0.97**	**0.97**
2806	**0.72**	0.68
3208	**0.86**	0.78
3636	**0.94**	0.93
3977	**0.96**	0.94
4434	0.53	**0.76**
4473	**0.98**	**0.98**
5452	**0.70**	0.69
5943	0.81	**0.83**
6083	**0.86**	0.78
6413	0.71	**0.76**
6507	0.67	**0.76**
7234	0.74	**0.76**

Table 5.5 and **??** report the pair of hyperparameters giving best performance for the different´folds, first on the preictal and then the ictal graph. We not how the best pair of hyperparameters is not robust per fold. Moreover, there is a great variability also between patients.

5.3. DISCUSSION

The performance of the proposed method is strongly dependent on the average spectrum of the background and ictal conditions. The ROC curves give good performance when these two spectra are the same, and the standard deviation for each Fourier component is low. Although our algorithm outperforms the two graph-based baselines, it does not perform better than the single electrode. We suspect that integrating knowledge regarding the frequency evolution of the ictal patterns could enhance the performance. Moreover, some ROC curves we have not reported here show an S-like shape. Consequently, the data we are working with are too complex for a classification based on this feature alone.

Next, to study the performance of the hyperparameters, we have repeated the splits of training and testing sets three times. Another possible alternative would have been to use the training data to select K and p to use them for the testing set. However, in both cases, we cannot properly tune the hyperparameters. The different number of samples present for fold does not allow us to do that. Our methods allow instead to test how robust the hyperparameters are for the different folds. Usually, we have more background

Table 5.5: Hyperparameters giving the best AUC for each fold and patient, when using the preictal graph.

Patient Identifier	**k1**		**k2**		**k3**	
	K	p	K	p	K	p
258	0.75	0.8	0.9	0.95	0.9	0.95
473	0.8	0.7	0.8	0.9	0.85	0.8
529	0.85	0.95	0.85	0.8	0.85	0.85
1543	0.7	0.7	0.85	0.7	0.85	0.7
2297	0.85	0.85	0.9	0.9	0.7	0.9
2806	0.85	0.85	0.85	0.95	0.85	0.95
3208	0.85	0.7	0.9	0.95	0.85	0.8
3636	0.7	0.95	0.7	0.9	0.9	0.7
3977	0.8	0.95	0.75	0.75	0.85	0.9
4434	0.85	0.9	0.85	0.8	0.7	0.7
4473	0.75	0.95	0.7	0.95	0.7	0.95
5452	0.9	0.95	0.85	0.95	0.85	0.9
5943	0.8	0.95	0.7	0.8	0.75	0.9
6083	0.7	0.85	0.9	0.8	0.7	0.8
6413	0.9	0.85	0.85	0.85	0.75	0.8
6507	0.8	0.95	0.7	0.95	0.9	0.75
7234	0.9	0.85	0.8	0.75	0.9	0.85

data than ictal one. Consequently, in a database with hours of recordings per patient, we could discard background data to have a constant number of data per different folds. In that case, we could adequately cross-validate the algorithm.
Regarding the graph, we could guess the location of the epileptogenic zone by looking at the nodes of the preictal and ictal graphs with lower degrees. This implies that the areas involved with the onset have lower autocorrelation values. We are aware that this methodology is quite naive for three main reasons. First, the localization is not precise as based on 21 electrodes. Consequently, we can only indicate the hemisphere involved with the onset but not a specific region. Second, the autocorrelation is quite a simple measure, and it was sometimes difficult to see a definite change in the graph's structure. Third, sometimes the onset characteristic could be inferred from the preictal graph, some other times from the ictal one. This indicates the lack of a proper structure to follow.

6

CONCLUSION

This chapter concludes the work of this research project. Section 6.1 summarizes the work done with a focus on the method and results. We address the answer to the posed research questions in Section 6.2 while Section 6.3 proposes two future works.

6.1. THESIS SUMMARY

In this thesis, we proposed a new framework for focal epilepsy detection. In particular, the novelty of our algorithm lies in the fusion of a technique for topology inference of graph [7] and a blind detector using a difference in graph signal bandwidth over the ictal and background conditions. Chapter 2 and Chapter 3 provided the basic background of our research and the current methods for epilepsy detection. Then, we explain the core of the algorithm and the selection of the used data in Chapter 4. Last, in Chapter 5 we compare the performance of the proposed algorithm with other two graph-based methods and a simple energy detector using just one electrode. The algorithm never outperforms the single electrode detector, but it still gives good performance in terms of AUC for seven out of the seventeen studied subjects. Furthermore, we can give a basic guess of the hemisphere involved in the seizure onset by looking at the inferred ictal and preictal graphs.

6.2. ANSWER RESEARCH QUESTION

The first research question we posed at the beginning of this work was:

RQ1. Can these alterations in brain connectivity patterns be modeled and then used to detect an incoming seizure?

We exploit EEG recordings to build two graphs per patient to address this question: one for the preictal and one for the ictal activity. The proposed framework allows. In particular, for the only patient with slightly more than 1 hour of data, we obtain a FPR of 0.25 for TPR of 0.5.

RQ2. Can we gain more insights regarding the localization of the seizure onset by the inferred model?

The inferred graphs show a lower density of edges, and hence, lower degrees, around the nodes involved with the seizure for most subjects. However, we cannot identify precisely the epileptogenic zone.

6.3. FUTURE WORKS

To conclude this research, we propose three possible future works that could enhance the performance of the proposed framework and, at the same time, give better insights into the epileptogenic zone and into disorder in general.

1. The algorithm could be tested on a graph evaluated with a different metric as coherency. As mentioned in Section 3.2 coherency can model better the real connection of brain areas. This would allow studying whether and how the performance of our algorithm change using this approach. Furthermore, we could compare the degree matrices obtained in this way with the ones obtained in this work. In this way, we might better guess the seizure onset by considering areas with low degrees in all the graphs.

2. In this work, we did not exploit the temporal frequency components of the ictal pattern. Therefore, we could extract a second feature from the temporal frequency domain. Concretely, it would be interesting to work both with the GFT and the DFT operators. In this way, we could study the temporal frequencies providing non-negligible graph Fourier components.

3. The algorithm could be extended with a machine learning approach. In particular, a four-class classification algorithm could be investigated. Here the four classes would be interictal, preictal, ictal, and postictal.

BIBLIOGRAPHY

[1] Hanneke M De Boer, Marco Mula, and Josemir W Sander. "The global burden and stigma of epilepsy". In: *Epilepsy & behavior* 12.4 (2008), pp. 540–546.

[2] Michael R Sperling. "The consequences of uncontrolled epilepsy". In: *CNS spectrums* 9.2 (2004), pp. 98–109.

[3] DE Blum et al. "Patient awareness of seizures". In: *Neurology* 47.1 (1996), pp. 260–264.

[4] Yushi Inoue and Tadahiro Mihara. "Awareness and responsiveness during partial seizures". In: *Epilepsia* 39.S5 (1998), pp. 7–10.

[5] Christian E Elger and Christian Hoppe. "Diagnostic challenges in epilepsy: seizure under-reporting and seizure detection". In: *The Lancet Neurology* 17.3 (2018), pp. 279–288.

[6] Mark A Kramer and Sydney S Cash. "Epilepsy as a disorder of cortical network organization". In: *The Neuroscientist* 18.4 (2012), pp. 360–372.

[7] Mark A Kramer, Eric D Kolaczyk, and Heidi E Kirsch. "Emergent network topology at seizure onset in humans". In: *Epilepsy research* 79.2-3 (2008), pp. 173–186.

[8] Barbara C Jobst and Gregory D Cascino. "Resective epilepsy surgery for drug-resistant focal epilepsy: a review". In: *Jama* 313.3 (2015), pp. 285–293.

[9] Gagandeep Singh and Josemir W Sander. "The global burden of epilepsy report: implications for low-and middle-income countries". In: *Epilepsy & Behavior* 105 (2020), p. 106949.

[10] Carl E Stafstrom and Lionel Carmant. "Seizures and epilepsy: an overview for neuroscientists". In: *Cold Spring Harbor perspectives in medicine* 5.6 (2015), a022426.

[11] Pierluigi Bertora. *Neurologia: per i corsi di laurea in professioni sanitarie*. Piccin, 2015.

[12] Allan Krumholz. "Nonepileptic seizures: diagnosis and management." In: *Neurology* 53.5 Suppl 2 (1999), S76–83.

[13] Markus Reuber and Christian E Elger. "Psychogenic nonepileptic seizures: review and update". In: *Epilepsy & Behavior* 4.3 (2003), pp. 205–216.

[14] Taoufik M Alsaadi and Anna Vinter Marquez. "Psychogenic nonepileptic seizures". In: *American family physician* 72.5 (2005), pp. 849–856.

[15] Robert S Fisher et al. "ILAE official report: a practical clinical definition of epilepsy". In: *Epilepsia* 55.4 (2014), pp. 475–482.

[16] Jerome Engel Jr. "ILAE classification of epilepsy syndromes". In: *Epilepsy research* 70 (2006), pp. 5–10.

[17] Jerome Engel Jr. “A practical guide for routine EEG studies in epilepsy.” In: *Journal of clinical neurophysiology: official publication of the American Electroencephalographic Society* 1.2 (1984), pp. 109–142.

[18] Felix Rosenow, Karl Martin Klein, and Hajo M Hamer. “Non-invasive EEG evaluation in epilepsy diagnosis”. In: *Expert review of neurotherapeutics* 15.4 (2015), pp. 425–444.

[19] Sebastian Nagel. “Towards a home-use BCI: fast asynchronous control and robust non-control state detection”. PhD thesis. Universität Tübingen, 2019.

[20] Frederic A Gibbs, Emma L Gibbs, and Williams G Lennox. “Epilepsy: a paroxysmal cerebral dysrhythmia”. In: *Epilepsy & behavior* 3.4 (2002), pp. 395–401.

[21] Borbála Hunyadi et al. “A mimicking approach for human epileptic seizure detection”. In: *Proc. of the International Biosignal Processing Conference*. 2010, pp. 1–4.

[22] Song Cui et al. “Learning EEG synchronization patterns for epileptic seizure prediction using bag-of-wave features”. In: *Journal of Ambient Intelligence and Humanized Computing* (2018), pp. 1–16.

[23] Levin Kuhlmann et al. “Seizure prediction—ready for a new era”. In: *Nature Reviews Neurology* 14.10 (2018), pp. 618–630.

[24] Mojtaba Bandarabadi et al. “On the proper selection of preictal period for seizure prediction”. In: *Epilepsy & Behavior* 46 (2015), pp. 158–166.

[25] Jason S Naftulin et al. “Ictal and preictal power changes outside of the seizure focus correlate with seizure generalization”. In: *Epilepsia* 59.7 (2018), pp. 1398–1409.

[26] Michael H Kohrman. “What is epilepsy? Clinical perspectives in the diagnosis and treatment”. In: *Journal of Clinical Neurophysiology* 24.2 (2007), pp. 87–95.

[27] HM Hamer et al. “Symptomatology of epileptic seizures in the first three years of life”. In: *Epilepsia* 40.7 (1999), pp. 837–844.

[28] Robert S Fisher et al. “Operational classification of seizure types by the International League Against Epilepsy: Position Paper of the ILAE Commission for Classification and Terminology”. In: *Epilepsia* 58.4 (2017), pp. 522–530.

[29] Juliana Meneguello, Fernando Danelon Leonhardt, and Liliane Desgualdo Pereira. “Auditory processing in patients with temporal lobe epilepsy”. In: *Brazilian journal of otorhinolaryngology* 72.4 (2006), pp. 496–504.

[30] S Sveinbjornsdottir and JS Duncan. “Parietal and occipital lobe epilepsy: a review”. In: *Epilepsia* 34.3 (1993), pp. 493–521.

[31] N Sulaiman et al. “Offline LabVIEW-Based EEG Signals Analysis to Detect Vehicle Driver Microsleep”. In: *International Conference on Movement, Health and Exercise*. Springer, Singapore. 2019, pp. 271–289.

[32] Sandipan Pati and Andreas V Alexopoulos. “Pharmacoresistant epilepsy: from pathogenesis to current and emerging therapies”. In: *Cleve Clin J Med* 77.7 (2010), pp. 457–567.

[33] U Rajendra Acharya et al. “Characterization of focal EEG signals: a review”. In: *Future Generation Computer Systems* 91 (2019), pp. 290–299.

[34] Rei Enatsu and Nobuhiro Mikuni. “Invasive evaluations for epilepsy surgery: a review of the literature”. In: *Neurologia medico-chirurgica* 56.5 (2016), pp. 221–227.

[35] Bernhard Graimann et al. “A comparison between using ECoG and EEG for direct brain communication”. In: *Proceedings of the EMBEC05* (2005).

[36] KJ Friston et al. “Functional connectivity: the principal-component analysis of large (PET) data sets”. In: *Journal of Cerebral Blood Flow & Metabolism* 13.1 (1993), pp. 5–14.

[37] Mark Richardson. “Current themes in neuroimaging of epilepsy: brain networks, dynamic phenomena, and clinical relevance”. In: *Clinical Neurophysiology* 121.8 (2010), pp. 1153–1175.

[38] Weiyu Huang et al. “A graph signal processing perspective on functional brain imaging”. In: *Proceedings of the IEEE* 106.5 (2018), pp. 868–885.

[39] Weiyu Huang, Antonio G Marques, and Alejandro R Ribeiro. “Rating prediction via graph signal processing”. In: *IEEE Transactions on Signal Processing* 66.19 (2018), pp. 5066–5081.

[40] Elisabeth Drayer and Tirza Routtenberg. “Detection of false data injection attacks in smart grids based on graph signal processing”. In: *IEEE Systems Journal* 14.2 (2019), pp. 1886–1896.

[41] Raksha Ramakrishna and Anna Scaglione. “Grid-graph signal processing (grid-GSP): A graph signal processing framework for the power grid”. In: *IEEE Transactions on Signal Processing* 69 (2021), pp. 2725–2739.

[42] Olaf Sporns and Richard F Betzel. “Modular brain networks”. In: *Annual review of psychology* 67 (2016), pp. 613–640.

[43] Hermann Haken. *Principles of brain functioning: a synergetic approach to brain activity, behavior and cognition*. Vol. 67. Springer Science & Business Media, 2013.

[44] Michael D Fox and Marcus E Raichle. “Spontaneous fluctuations in brain activity observed with functional magnetic resonance imaging”. In: *Nature reviews neuroscience* 8.9 (2007), pp. 700–711.

[45] Chenhui Hu et al. “Matched signal detection on graphs: Theory and application to brain imaging data classification”. In: *NeuroImage* 125 (2016), pp. 587–600.

[46] Zarina Rakhimberdina, Xin Liu, and Tsuyoshi Murata. “Population graph-based multi-model ensemble method for diagnosing autism spectrum disorder”. In: *Sensors* 20.21 (2020), p. 6001.

[47] Weiyu Huang et al. “Graph frequency analysis of brain signals”. In: *IEEE journal of selected topics in signal processing* 10.7 (2016), pp. 1189–1203.

[48] Thomas Philip Runarsson and Sven Sigurdsson. “On-line detection of patient specific neonatal seizures using support vector machines and half-wave attribute histograms”. In: *International Conference on Computational Intelligence for Modelling, Control and Automation and International Conference on Intelligent Agents, Web Technologies and Internet Commerce (CIMCA-IAWTIC'06)*. Vol. 2. IEEE. 2005, pp. 673–677.

[49] E Tessy, PP Muhammed Shanir, and Shaleena Manafuddin. “Time domain analysis of epileptic EEG for seizure detection”. In: *2016 International Conference on Next Generation Intelligent Systems (ICNGIS)*. IEEE. 2016, pp. 1–4.

[50] Lucas Lacasa et al. “From time series to complex networks: The visibility graph”. In: *Proceedings of the National Academy of Sciences* 105.13 (2008), pp. 4972–4975.

[51] Zeynab Mohammadpoory, Mahda Nasrolahzadeh, and Javad Haddadnia. “Epileptic seizure detection in EEGs signals based on the weighted visibility graph entropy”. In: *Seizure* 50 (2017), pp. 202–208.

[52] Supriya Supriya et al. “Weighted visibility graph with complex network features in the detection of epilepsy”. In: *IEEE access* 4 (2016), pp. 6554–6566.

[53] Priyanka Mathur and Vijay Kumar Chakka. “Graph Signal Processing of EEG signals for Detection of Epilepsy”. In: *2020 7th International Conference on Signal Processing and Integrated Networks (SPIN)*. IEEE. 2020, pp. 839–843.

[54] Yannick Roy et al. “Deep learning-based electroencephalography analysis: a systematic review”. In: *Journal of neural engineering* 16.5 (2019), p. 051001.

[55] Pari Jahankhani, Vassilis Kodogiannis, and Kenneth Revett. “EEG signal classification using wavelet feature extraction and neural networks”. In: *IEEE John Vincent Atanasoff 2006 International Symposium on Modern Computing (JVA'06)*. IEEE. 2006, pp. 120–124.

[56] Abdulhamit Subasi. “EEG signal classification using wavelet feature extraction and a mixture of expert model”. In: *Expert Systems with Applications* 32.4 (2007), pp. 1084–1093.

[57] Nasser Sadati, Hamid Reza Mohseni, and Arash Maghsoudi. “Epileptic seizure detection using neural fuzzy networks”. In: *2006 IEEE international conference on fuzzy systems*. IEEE. 2006, pp. 596–600.

[58] Jean Gotman. “Automatic recognition of epileptic seizures in the EEG”. In: *Electroencephalography and clinical Neurophysiology* 54.5 (1982), pp. 530–540.

[59] J Gotman. “Seizure recognition and analysis.” In: *Electroencephalography and clinical neurophysiology. Supplement* 37 (1985), pp. 133–145.

[60] Jean Gotman. “Automatic seizure detection: improvements and evaluation”. In: *Electroencephalography and clinical Neurophysiology* 76.4 (1990), pp. 317–324.

[61] PP Shanir, Yusuf U Khan, and Omar Farooq. “Time domain analysis of EEG for automatic seizure detection”. In: *Emerging Trends in Electrical and Electronics Engineering* (2015).

[62] Borbála Hunyadi et al. “Incorporating structural information from the multichannel EEG improves patient-specific seizure detection”. In: *Clinical Neurophysiology* 123.12 (2012), pp. 2352–2361.

[63] Jerald Yoo et al. “An 8-channel scalable EEG acquisition SoC with patient-specific seizure classification and recording processor”. In: *IEEE journal of solid-state circuits* 48.1 (2012), pp. 214–228.

[64] Christos Chatzichristos et al. “Epileptic seizure detection in EEG via fusion of multiview attention-gated U-net deep neural networks”. In: *2020 IEEE Signal Processing in Medicine and Biology Symposium (SPMB)*. IEEE. 2020, pp. 1–7.

[65] Olaf Ronneberger, Philipp Fischer, and Thomas Brox. “U-net: Convolutional networks for biomedical image segmentation”. In: *International Conference on Medical image computing and computer-assisted intervention*. Springer. 2015, pp. 234–241.

[66] Ian C Covert et al. “Temporal graph convolutional networks for automatic seizure detection”. In: *Machine Learning for Healthcare Conference*. PMLR. 2019, pp. 160–180.

[67] André M Bastos and Jan-Mathijs Schoffelen. “A tutorial review of functional connectivity analysis methods and their interpretational pitfalls”. In: *Frontiers in systems neuroscience* 9 (2016), p. 175.

[68] Puneet Rana et al. “Seizure detection using the phase-slope index and multichannel ECoG”. In: *IEEE Transactions on Biomedical Engineering* 59.4 (2012), pp. 1125–1134.

[69] Stefan Haufe et al. “A critical assessment of connectivity measures for EEG data: a simulation study”. In: *Neuroimage* 64 (2013), pp. 120–133.

[70] Guido Nolte et al. “Identifying true brain interaction from EEG data using the imaginary part of coherency”. In: *Clinical neurophysiology* 115.10 (2004), pp. 2292–2307.

[71] M Lavanga et al. “A brain-age model for preterm infants based on functional connectivity”. In: *Physiological measurement* 39.4 (2018), p. 044006.

[72] Mark A Kramer et al. “Network inference with confidence from multivariate time series”. In: *Physical Review E* 79.6 (2009), p. 061916.

[73] Mark A Kramer, Eric D Kolaczyk, and Heidi E Kirsch. “Emergent network topology at seizure onset in humans”. In: *Epilepsy research* 79.2-3 (2008), pp. 173–186.

[74] Hao Qu and Jean Gotman. “Improvement in seizure detection performance by automatic adaptation to the EEG of each patient”. In: *Electroencephalography and clinical Neurophysiology* 86.2 (1993), pp. 79–87.

[75] Iyad Obeid and Joseph Picone. “The temple university hospital EEG data corpus”. In: *Frontiers in neuroscience* 10 (2016), p. 196.

[76] L Veloso et al. “Big data resources for EEGs: enabling deep learning research”. In: *2017 IEEE Signal Processing in Medicine and Biology Symposium (SPMB)*. IEEE. 2017, pp. 1–3.

[77] Domenic Ochal et al. “The Temple University Hospital EEG Corpus: Annotation Guidelines”. In: *Institute for Signal and Information Processing Report* 1.1 (2020).

[78] Silvia Lopez et al. “An analysis of two common reference points for EEGs”. In: *2016 IEEE Signal Processing in Medicine and Biology Symposium (SPMB)*. IEEE. 2016, pp. 1–5.

[79] E. Isufi, A. S. U. Mahabir, and G. Leus. “Blind Graph Topology Change Detection”. In: *IEEE Signal Processing Letters* 25.5 (2018), pp. 655–659. DOI: 10.1109/LSP.2018.2819127.

[80] Kaat Vandecasteele et al. “Visual seizure annotation and automated seizure detection using behind-the-ear electroencephalographic channels”. In: *Epilepsia* 61.4 (2020), pp. 766–775.

[81] Georgiy R Minasyan et al. “Patient-specific early seizure detection from scalp EEG”. In: *Journal of clinical neurophysiology: official publication of the American Electroencephalographic Society* 27.3 (2010), p. 163.

[82] Christoph Baumgartner and Johannes P Koren. “Seizure detection using scalp-EEG”. In: *Epilepsia* 59 (2018), pp. 14–22.

[83] James P Egan and James Pendleton Egan. *Signal detection theory and ROC-analysis*. Academic press, 1975.

[84] Tom Fawcett. “An introduction to ROC analysis”. In: *Pattern recognition letters* 27.8 (2006), pp. 861–874.

A

Patient analysis

A

PATIENT 258 - FNSZ

Recording 1:

Five seizures considered. At first the patient is awake, then he enters a state of drowsiness. We observe different ictal patterns, each characterized by specific dominant frequency bands. However, all seizures are localized in the right centrotemporal lobe.

Recording 2:

Increasing beta activity (above 13Hz) in left hemisphere. 3 considered seizures, all localized in right hemisphere. Status epilepticus.

Figure A.1 depicts in a) and c) the inferred preictal and ictal graphs which are associated with the highest AUC value for fold 1. In b) and d) the figure provide the corresponding degree matrices.

Common observations between folds:

- Preictal graph shows more edges than the ictal one.
- As K increases, we observe less and less connections (in both graphs) in the right hemisphere with a temporal posterior localization.
- Ictal condition more band-limited but still there is not a clear difference.
- Algorithm does not seem robust. Some curves show an inverse polarity.
- In general, a selection of the frequencies benefits the performance of the algorithm.
- Different graphs give comparable performance. This is the case of the complete, preictal and ictal graph.

General comments:

The algorithm does not seem robust for this patient. Different combinations of hyperparameters give different curves with different polarities on the testing set. Selecting the frequency and inferring the graph from data seem to benefit the performance of the detection when compared with the first two baselines. In particular, the ictal graph seems to slightly enhance the performance with respect to the preictal graph. However, the single channel analysis outperforms the other considered ones. In particular, analysis at electrode T4 gives AUC above 0.8. This electrode is in the right temporal region.

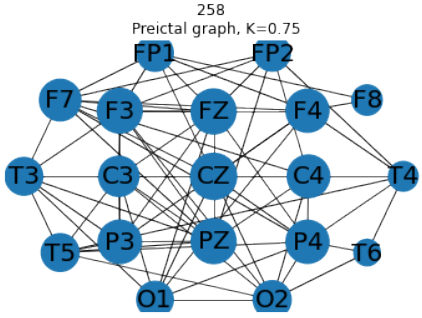

(a)

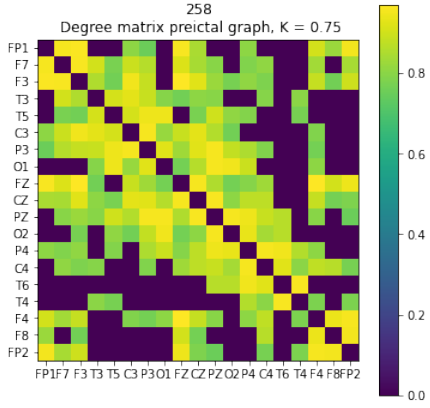

(b)

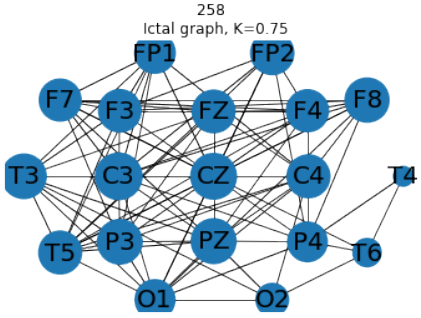

(c)

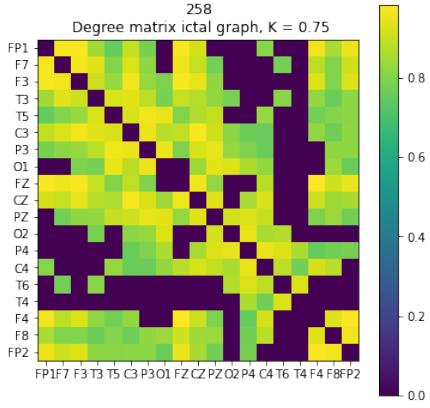

(d)

Figure A.1: An illustration of the inferred a) preictal and b) ictal graphs. The structure refers to fold 1 and hyperparameters providing the highest AUC values. The positions of the nodes resemble their relative position in Figure 4.4. In addition, the width of the circle surrounding each node is an indication of its degree. In b) and d) their associated degree matrix.

A

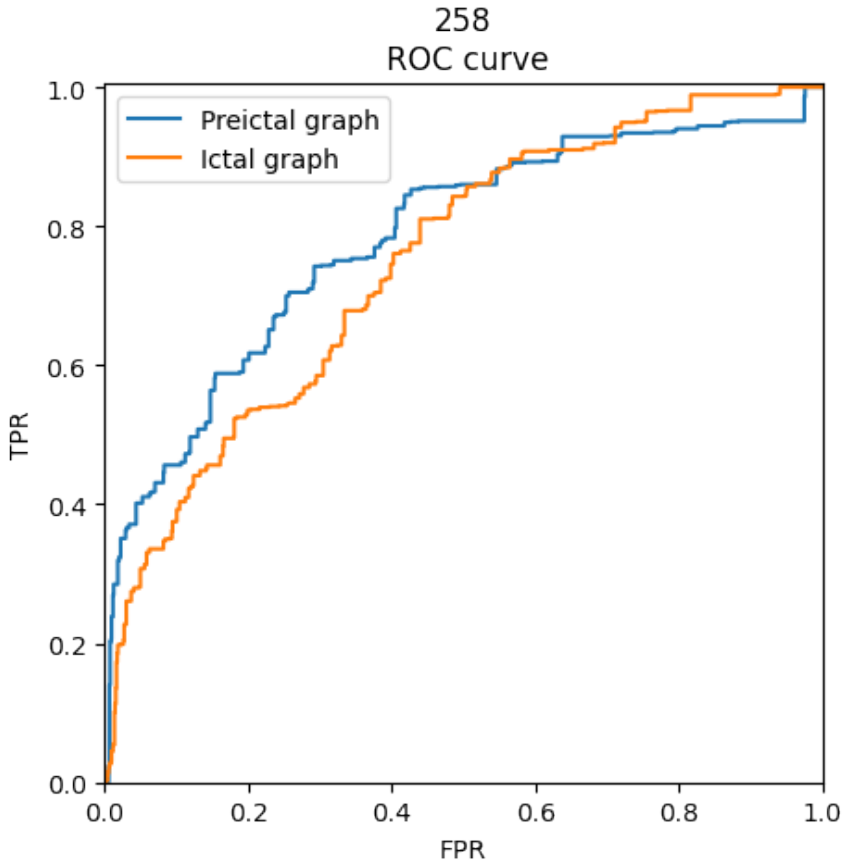

Figure A.2: ROC curve for patient 258 with the proposed method, using preictal graph a) and ictal one b). The curves reported here give the highest AUC value for fold 1. In particular for the preictal graph we used $K = 0.75$ and $p = 0.8$; for the ictal graph we used $K = 0.75$ and $p = 0.85$.

PATIENT 473 - FNSZ

Recording 1:

Fourteen seizures considered. Activity from the right hemisphere is low voltage theta, delta, and muscle activity. From the left hemisphere, the activity is slower delta activity with an underlying sharp wave or periodic complex, which is maximum in the left central parietal region, as well as the posterior temporal region.

Figure A.3 depicts in a) and c) the inferred preictal and ictal graphs which are associated with the highest AUC value for fold 1. In b) and d) the figure provide the corresponding degree matrices.

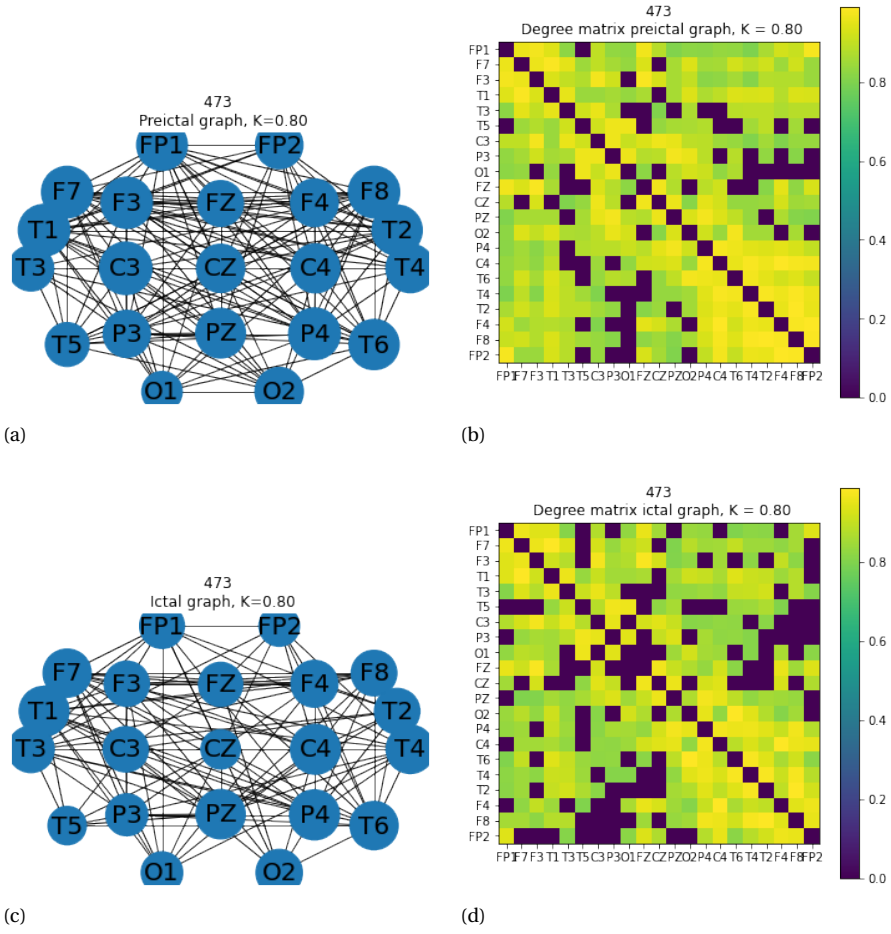

Figure A.3: An illustration of the inferred a) preictal and b) ictal graphs. The structure refers to fold 1 and hyperparameters providing the highest AUC values. The positions of the nodes resemble their relative position in Figure 4.4. In addition, the width of the circle surrounding each node is an indication of its degree. In b) and d) their associated degree matrix.

Common observations between folds:

- In two out of the three folds, the preictal graph shows more edges than the ictal one.
- There is not a clear area where the connections are way less compared with other areas except for in the ictal graph, for K = 0.9. in this case, we observe an area in the left posterior region with few connections.
- Ictal condition more band-limited but still there is not a clear difference.
- Algorithm does not seem robust and, in many cases, it cannot be applied for this patient.
- In general, there does not seem to be general pattern between the curves.

General comments:
The algorithm does not seem robust for this patient. In general, a selection of the frequencies does not benefit the performance of the algorithm: the performance of the proposed method and the one of the detector not selecting frequencies is comparable. In addition, the complete graph in this case gives significant results too. The same holds for the ictal graph. Single electrode analysis gives best results for electrodes located at the right and frontal areas. Performance for this patient is generally good.
Figure **??** depicts the ROC curves giving highest AUC values for the first fold of the simulations, using the preictal and the ictal graph. Then, Table **??** reports the corresponding TPR values for FPR=10^{-3} and FPR=$2 * 10^{-3}$.

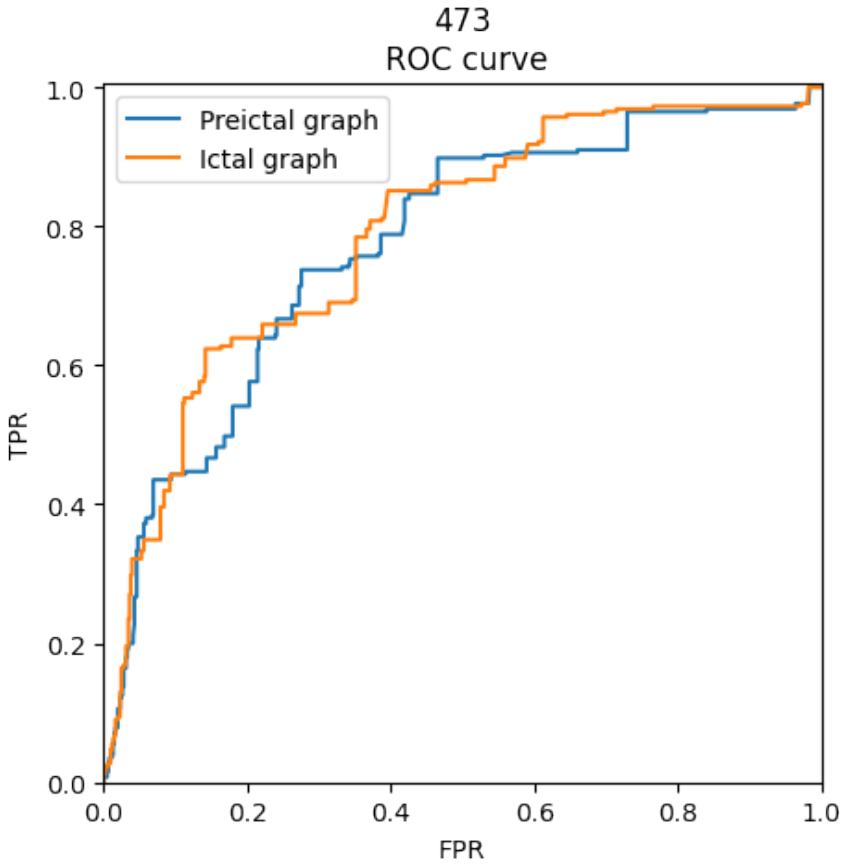

Figure A.4: ROC curve for patient 473 with the proposed method, using preictal graph a) and ictal one b). The curves reported here give the highest AUC value for fold 1. In particular for the preictal graph we used $K = 0.8$ and $p = 0.7$; for the ictal graph we used $K = 0.8$ and $p = 0.85$.

PATIENT 529 - FNSZ

Recording 1:
Periodic left temporal sharp wave identified with a periodicity of approximately 1 to 3 seconds throughout the record. However, no seizure occurs.
Recording 2:
One seizure from the left temporal region. Left temporal periodic sharp waves. A postictal 5.5 Hz rhythmic discharge identified from the occipital regions, left greater than right.
Recording 3:
Left temporal sharp waves. Three left temporal lobe seizures activity and sharp and focal slowing.

Figure A.5 depicts in a) and c) the inferred preictal and ictal graphs which are associated with the highest AUC value for fold 1. In b) and d) the figure provide the corresponding degree matrices.
Common observations between folds:

- Preictal graph shows more edges than the ictal one.
- Less connections are observed in the posterior area with no clear difference between left and right hemispheres.
- Ictal condition more band-limited but still there is not a clear difference.
- Algorithm does not seem robust and, in many cases, it cannot be applied for this patient.

General comments:
The algorithm does not seem robust for this patient. In general, a selection of the frequencies does not benefit the performance of the algorithm. The performance of the proposed method and the one of the detector not selecting frequencies is comparable. However, it seems that a complete graph in this case gives not useful information. Hence the ictal graph (that is less connected) also gives slightly better performances. Single electrode analysis gives best results for electrodes located at the right and frontal areas. Still AUC below 0.8. In general, the performance for this patient is not really satisfying. It might be due to intense pattern of low frequencies.
Figure **??** depicts the ROC curves giving highest AUC values for the first fold of the simulations, using the preictal and the ictal graph. Then, Table **??** reports the corresponding TPR values for FPR=10^{-3} and FPR=$2 * 10^{-3}$.

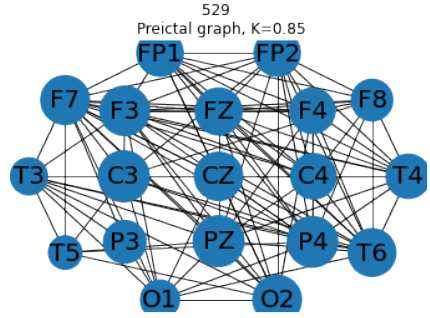

(a)

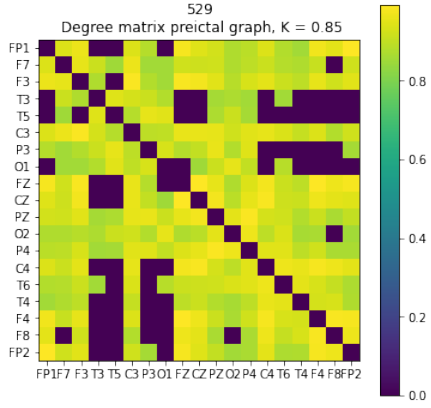

(b)

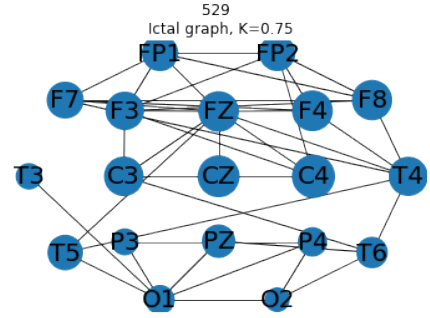

(c)

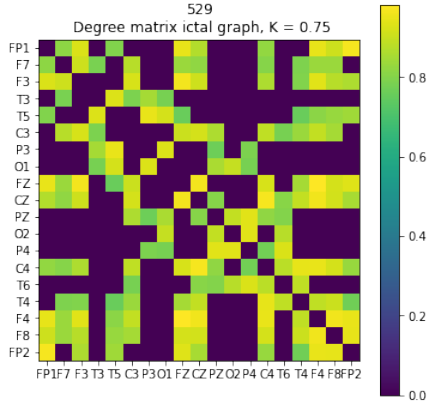

(d)

Figure A.5: An illustration of the inferred a) preictal and b) ictal graphs. The structure refers to fold 1 and hyperparameters providing the highest AUC values. The positions of the nodes resemble their relative position in Figure 4.4. In addition, the width of the circle surrounding each node is an indication of its degree. In b) and d) their associated degree matrix.

A

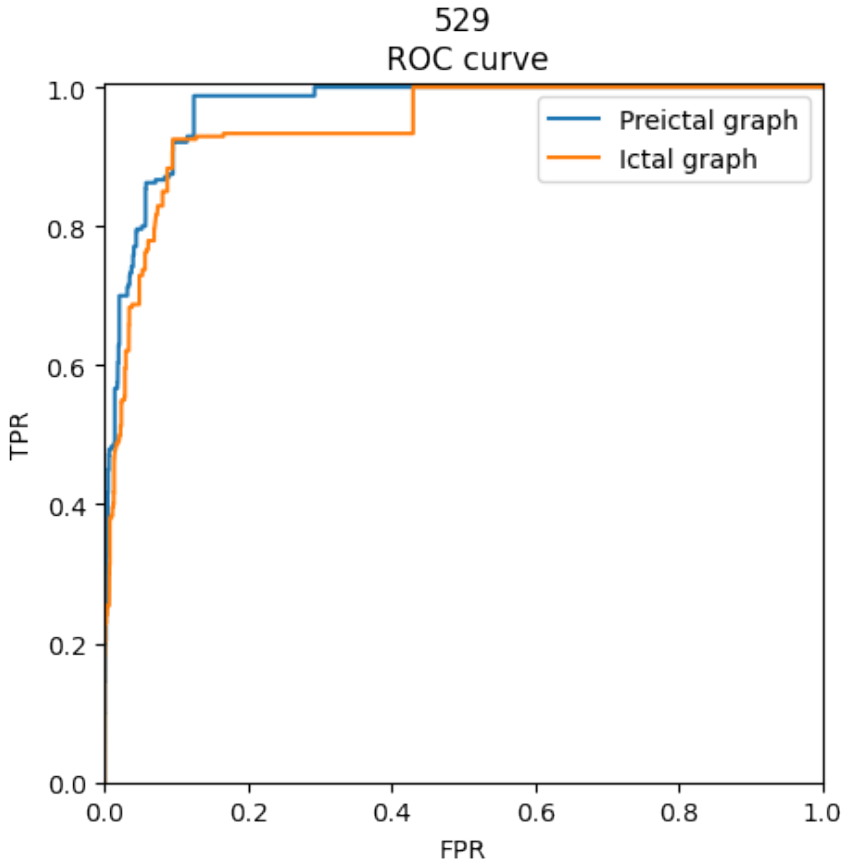

Figure A.6: ROC curve for patient 529 with the proposed method, using preictal graph a) and ictal one b). The curves reported here give the highest AUC value for fold 1. In particular for the preictal graph we used $K = 0.85$ and $p = 0.95$; for the ictal graph we used $K = 0.75$ and $p = 0.95$.

PATIENT 1543 - FNSZ

Recording 1:

Four seizures localized in the left hemisphere, maximum in the temporal region. The individual is in an unconscious state. Status epilepticus.

Figure A.7 depicts in a) and c) the inferred preictal and ictal graphs which are associated with the highest AUC value for fold 1. In b) and d) the figure provide the corresponding degree matrices.

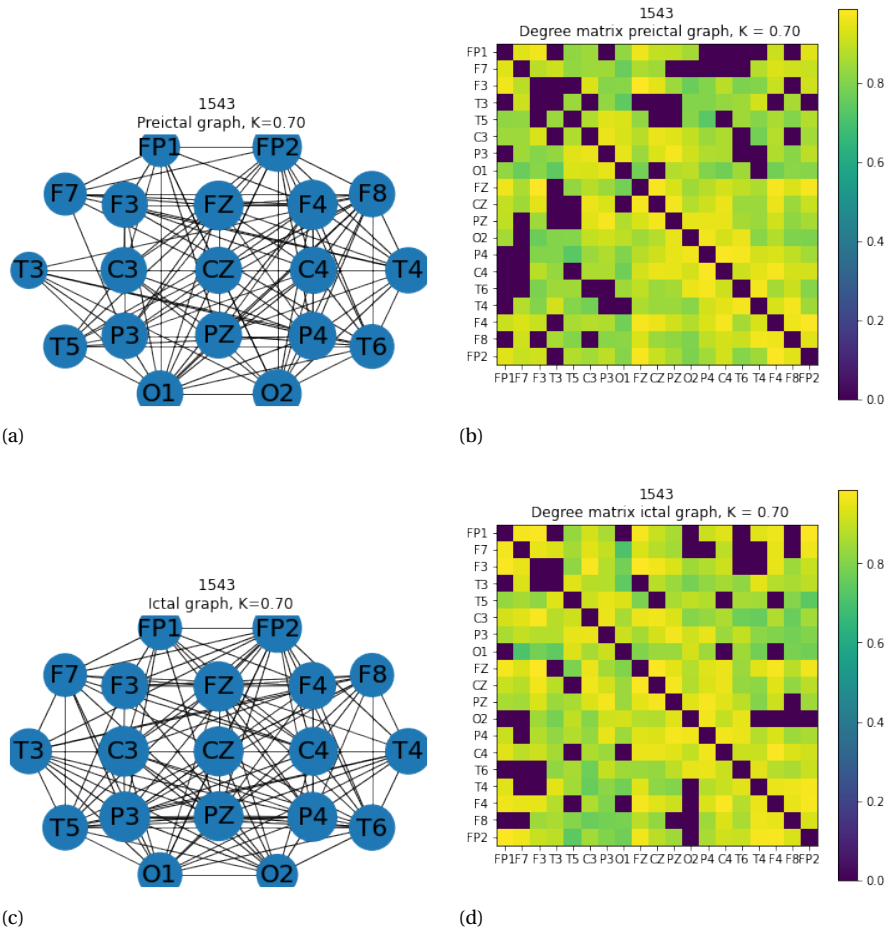

Figure A.7: An illustration of the inferred a) preictal and b) ictal graphs. The structure refers to fold 1 and hyperparameters providing the highest AUC values. The positions of the nodes resemble their relative position in Figure 4.4. In addition, the width of the circle surrounding each node is an indication of its degree. In b) and d) their associated degree matrix.

Common observations between folds:

- Preictal graph shows less edges than the ictal one in fold 2 and 3. The opposite holds for folder 1.
- No clear difference between left and right hemispheres.
- Ictal condition more band-limited but still there is not a clear difference.
- Algorithm does not seem robust and, in many cases, it cannot be applied for this patient.
- For most cases the preictal condition is more bandlimited. However, there is not a clear difference.
- For most of the cases the algorithm does not work as it cannot be applied.
- In general, there does not seem to be general pattern between the curves.

General comments:
In general, a selection of the frequencies slightly benefits the performance of the algorithm. The complete graph does not give useful information. Furthermore the use of the ictal graph gives comparable results with the detector built with the preictal graph. The performance for this patient is not really satisfying.
Figure **??** depicts the ROC curves giving highest AUC values for the first fold of the simulations, using the preictal and the ictal graph. Then, Table **??** reports the corresponding TPR values for FPR=10^{-3} and FPR=$2 * 10^{-3}$.

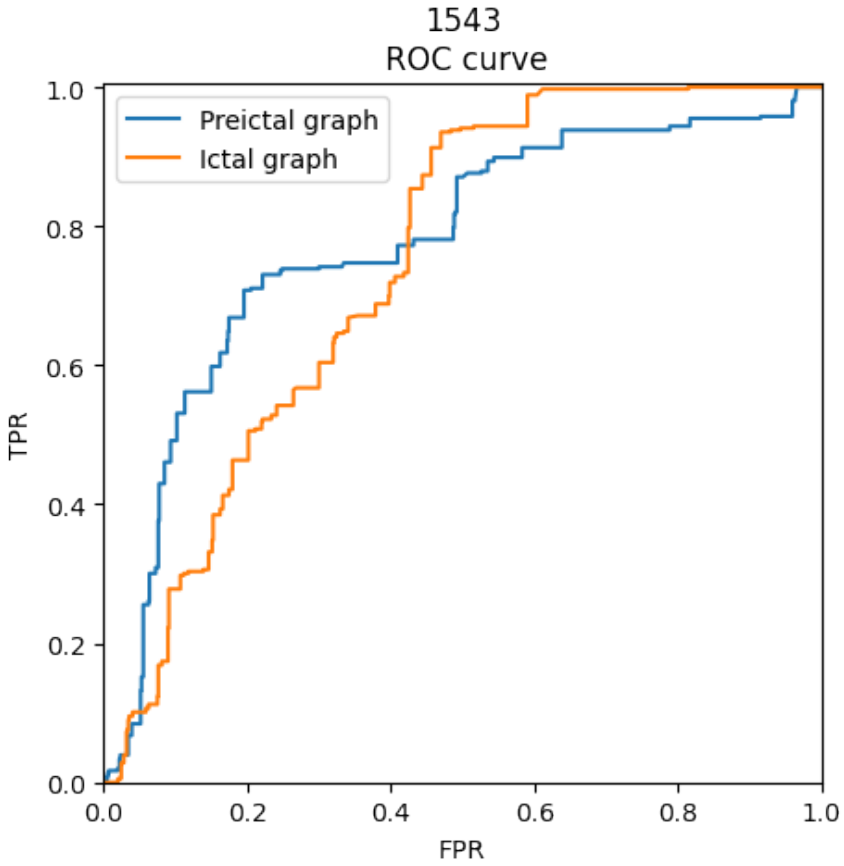

Figure A.8: ROC curve for patient 1543 with the proposed method, using preictal graph a) and ictal one b). The curves reported here give the highest AUC value for fold 1. In particular for the preictal graph we used $K = 0.7$ and $p = 0.7$; for the ictal graph we used $K = 0.7$ and $p = 0.7$.

A

PATIENT 2297 - CPSZ

Recording 1:
No seizure present. However the EEG has abnormal activity due to focal slowing and fast activity from right occipitotemporal region; right centrotemporal sharp waves; asymmetry with faster frequency activity from right.
Recording 2:
Eight seizures from the right but challenging to localize. Muscle movement.

Figure A.9 depicts in a) and c) the inferred preictal and ictal graphs which are associated with the highest AUC value for fold 1. In b) and d) the figure provide the corresponding degree matrices.
Common observations between folds:

- Ictal graph shows less edges than the ictal one in fold 1 and 2. The opposite holds for fold 3.

General comments:
Good performance both from left and right electrodes. The algorithm works very well for this patient. Maybe because it is distinguishing ictal from abnormal activity.
Figure **??** depicts the ROC curves giving highest AUC values for the first fold of the simulations, using the preictal and the ictal graph. Then, Table **??** reports the corresponding TPR values for FPR=10^{-3} and FPR=$2 * 10^{-3}$.

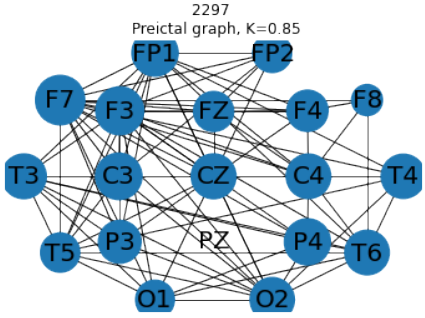

(a)

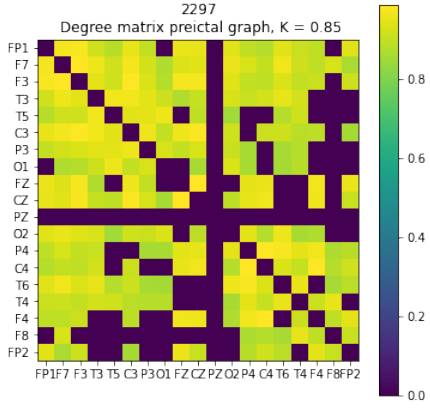

(b)

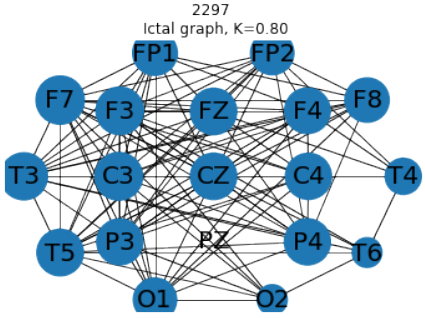

(c)

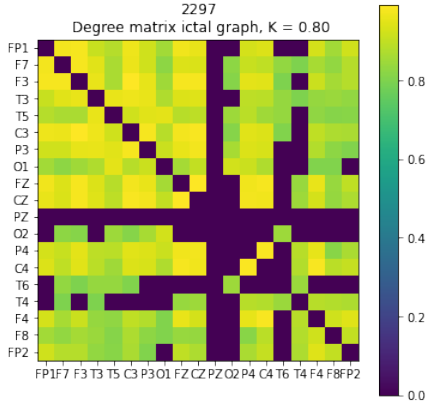

(d)

Figure A.9: An illustration of the inferred a) preictal and b) ictal graphs. The structure refers to fold 1 and hyperparameters providing the highest AUC values. The positions of the nodes resemble their relative position in Figure 4.4. In addition, the width of the circle surrounding each node is an indication of its degree. In b) and d) their associated degree matrix.

A

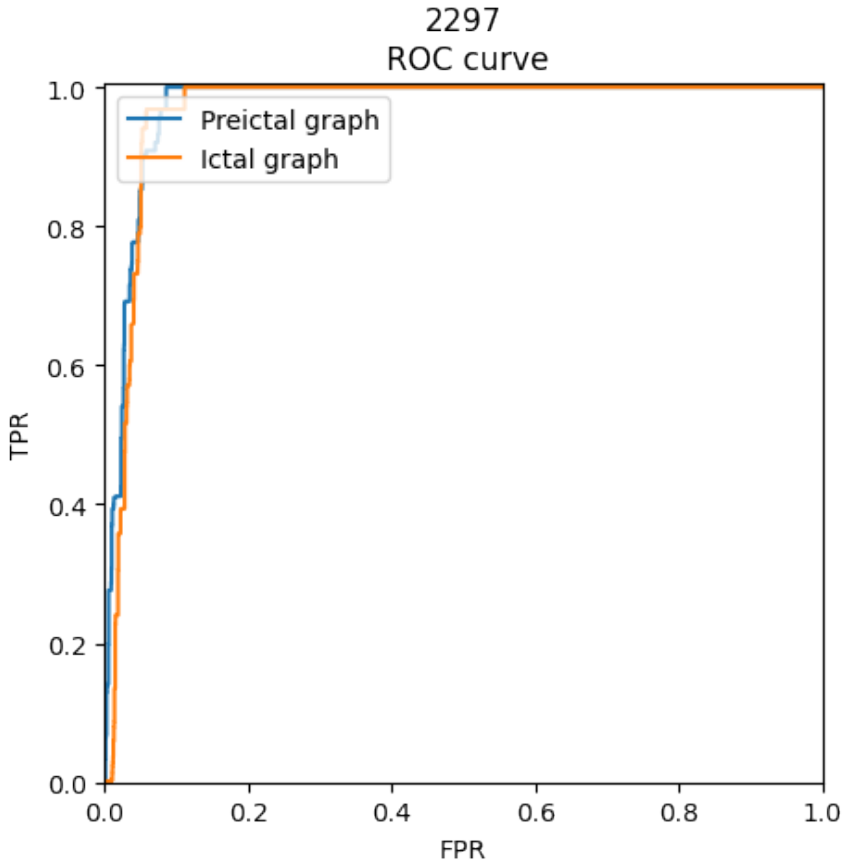

Figure A.10: ROC curve for patient 2297 with the proposed method, using preictal graph a) and ictal one b). The curves reported here give the highest AUC value for fold 1. In particular for the preictal graph we used $K = 0.85$ and $p = 0.85$; for the ictal graph we used $K = 0.8$ and $p = 0.8$.

PATIENT 2806 - FNSZ

Recording 1:

Sixteen seizures with onset in right hemisphere. Involuntary movements left hand and of head. Marked background suppression from left.

Recording 2:

No seizure. Spike wave complexes that originate from the right hemisphere. Background has improved and slowing is observed.

Figure A.11 depicts in a) and c) the inferred preictal and ictal graphs which are associated with the highest AUC value for fold 1. In b) and d) the figure provide the corresponding degree matrices.

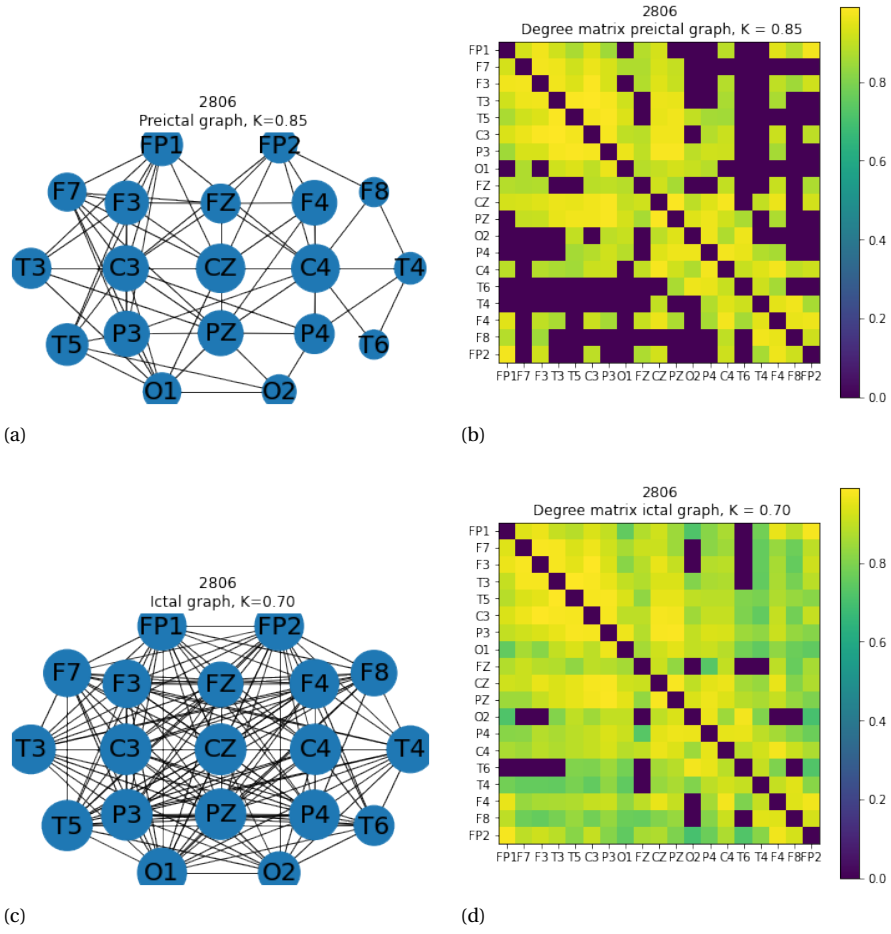

Figure A.11: An illustration of the inferred a) preictal and b) ictal graphs. The structure refers to fold 1 and hyperparameters providing the highest AUC values. The positions of the nodes resemble their relative position in Figure 4.4. In addition, the width of the circle surrounding each node is an indication of its degree. In b) and d) their associated degree matrix.

Common observations between folds:

- Preictal graph shows less connections than the ictal one.
- Right hemisphere has slightly less connections.
- A lot of curves show behaviour almost random.
- A lot of combination of the two hyperparameter are not suitable for the method.
- Ictal condition slightly more band-limited but still there is not a clear difference

General comments:
In general, a selection of the frequencies slightly benefits the performance of the algorithm. The complete graph does not give useful information. Comparable results in terms of AUC with respect to the preictal projection For first two folds, best performing electrode is in left hemisphere (T3). For third record, the electrode with best AUC is located on the frontal area of the right hemisphere (F4). The performance for this patient is not really satisfying. It might be due to suppression of background.
Figure A.12 depicts the ROC curves giving highest AUC values for the first fold of the simulations, using the preictal and the ictal graph. Then, Table **??** reports the corresponding TPR values for FPR=10^{-3} and FPR=$2 * 10^{-3}$.

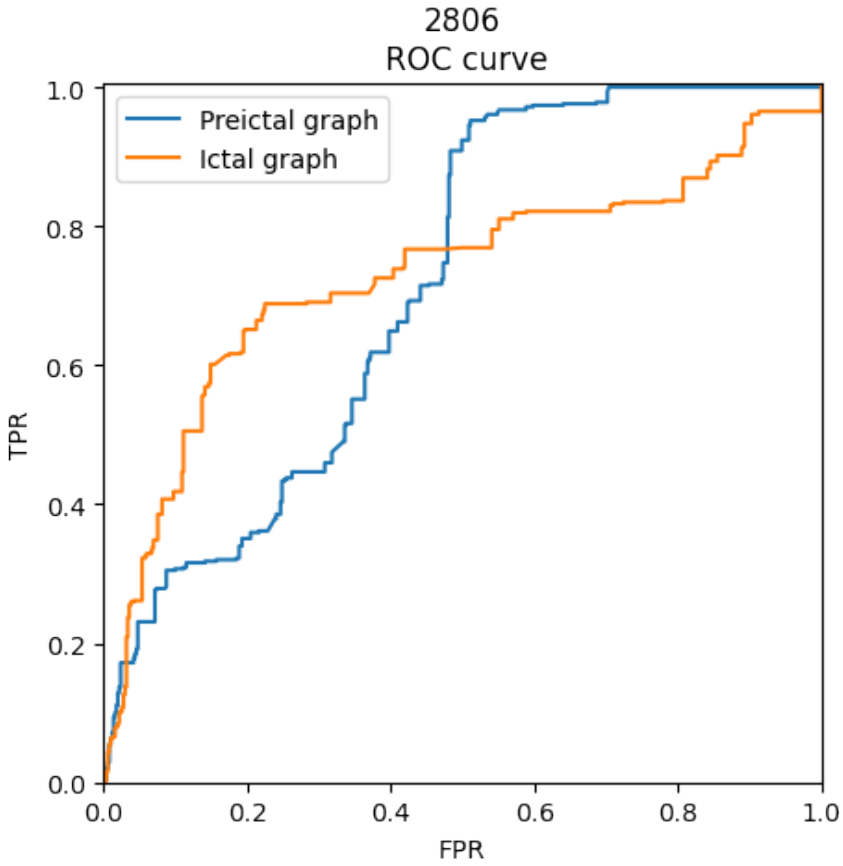

Figure A.12: ROC curve for patient 2806 with the proposed method, using preictal graph a) and ictal one b). The curves reported here give the highest AUC value for fold 1. In particular for the preictal graph we used $K = 0.85$ and $p = 0.85$; for the ictal graph we used $K = 0.7$ and $p = 0.9$.

A

PATIENT 3208 - FNSZ

Recording 1:

Four seizures from right hemisphere. The recording demonstrates gradual diminution, a fading of the epileptiform activity from the right frontal region. The overall background from the left demonstrates some variability with some portions being much slower than the right. Then, the epileptiform fades from the right hemisphere, although the intra-hemispheric asymmetry persists.

Figure A.13 depicts in a) and c) the inferred preictal and ictal graphs which are associated with the highest AUC value for fold 1. In b) and d) the figure provide the corresponding degree matrices.

Common observations between folds:

- Preictal graph shows less connections than the ictal one.
- Right hemisphere has slightly less connections.
- Preictal condition slightly more band-limited. The average spectrum shows differences even though there does not seem to be a true bandlimited condition.
- Some curves show a sort of flat behaviour indicating a strange distribution. Here having a second feature to use might help.

General comments:

In general, a selection of the frequencies benefits the performance of the algorithm. The complete graph does not give further information. We notice an inversion of polarity for the last fold. Ictal has similar results but slightly worse in terms of AUC. For first two folds, best performing electrode is in right hemisphere (C4). For third record, the electrode with best AUC is located at FZ. Average spectrum shows differences even though standard deviation is high. ROC curves show strange polarity, in particular for folds 2 and 3.

Figure A.14 depicts the ROC curves giving highest AUC values for the first fold of the simulations, using the preictal and the ictal graph. Then, Table **??** reports the corresponding TPR values for FPR=10^{-3} and FPR=$2 * 10^{-3}$.

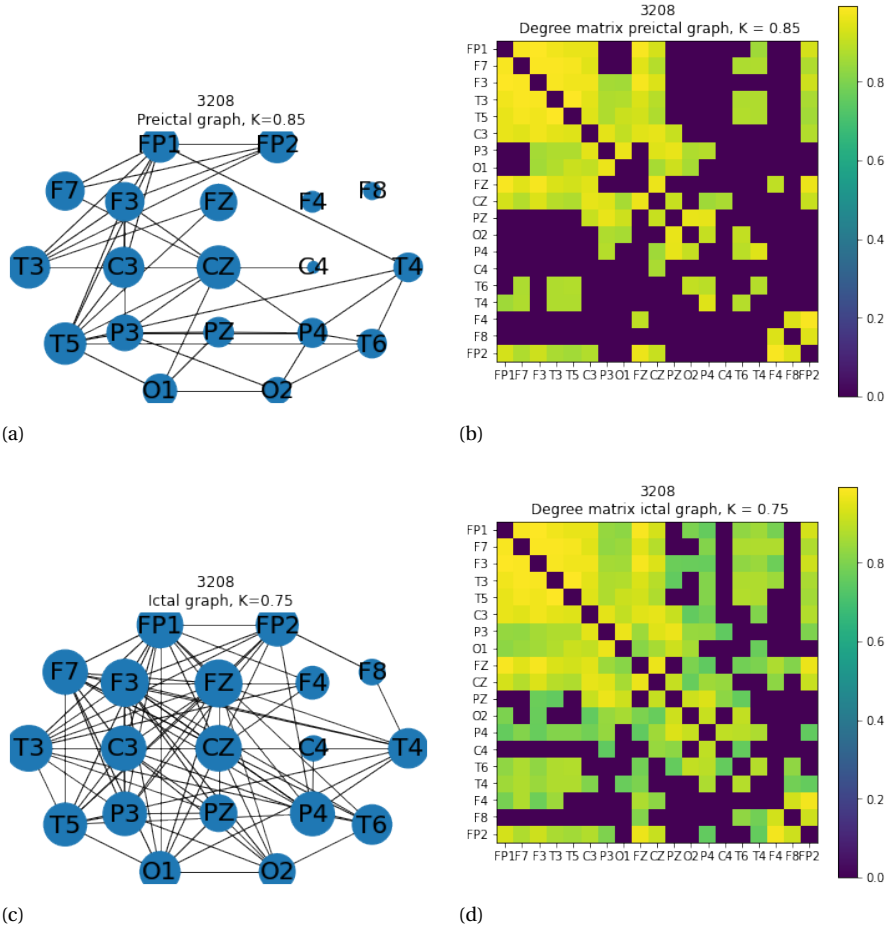

Figure A.13: An illustration of the inferred a) preictal and b) ictal graphs. The structure refers to fold 1 and hyperparameters providing the highest AUC values. The positions of the nodes resemble their relative position in Figure 4.4. In addition, the width of the circle surrounding each node is an indication of its degree. In b) and d) their associated degree matrix.

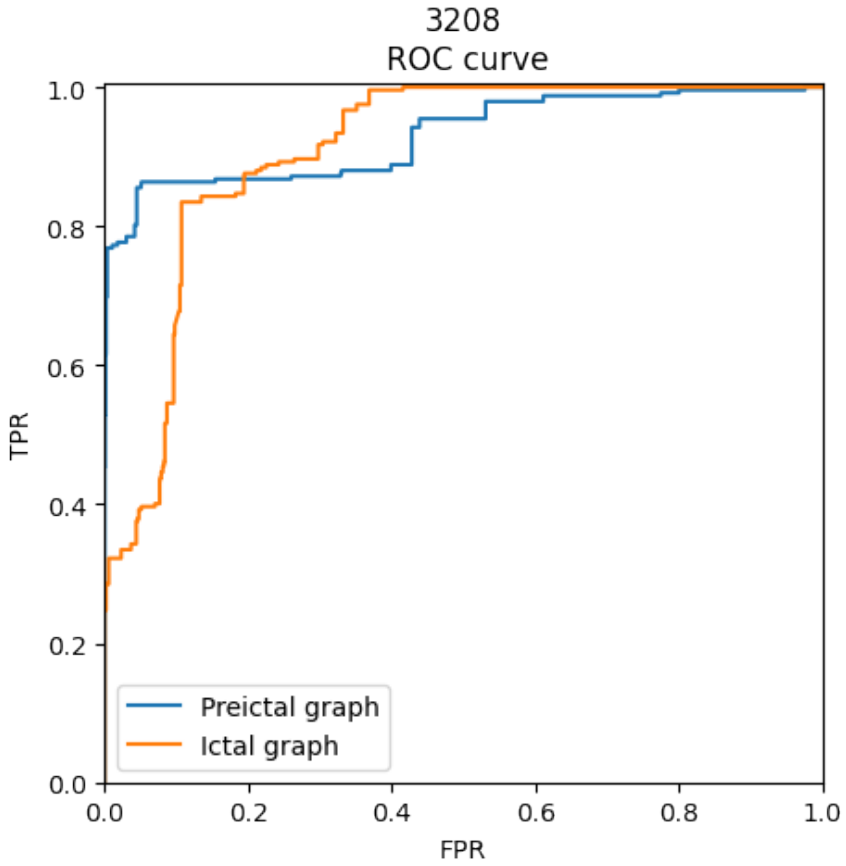

Figure A.14: ROC curve for patient 3208 with the proposed method, using preictal graph a) and ictal one b). The curves reported here give the highest AUC value for fold 1. In particular for the preictal graph we used $K = 0.8$ and $p = 0.7$; for the ictal graph we used $K = 0.75$ and $p = 0.9$.

PATIENT 3636 - FNSZ

Recording 1:

Eight seizures from right hemisphere. Focal onset right hemispheric seizures in an individual who at least initially is conversant during these seizures. They spread also to left hemisphere. In the end the ictal pattern cease abruptly.

Figure A.15 depicts in a) and c) the inferred preictal and ictal graphs which are associated with the highest AUC value for fold 1. In b) and d) the figure provide the corresponding degree matrices.

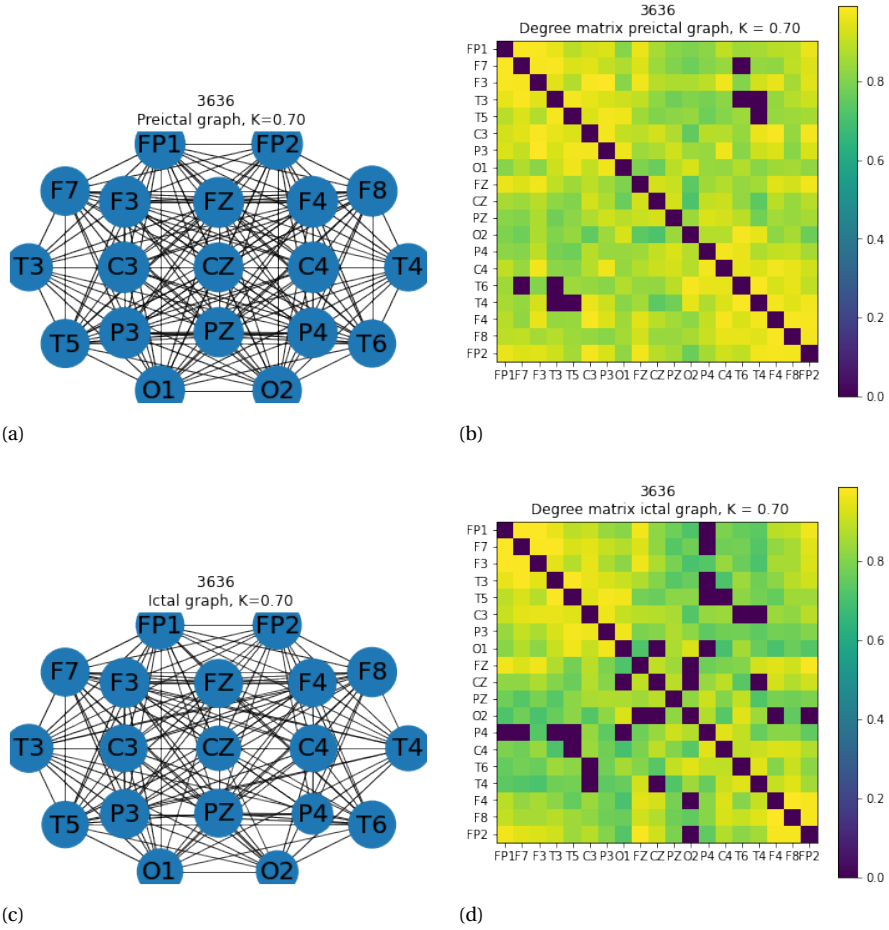

Figure A.15: An illustration of the inferred a) preictal and b) ictal graphs. The structure refers to fold 1 and hyperparameters providing the highest AUC values. The positions of the nodes resemble their relative position in Figure 4.4. In addition, the width of the circle surrounding each node is an indication of its degree. In b) and d) their associated degree matrix.

Common observations between folds:

- Ictal graph shows less connections than the preictal one.
- Right hemisphere has slightly less connections.
- Sometimes (for combination of hyperparameters) the ictal condition is more bandlimited, for others the ictal is. This because there is not a clear difference in terms of bandwidth.
- Sometimes strange shape of curved indicating the need to extract more features.

General comments:
In general, a selection of the frequencies benefits the performance of the algorithm and so does learning the graph and not using a complete one. Comparable results in terms of AUC with respect to the preictal projection. Best performing electrode for all folds in right occipital area. The algorithm seems to perform quite well even with a spread of areas involved in the seizure.
Figure A.16 depicts the ROC curves giving highest AUC values for the first fold of the simulations, using the preictal and the ictal graph. Then, Table **??** reports the corresponding TPR values for FPR=10^{-3} and FPR=$2 * 10^{-3}$.

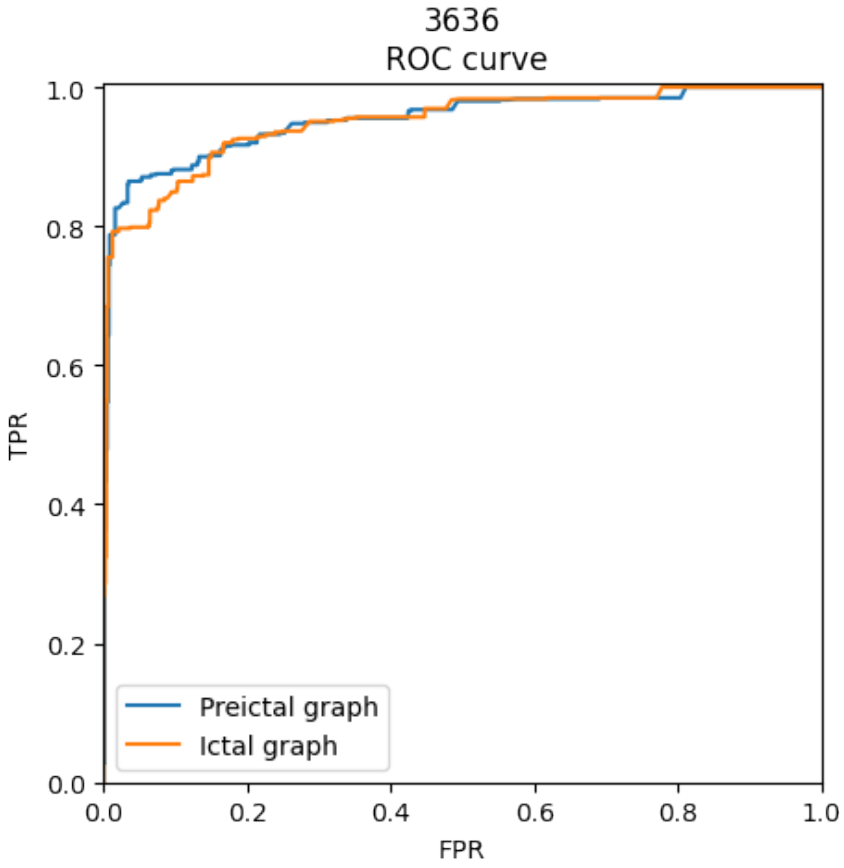

Figure A.16: ROC curve for patient 258 with the proposed method, using preictal graph a) and ictal one b). The curves reported here give the highest AUC value for fold 1. In particular for the preictal graph we used $K = 0.7$ and $p = 0.95$; for the ictal graph we used $K = 0.7$ and $p = 0.95$.

A

PATIENT 3977 - CPSZ

Recording 1:

Five seizures. The accurate localization was somewhat challenging and there were some atypical features such as a high amplitude but positive rather than negative discharge using the referential montage. In that one of the behaviours is eye deviation to the left, consideration for right occipital focus.

Figure A.17 depicts in a) and c) the inferred preictal and ictal graphs which are associated with the highest AUC value for fold 1. In b) and d) the figure provide the corresponding degree matrices.

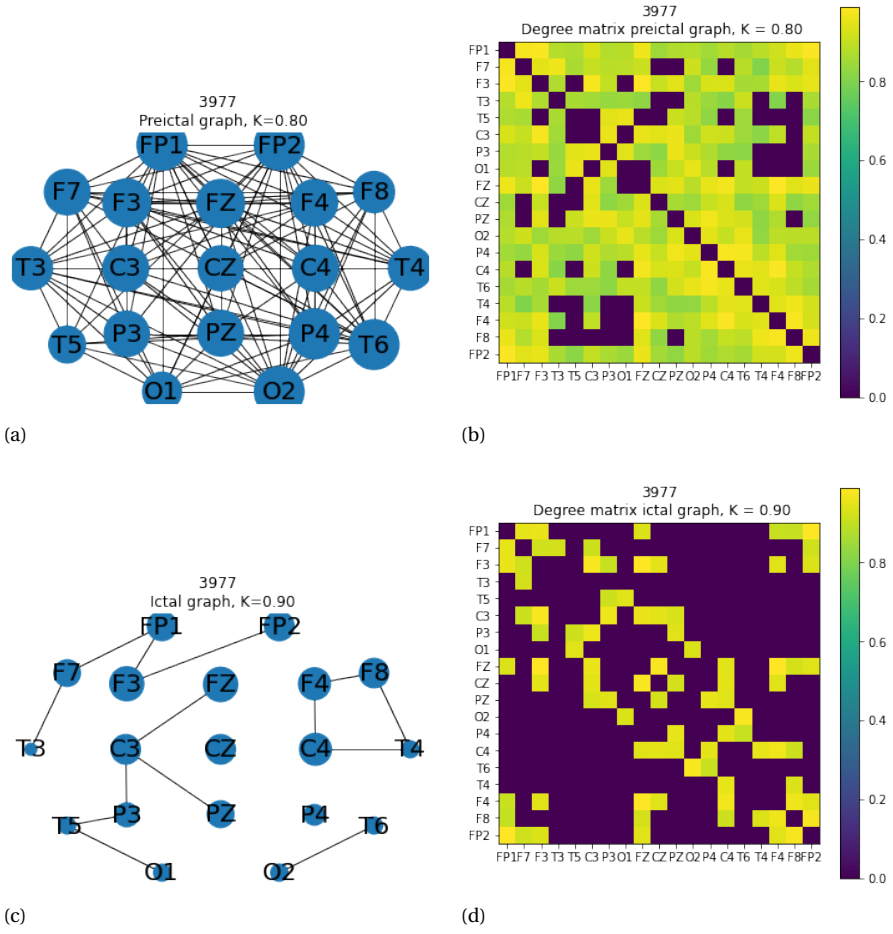

Figure A.17: An illustration of the inferred a) preictal and b) ictal graphs. The structure refers to fold 1 and hyperparameters providing the highest AUC values. The positions of the nodes resemble their relative position in Figure 4.4. In addition, the width of the circle surrounding each node is an indication of its degree. In b) and d) their associated degree matrix.

Common observations between folds:

- Ictal graph shows less connections than the preictal one.
- Occipital area has slightly less connections.
- Ictal slightly more bandlimited. There is not a clear difference in terms of bandwidth. However, for second and third fold, background projection however has little variability.
- Start with strange plateau which is observed also with the ictal graph.
- Not clear pattern between the hyperparameters.

General comments:
In general, a selection of the frequencies benefits the performance of the algorithm and so does learning the graph and not using a complete one. Ictal has worse average performance in terms of AUC. Best performing electrodes are at T6 for first fold, FZ for second and third fold. This does not match the situation portrayed by the annotation. For last two folds there is slight plateau like behaviour at start of recording.
Figure A.18 depicts the ROC curves giving highest AUC values for the first fold of the simulations, using the preictal and the ictal graph. Then, Table **??** reports the corresponding TPR values for FPR=10^{-3} and FPR=$2 * 10^{-3}$.

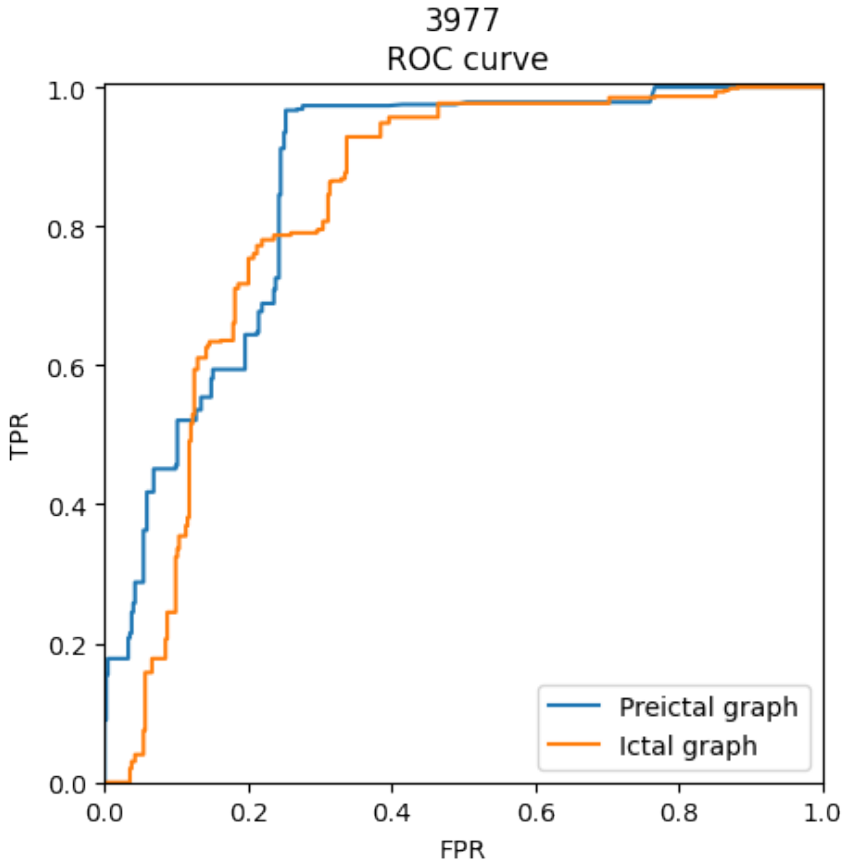

Figure A.18: ROC curve for patient 3977 with the proposed method, using preictal graph a) and ictal one b). The curves reported here give the highest AUC value for fold 1. In particular for the preictal graph we used $K = 0.8$ and $p = 0.95$; for the ictal graph we used $K = 0.9$ and $p = 0.95$.

PATIENT 4434 - FNSZ

Recording 1:

Eight repetitive focal seizures from the left occipital region. Slow activity from right hemisphere.

Figure A.19 depicts in a) and c) the inferred preictal and ictal graphs which are associated with the highest AUC value for fold 1. In b) and d) the figure provide the corresponding degree matrices.

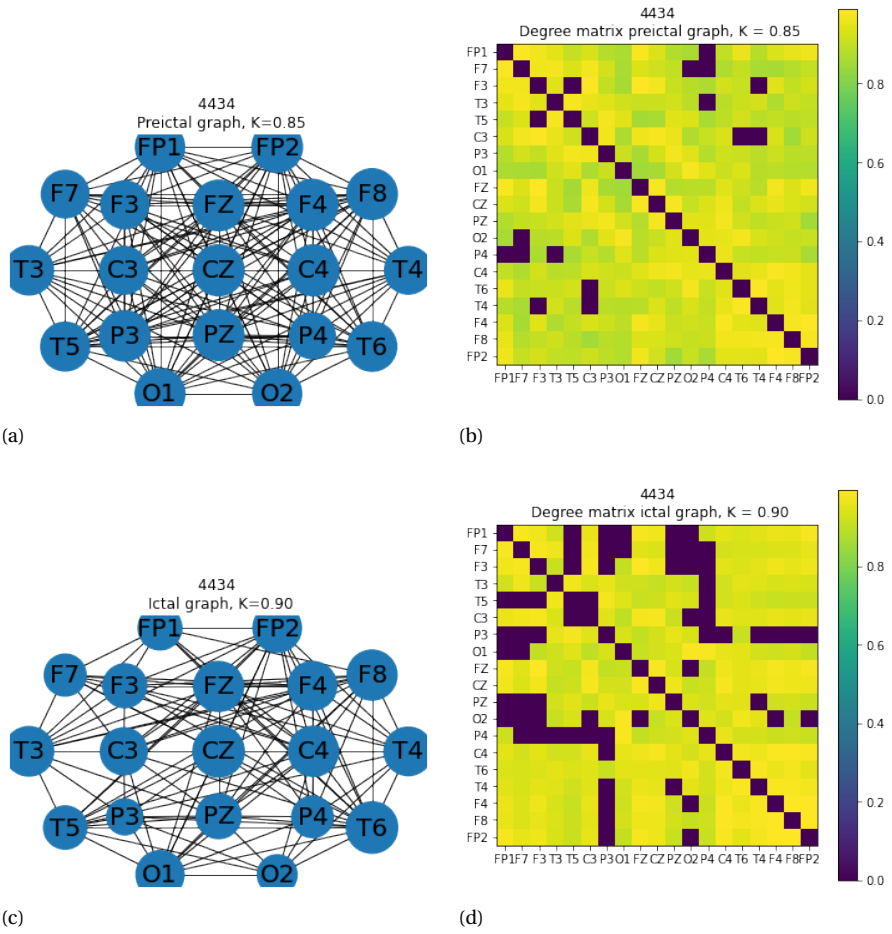

Figure A.19: An illustration of the inferred a) preictal and b) ictal graphs. The structure refers to fold 1 and hyperparameters providing the highest AUC values. The positions of the nodes resemble their relative position in Figure 4.4. In addition, the width of the circle surrounding each node is an indication of its degree. In b) and d) their associated degree matrix.

Common observations between folds:

- Ictal graph shows less connections than the preictal one.
- Right hemisphere has slightly less connections.
- Sometimes (for combination of hyperparameters) the ictal condition is more bandlimited, for others the ictal is. This because there is not a clear difference in terms of bandwidth.
- Sometimes strange shape of curved indicating the need to extract more features.
- No clear pattern between the hyperparameters.

General comments:
Ictal graph allows for comparable results in terms of AUC with respect to the preictal projection. The single channel analysis does not give promising results either.
Figure **??** depicts the ROC curves giving highest AUC values for the first fold of the simulations, using the preictal and the ictal graph. Then, Table **??** reports the corresponding TPR values for FPR=10^{-3} and FPR=$2 * 10^{-3}$.

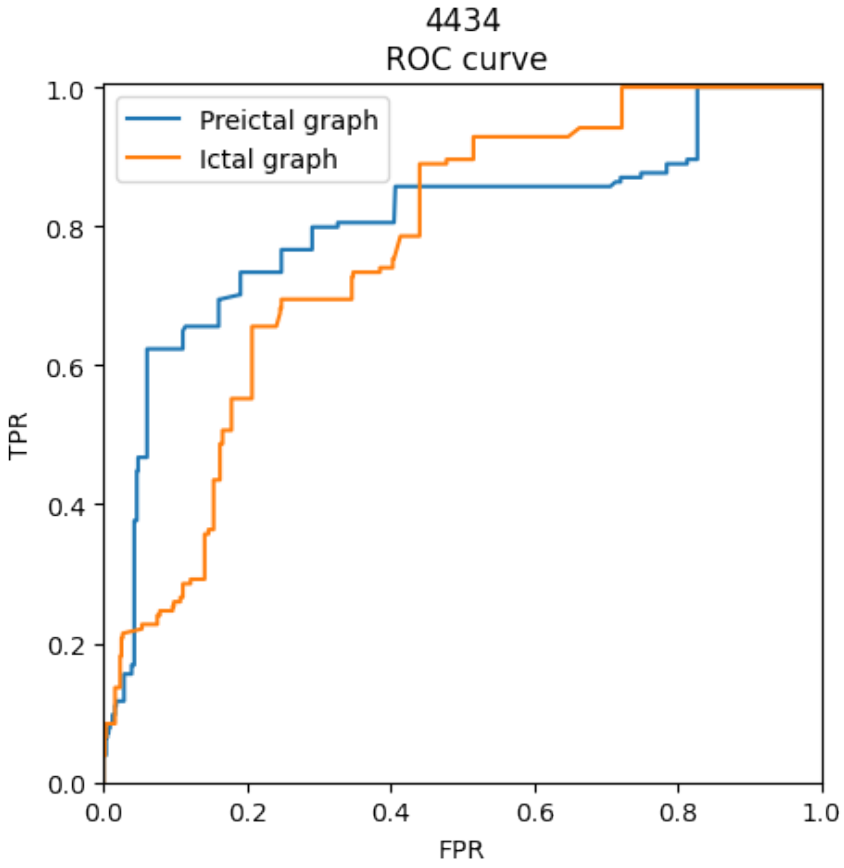

Figure A.20: ROC curve for patient 4434 with the proposed method, using preictal graph a) and ictal one b). The curves reported here give the highest AUC value for fold 1. In particular for the preictal graph we used $K = 0.85$ and $p = 0.9$; for the ictal graph we used $K = 0.9$ and $p = 0.95$.

PATIENT 4473 - FNSZ

Recording 1:
Periodic left temporal sharp wave identified with a periodicity of approximately 1 to 3 seconds throughout the record. However, no seizure occurs.
Recording 2:
One seizure from the left temporal region. Left temporal periodic sharp waves. A postictal 5.5 Hz rhythmic discharge identified from the occipital regions, left greater than right.
Recording 3:
Left temporal sharp waves. Three left temporal lobe seizures activity and sharp and focal slowing.

Figure A.21 depicts in a) and c) the inferred preictal and ictal graphs which are associated with the highest AUC value for fold 1. In b) and d) the figure provide the corresponding degree matrices.
Common observations between folds:

- Preictal graph shows more edges than the ictal one.

General comments:
Figure **??** depicts the ROC curves giving highest AUC values for the first fold of the simulations, using the preictal and the ictal graph. Then, Table **??** reports the corresponding TPR values for FPR=10^{-3} and FPR=$2 * 10^{-3}$.

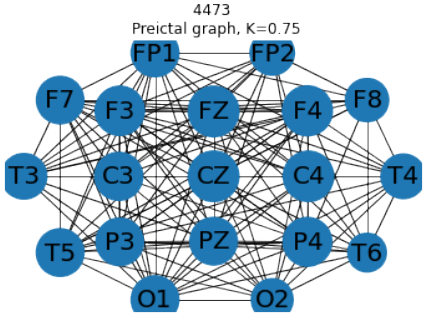

(a)

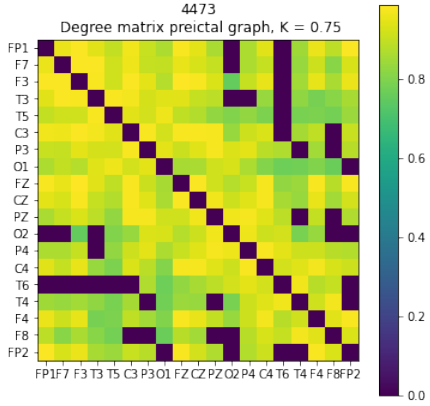

(b)

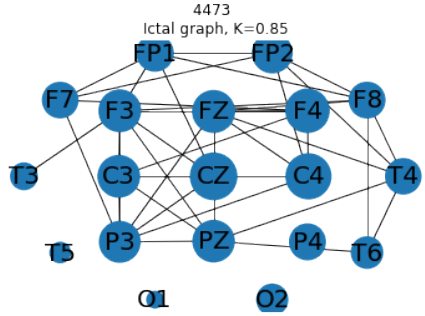

(c)

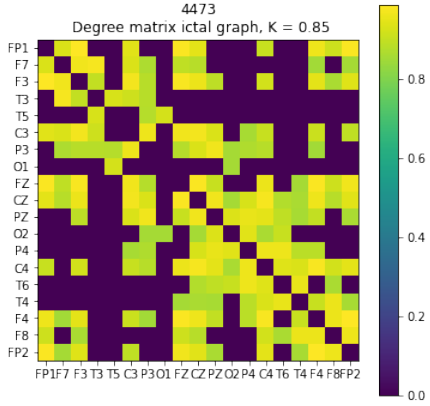

(d)

Figure A.21: An illustration of the inferred a) preictal and b) ictal graphs. The structure refers to fold 1 and hyperparameters providing the highest AUC values. The positions of the nodes resemble their relative position in Figure 4.4. In addition, the width of the circle surrounding each node is an indication of its degree. In b) and d) their associated degree matrix.

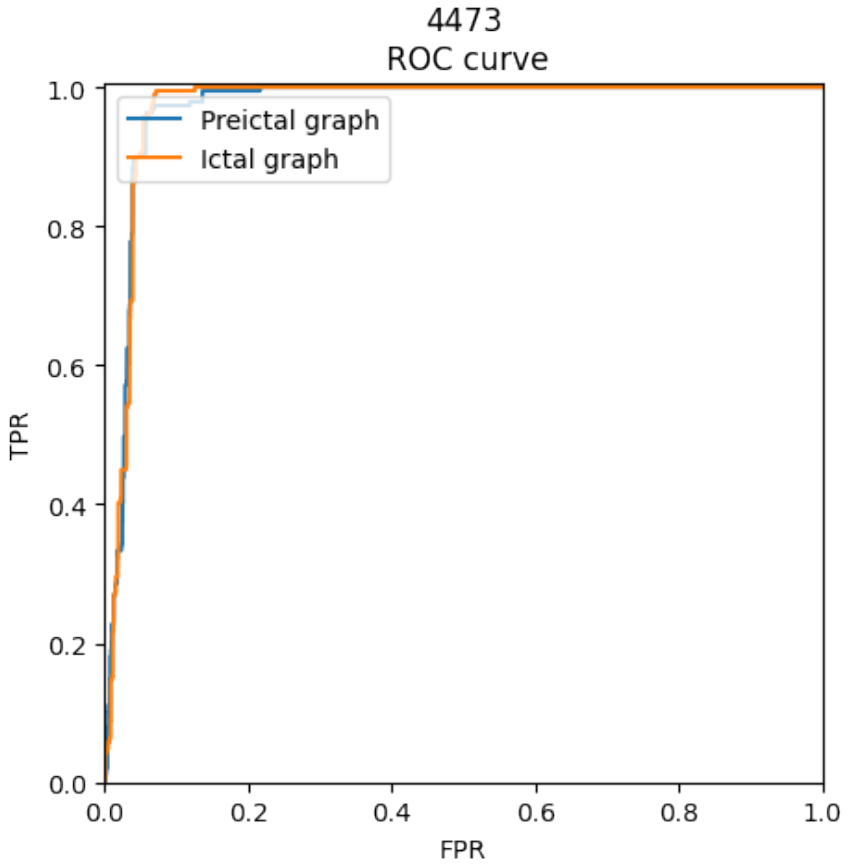

Figure A.22: ROC curve for patient 4473 with the proposed method, using preictal graph a) and ictal one b). The curves reported here give the highest AUC value for fold 1. In particular for the preictal graph we used $K = 0.75$ and $p = 0.95$; for the ictal graph we used $K = 0.85$ and $p = 0.85$.

PATIENT 5452 - CPSZ

Recording 1:

One seizure present. Focal slowing from the right. Sharp waves from the left.

Recording 2:

Eight seizures present but they seem to be abating at the end of the record.

Figure A.23 depicts in a) and c) the inferred preictal and ictal graphs which are associated with the highest AUC value for fold 1. In b) and d) the figure provide the corresponding degree matrices.

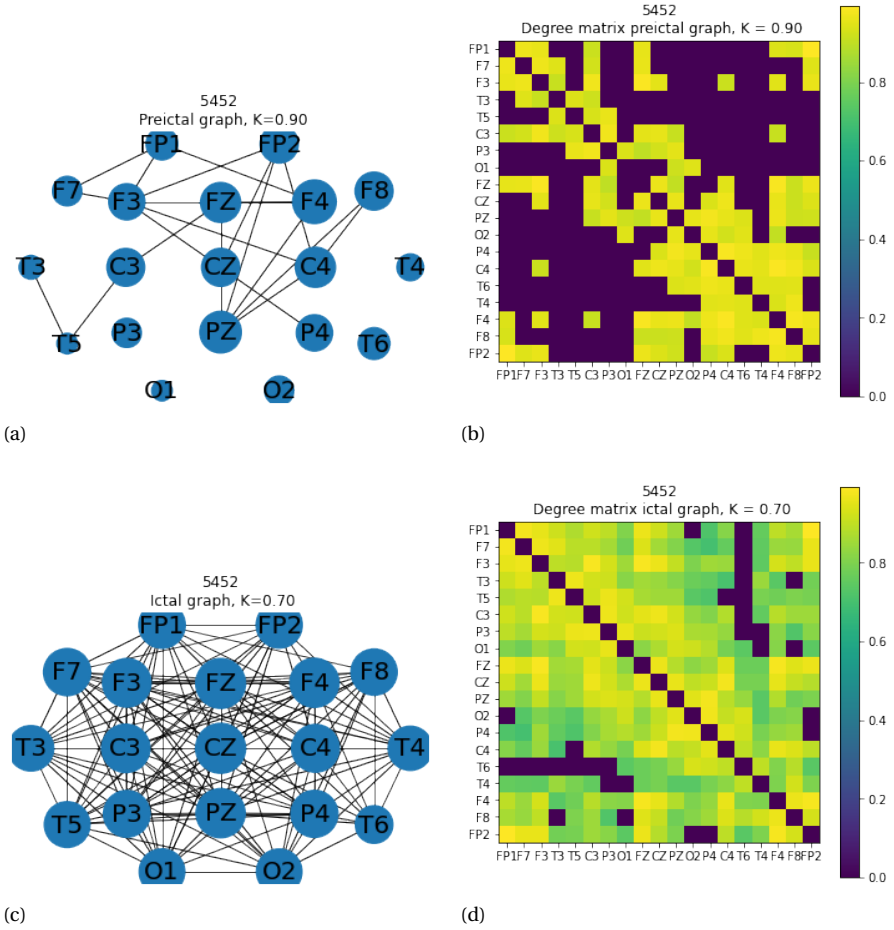

Figure A.23: An illustration of the inferred a) preictal and b) ictal graphs. The structure refers to fold 1 and hyperparameters providing the highest AUC values. The positions of the nodes resemble their relative position in Figure 4.4. In addition, the width of the circle surrounding each node is an indication of its degree. In b) and d) their associated degree matrix.

Common observations between folds:

- No clear area with less connections. Maybe slightly the posterior one.
- Ictal condition is more bandlimited. However, there is no clear difference in terms of bandwidth.
- Sometimes strange shape of curved indicating the need to extract more features.
- Not clear pattern between the hyperparameters.
- Curves portrait almost random detector.

General comments:
The algorithm does not work really well for this patient. Comparable results in terms of AUC with respect to the preictal projection. Best performing electrode for all folds is T3. The algorithm does not seem to perform quite well but this holds also for the single electrode analysis.
Figure A.24 depicts the ROC curves giving highest AUC values for the first fold of the simulations, using the preictal and the ictal graph. Then, Table **??** reports the corresponding TPR values for FPR=10^{-3} and FPR=$2 * 10^{-3}$.

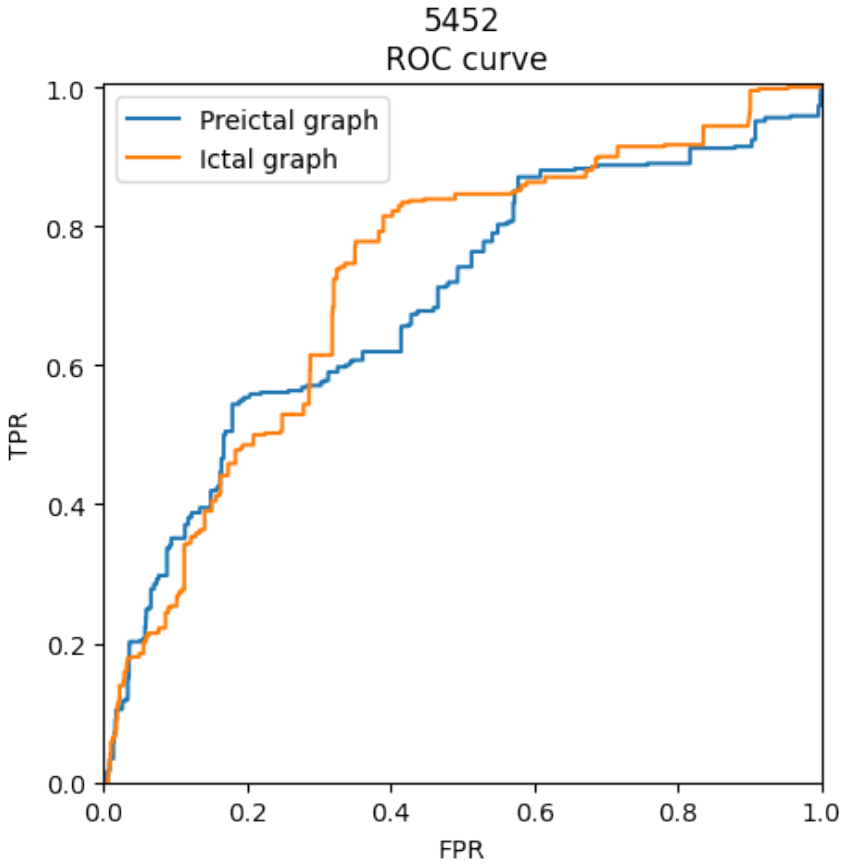

Figure A.24: ROC curve for patient 5452 with the proposed method, using preictal graph a) and ictal one b). The curves reported here give the highest AUC value for fold 1. In particular for the preictal graph we used $K = 0.9$ and $p = 0.95$; for the ictal graph we used $K = 0.7$ and $p = 0.95$.

A

PATIENT 5943 - FNSZ

Recording 1:

Eleven focal seizures from right temporal region superimposed upon a relatively slow background.

Figure A.25 depicts in a) and c) the inferred preictal and ictal graphs which are associated with the highest AUC value for fold 1. In b) and d) the figure provide the corresponding degree matrices.

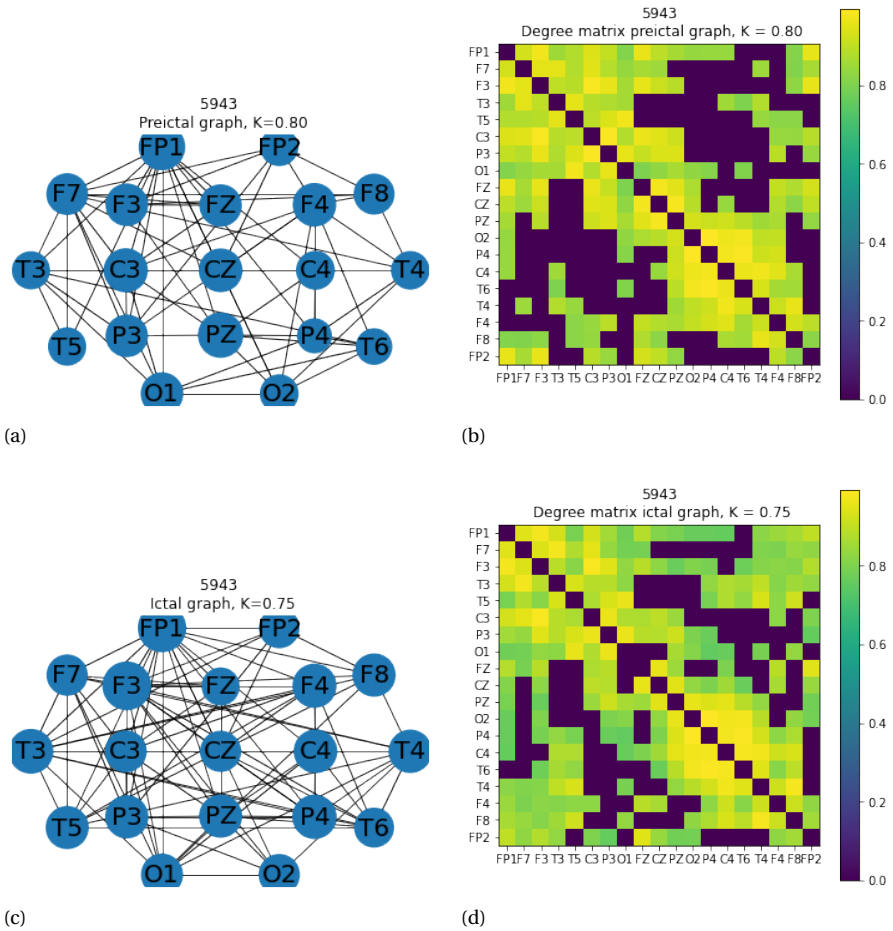

Figure A.25: An illustration of the inferred a) preictal and b) ictal graphs. The structure refers to fold 1 and hyperparameters providing the highest AUC values. The positions of the nodes resemble their relative position in Figure 4.4. In addition, the width of the circle surrounding each node is an indication of its degree. In b) and d) their associated degree matrix.

Common observations between folds:

- No clear area with less connections. Maybe frontal right and temporal left.
- Preictal condition is more bandlimited. However, there is no clear difference in terms of bandwidth.
- Not clear pattern between the hyperparameters.

General comments:
A selection of frequencies benefits the algorithm. The complete graph suits the algorithm. Projection on the ictal graph works slightly better. However, more combination of hyperparameters do not work. More electrodes give good performances. In particular T1, T4 and F8 have best performance for fold 1 2 and 3 respectively.
Figure A.26 depicts the ROC curves giving highest AUC values for the first fold of the simulations, using the preictal and the ictal graph. Then, Table **??** reports the corresponding TPR values for FPR=10^{-3} and FPR=$2 * 10^{-3}$.

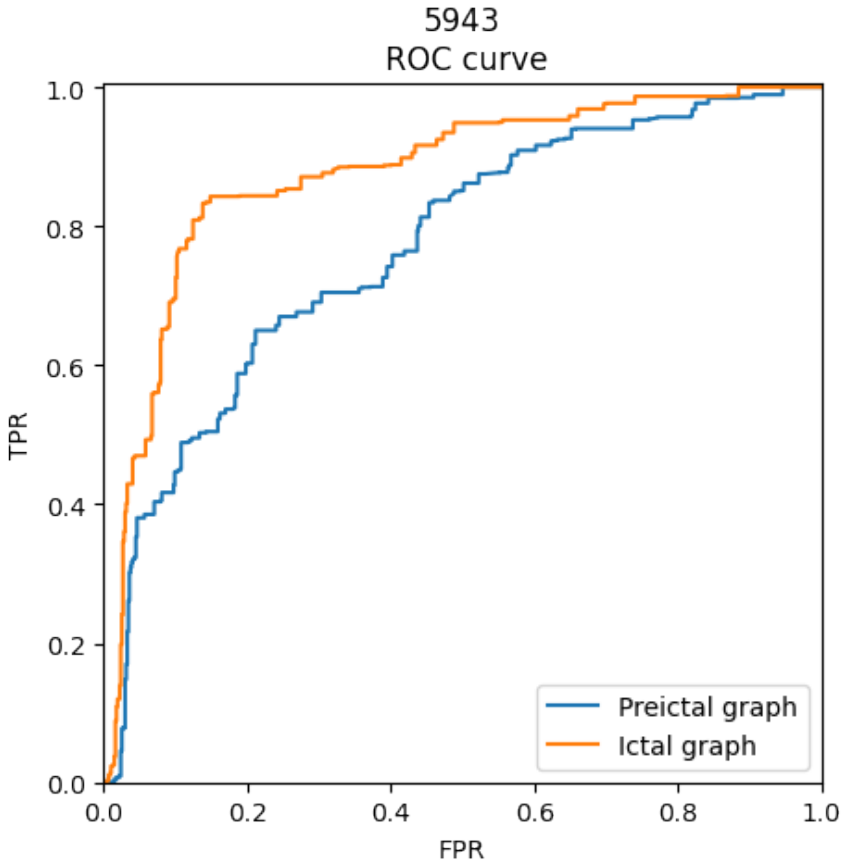

Figure A.26: ROC curve for patient 5943 with the proposed method, using preictal graph a) and ictal one b). The curves reported here give the highest AUC value for fold 1. In particular for the preictal graph we used $K = 0.75$ and $p = 0.8$; for the ictal graph we used $K = 0.75$ and $p = 0.85$.

A

PATIENT 6083 - CPSZ

Recording 1:
Seventeen seizures are recorded. Occipital epileptiform activity that starts from right but rapidly spreads.
Recording 2:
No seizures. Slowing activity.

Figure A.27 depicts in a) and c) the inferred preictal and ictal graphs which are associated with the highest AUC value for fold 1. In b) and d) the figure provide the corresponding degree matrices.

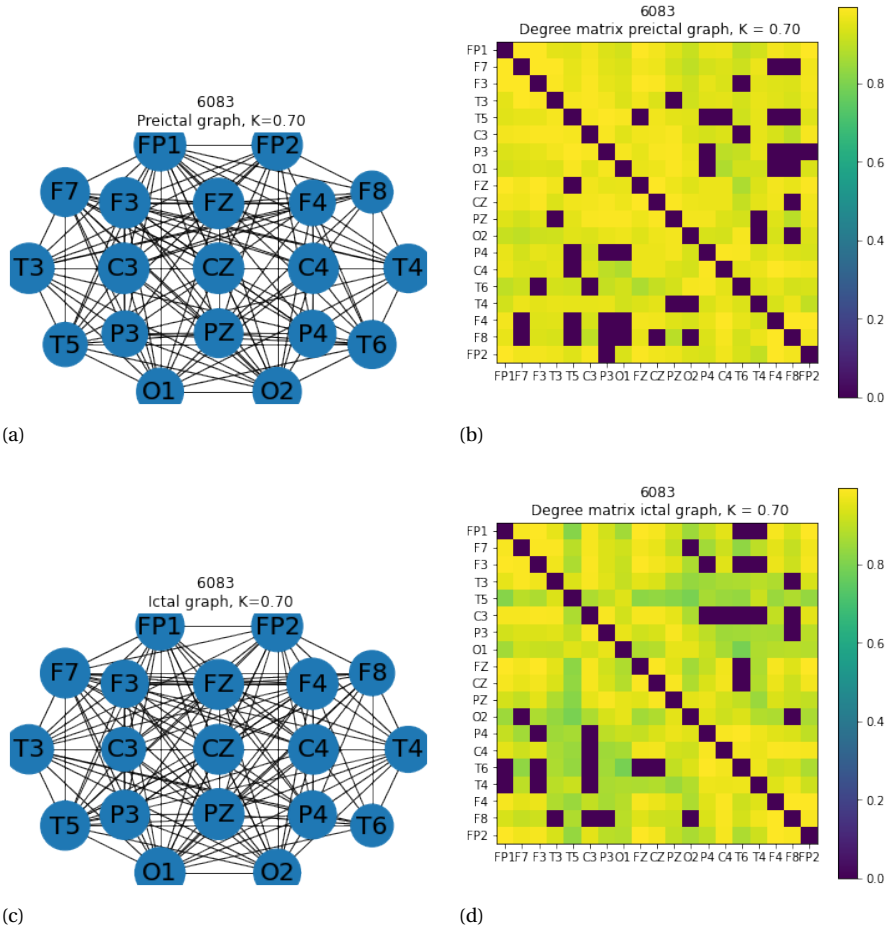

Figure A.27: An illustration of the inferred a) preictal and b) ictal graphs. The structure refers to fold 1 and hyperparameters providing the highest AUC values. The positions of the nodes resemble their relative position in Figure 4.4. In addition, the width of the circle surrounding each node is an indication of its degree. In b) and d) their associated degree matrix.

Common observations between folds:

- Ictal graph has slightly more connections.
- No clear area with less connections.
- Ictal condition is more bandlimited. However, there is no clear difference in terms of bandwidth.
- Sometimes curves with inverse polarity.
- Not clear pattern between the hyperparameters.

General comments:
Ictal projection works slightly worse than preictal one. Best performing is O1 for folds 1 and 3; T6 for fold 2. The algorithm seems to perform best for the proposed algorithm, using ictal graph.
Figure A.28 depicts the ROC curves giving highest AUC values for the first fold of the simulations, using the preictal and the ictal graph. Then, Table **??** reports the corresponding TPR values for FPR=10^{-3} and FPR=$2 * 10^{-3}$.

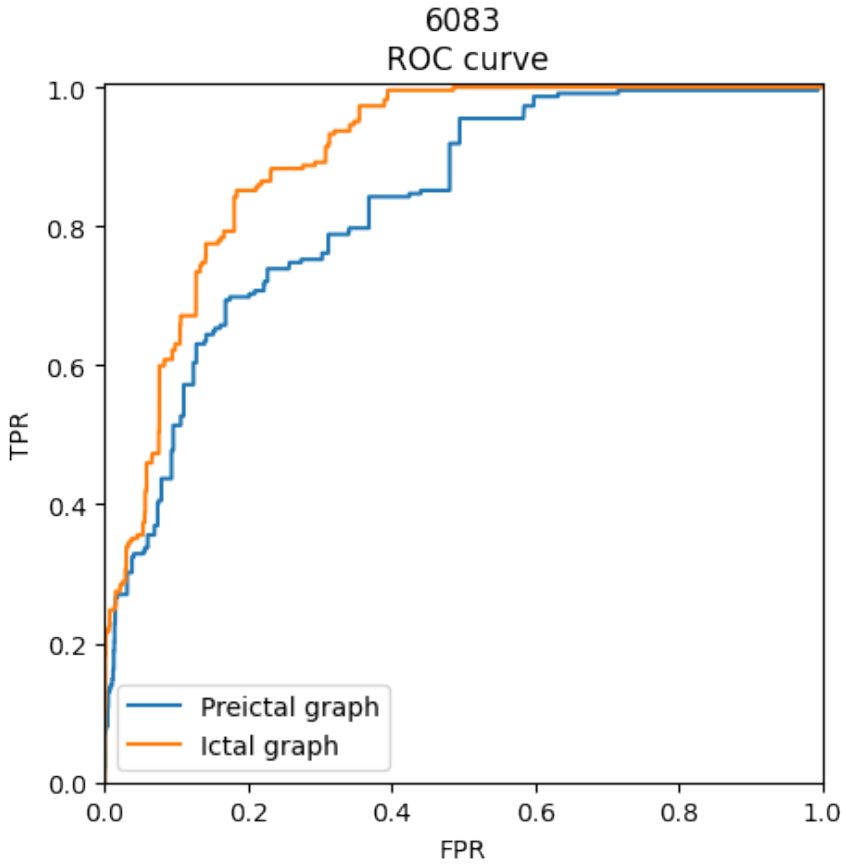

Figure A.28: ROC curve for patient 6083 with the proposed method, using preictal graph a) and ictal one b). The curves reported here give the highest AUC value for fold 1. In particular for the preictal graph we used $K = 0.7$ and $p = 0.85$; for the ictal graph we used $K = 0.7$ and $p = 0.95$.

PATIENT 6413 - CPSZ

Recording 1:

Six seizures from right central temporal region. Slowing in background.

Figure A.29 depicts in a) and c) the inferred preictal and ictal graphs which are associated with the highest AUC value for fold 1. In b) and d) the figure provide the corresponding degree matrices.

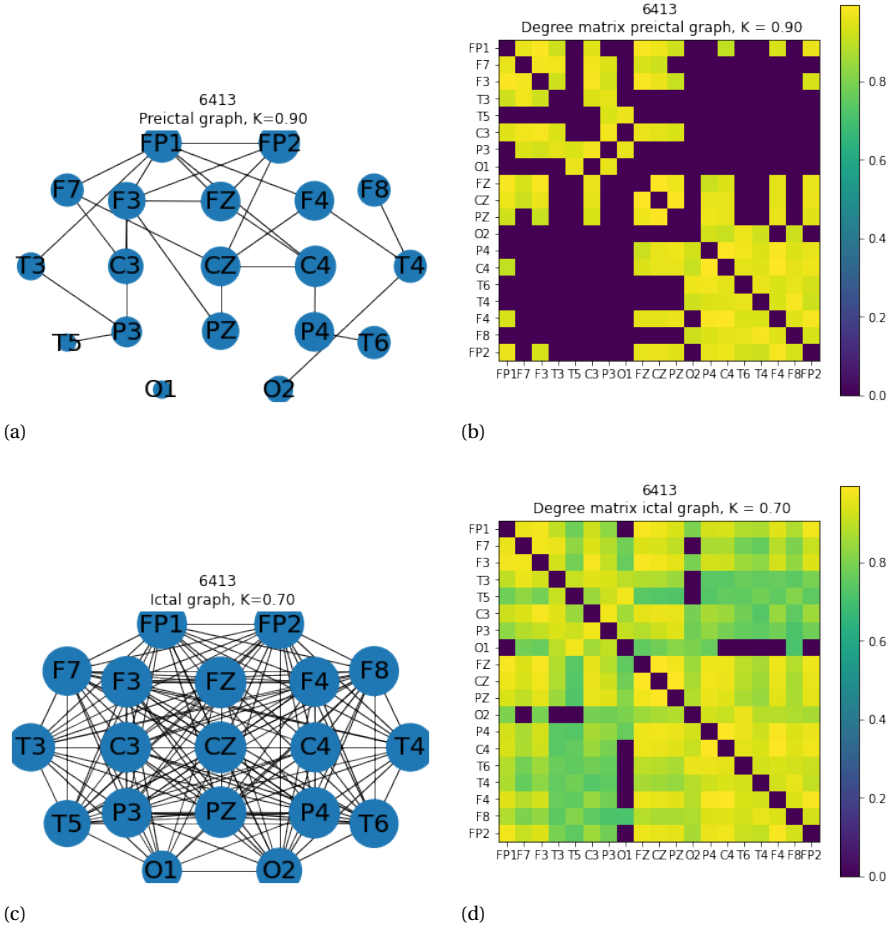

Figure A.29: An illustration of the inferred a) preictal and b) ictal graphs. The structure refers to fold 1 and hyperparameters providing the highest AUC values. The positions of the nodes resemble their relative position in Figure 4.4. In addition, the width of the circle surrounding each node is an indication of its degree. In b) and d) their associated degree matrix.

Common observations between folds:

- No clear area with less connections.

A

- Ictal condition is more bandlimited. However, there is no clear difference in terms of bandwidth.
- Sometimes curves with inverse polarity.
- Not clear pattern between the hyperparameters.

General comments:
Ictal projection works slightly better than preictal one. Best performing is PZ for all the folds. Still, all other electrodes give reasonable performance too. Even though the graph does not pinpoint the onset of the seizure, the proposed algorithm outperforms all three baselines for this patient. We remark that the time considered is short.
Figure A.30 depicts the ROC curves giving highest AUC values for the first fold of the simulations, using the preictal and the ictal graph. Then, Table **??** reports the corresponding TPR values for FPR=10^{-3} and FPR=$2 * 10^{-3}$.

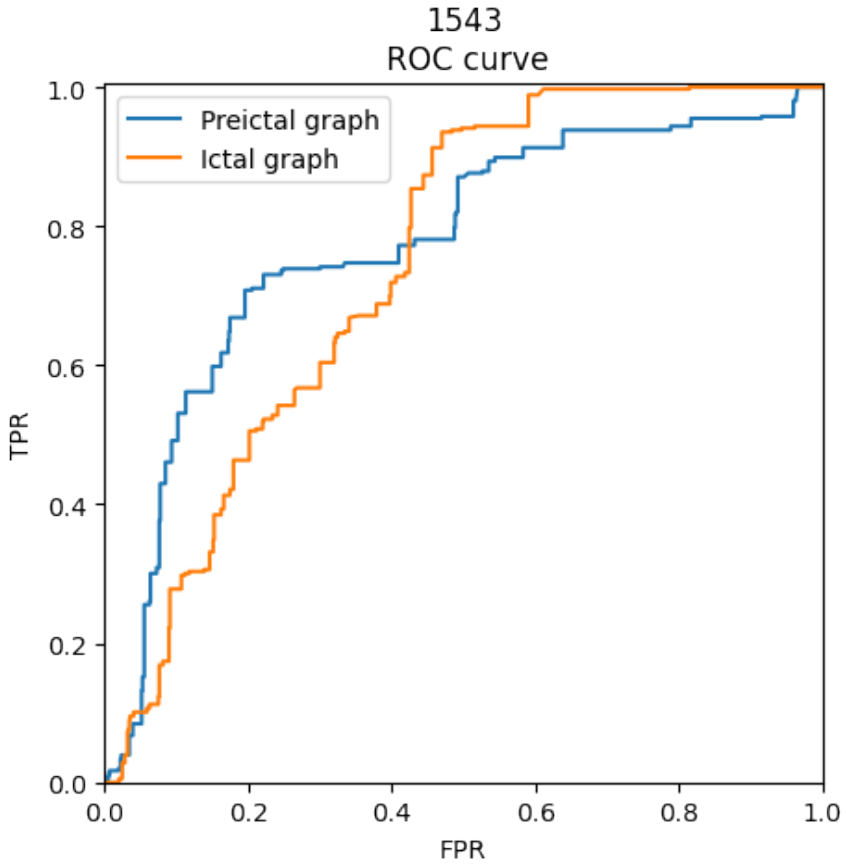

Figure A.30: ROC curve for patient 258 with the proposed method, using preictal graph a) and ictal one b). The curves reported here give the highest AUC value for fold 1. In particular for the preictal graph we used $K = 0.9$ and $p = 0.85$; for the ictal graph we used $K = 0.7$ and $p = 0.7$.

PATIENT 6507 - FNSZ

Recording 1:

Seven seizures are recorded. Slow pattern from right, seizures starting from left

Figure A.31 depicts in a) and c) the inferred preictal and ictal graphs which are associated with the highest AUC value for fold 1. In b) and d) the figure provide the corresponding degree matrices.

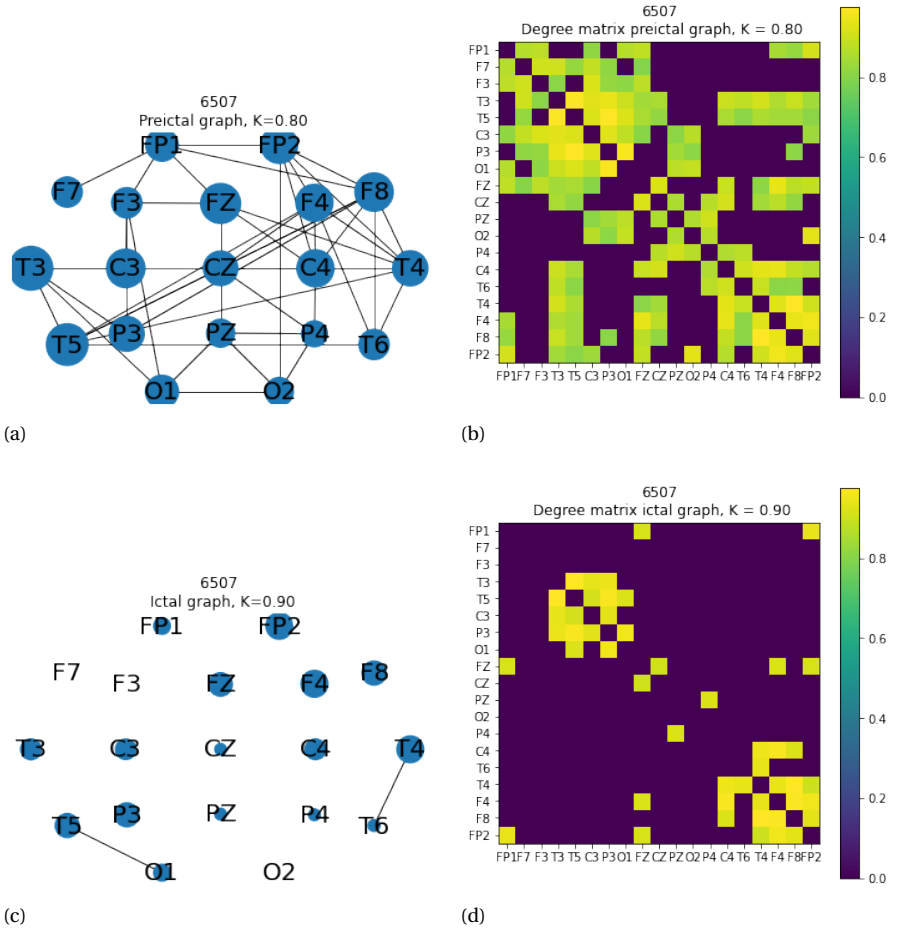

Figure A.31: An illustration of the inferred a) preictal and b) ictal graphs. The structure refers to fold 1 and hyperparameters providing the highest AUC values. The positions of the nodes resemble their relative position in Figure 4.4. In addition, the width of the circle surrounding each node is an indication of its degree. In b) and d) their associated degree matrix.

Common observations between folds:

- Ictal condition is more bandlimited. However, there is no clear difference in terms

A

of bandwidth.
- Sometimes curves with inverse polarity.
- Not clear pattern between the hyperparameters.

General comments:
The algorithm gives poor performance.
Figure A.32 depicts the ROC curves giving highest AUC values for the first fold of the simulations, using the preictal and the ictal graph. Then, Table **??** reports the corresponding TPR values for FPR=10^{-3} and FPR=$2 * 10^{-3}$.

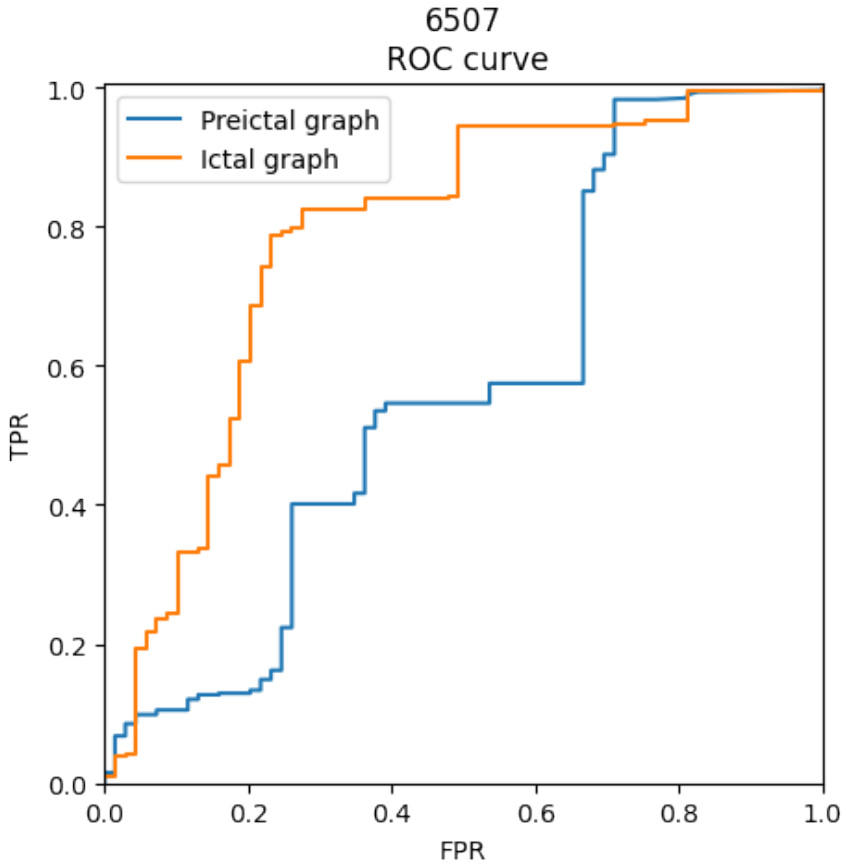

Figure A.32: ROC curve for patient 6507 with the proposed method, using preictal graph a) and ictal one b). The curves reported here give the highest AUC value for fold 1. In particular for the preictal graph we used $K = 0.8$ and $p = 0.95$; for the ictal graph we used $K = 0.9$ and $p = 0.75$.

PATIENT 7234 - FNSZ

Recording 1:

Five seizures are considered. central parietal and posterior temporal regions. Bursts of epileptiform activity in the right posterior quadrant and periodic sharp waves.

Figure A.33 depicts in a) and c) the inferred preictal and ictal graphs which are associated with the highest AUC value for fold 1. In b) and d) the figure provide the corresponding degree matrices.

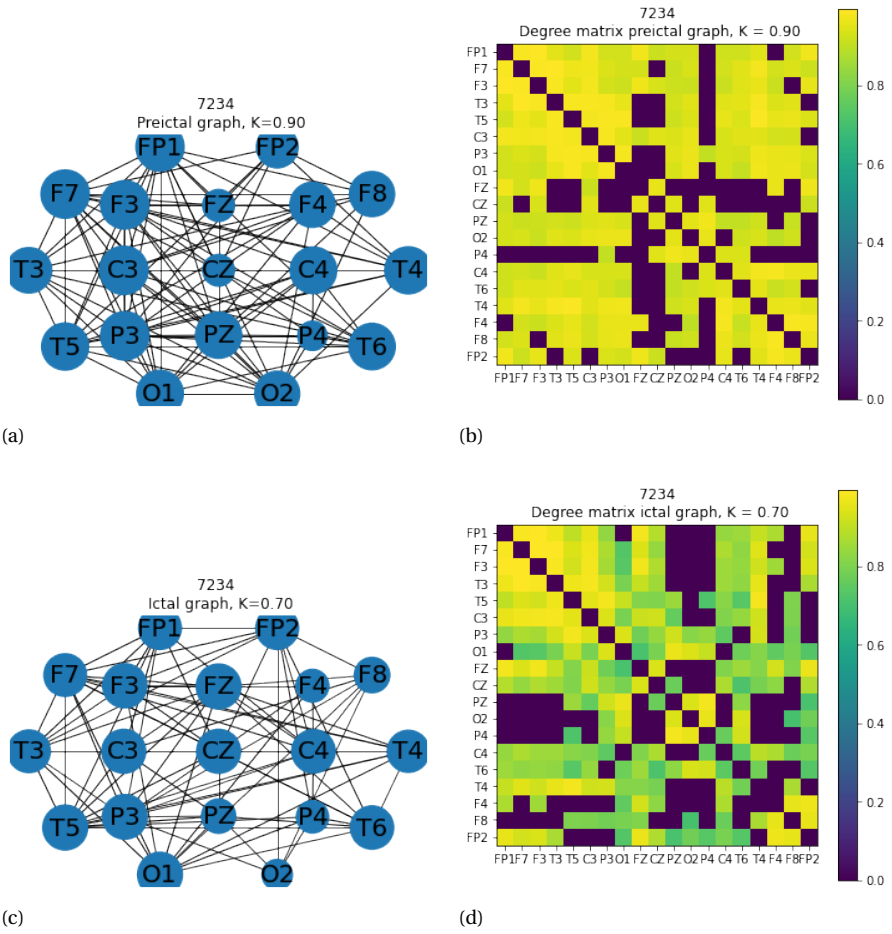

Figure A.33: An illustration of the inferred a) preictal and b) ictal graphs. The structure refers to fold 1 and hyperparameters providing the highest AUC values. The positions of the nodes resemble their relative position in Figure 4.4. In addition, the width of the circle surrounding each node is an indication of its degree. In b) and d) their associated degree matrix.

Common observations between folds:

- Ictal condition slightly less connections in folds one and three. The opposite holds for fold 2.
- No clear area with less connections
- For fold 2, ictal condition is more bandlimited. Nice difference in terms of spectrum.
- Small variability but this is to be expected as we are working with not many data.
- Not clear pattern between the hyperparameters. - Not so nice curves, tend to be randomic.

General comments:
Ictal projection works slightly better than preictal one. Single electrode analysis does not work extremely well (AUC < 0.8) with best sensors P4 for fold 1 and 2; O1 for the third fold. The proposed algorithm does not seem to give good results.
Figure A.34 depicts the ROC curves giving highest AUC values for the first fold of the simulations, using the preictal and the ictal graph. Then, Table **??** reports the corresponding TPR values for FPR=10^{-3} and FPR=$2 * 10^{-3}$.

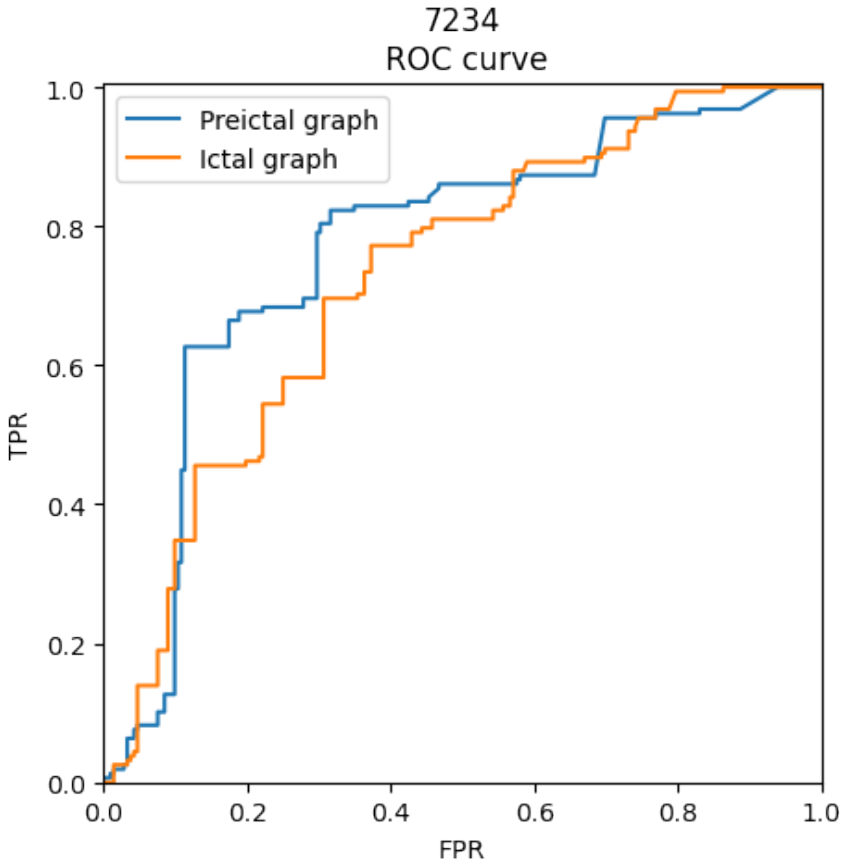

Figure A.34: ROC curve for patient 7234 with the proposed method, using preictal graph a) and ictal one b). The curves reported here give the highest AUC value for fold 1. In particular for the preictal graph we used $K = 0.9$ and $p = 0.85$; for the ictal graph we used $K = 0.85$ and $p = 0.95$.